REPUBLIC OF TURKEY

YILDIZ TECHNICAL UNIVERSITY

GRADUATE SCHOOL OF SCIENCE AND ENGINEERING

THEORETICAL AND EXPERIMENTAL STUDY OF PLATELET GENERATION FROM MEGAKARYOCYTE IN A MICROFLUIDIC PLATFORM

Günay ATAK

DOCTOR OF PHILOSOPHY THESIS

Department of Chemical Engineering

Chemical Engineering Program

Supervisor

Prof. Dr. Hasan SADIKOĞLU

Co-Supervisor

Assist. Prof. Dr. Muhammed Enes ORUÇ

February, 2022

REPUBLIC OF TURKEY

YILDIZ TECHNICAL UNIVERSITY

GRADUATE SCHOOL OF SCIENCE AND ENGINEERING

THEORETICAL AND EXPERIMENTAL STUDY OF PLATELET GENERATION FROM MEGAKARYOCYTE IN A MICROFLUIDIC PLATFORM

A thesis submitted by Günay ATAK in partial fulfillment of the requirements for the degree of DOCTOR OF PHILOSOPHY is approved by the committee on 25.02.2022 in Department of Chemical Engineering, Chemical Engineering Program.

Prof. Dr. Hasan SADIKOĞLU Yildiz Technical University Supervisor	Assist. Prof. Dr. Muhammed Enes ORUÇ Gebze Technical University Co- supervisor

Approved by the Examining Committee

Prof. Dr. Hasan SADIKOĞLU, Supervisor

Yildiz Technical University _____

Prof. Dr. Mustafa ÖZİLGEN, Member

Yeditepe University _____

Prof. Dr. Fatma Jale GÜLEN, Member

Yildiz Technical University _____

Assoc. Prof. Dr. Nil ACARALI, Member

Yildiz Technical University _____

Assist. Prof. Dr. Özgün YÜCEL, Member

Gebze Technical University _____

I hereby declare that I have obtained the required legal permissions during data collection and exploitation procedures, that I have made the in-text citations and cited the references properly, that I haven't falsified and/or fabricated research data and results of the study and that I have abided by the principles of the scientific research and ethics during my Thesis Study under the title of Theoretical and Experimental Study of Platelet Generation from Megakaryocyte in a Microfluidic Platform supervised by my supervisor, Prof. Dr. Hasan SADIKOĞLU. In the case of a discovery of false statement, I am to acknowledge any legal consequence.

Günay ATAK

Signature

This study was supported by the Yildiz Technical University Scientific Research Projects Coordination Unit Grant No: FCD-2018-3150.

Dedicated to my family

ACKNOWLEDGEMENTS

First of all, I would like to thank my very valuable supervisor Prof. Dr. Hasan SADIKOĞLU, who never stop supported me during my doctorate education. I would also like to thank my co-supervisor, Assist. Prof. Dr. Muhammed Enes ORUÇ shared his knowledge and experience with me with great patience and, without hesitation, created a solution for every problem I encountered. I want to thank my thesis monitoring committee members, Prof. Dr. Fatma Jale GÜLEN and Prof. Dr. Mustafa ÖZİLGEN, who shed light on my works with their valuable ideas, knowledge, and experiences throughout my doctoral education.

I want to thank Prof. Dr. Bayram YILMAZ, Assoc. Dr. Fatih KOCABAŞ, Dr. Neslihan MERiÇ, and Dr. Merve USLU provided the laboratory facilities. I want to thank my dear colleagues in the Department of Chemical Engineering for their support. I want to thank the Yildiz Technical University Scientific Research Projects Coordination Unit, which supported a part of my thesis with the project numbered FCD-2018-3150.

Finally, I would like to express my gratitude to my mother, Serpil BAYDAR, and my father, İbrahim BAYDAR, who has been by my side unconditionally in every step I have taken so far has given me financial and morale support. I would also like to thank my one and only brother Yiğit BAYDAR whose existence is my source of happiness and whose support I always felt. I want to express my endless thanks to my dear husband, Emre ATAK, who has been by my side since the first day of my doctoral education, which was full of stress and anxiety and has never spared his support and patience. My last thank for my four-legged son, my lovely dog Moka, my most significant source of morale, whose warmth and eternal loyalty I always feel.

Günay ATAK

TABLE OF CONTENTS

LIST OF SYMBOLS viii
LIST OF ABBREVIATIONS ix
LIST OF FIGURES x
LIST OF TABLES xiii
ABSTRACT xiv
ÖZET xvi
1 INTRODUCTION 1
1.1 Literature Review 1
1.2 Objective of the Thesis 3
1.3 Hypothesis 4
2 THEORETICAL BACKROUND 5
2.1 Platelets 5
2.2 Megakaryocytes 7
2.3 Microfluidics 8
2.4 Platelet formation in a microchannel 10
3 MICROFLUDIC DEVICE 14
3.1 Design of Microchips 14
3.2 Simulation of Microchips 16
3.2.1 Finite element method 16
3.2.2 COMSOL multiphsics 16
3.2.3 The governing equations and implementation of COMSOL 17
3.2.4 Flow properties 18
3.2.5 Particle tracking 18
3.3 Fabrication of Microchips 19
3.3.1 Mask design 23
3.3.2 Silicon wafer mold production by photolithography 28
3.3.3 Photoresist coating process 29
3.3.4 Soft baking of SU-8 30
3.3.5 UV exposure 31
3.3.6 Post bake 31
3.3.7 Chemical etching process (Developer) 31

3.3.8 PDMS chamber via soft lithography 33
4 RESPONSE SURFACE METHODOLOGY **38**
5 ISOLATION OF MEGAKARYOCYTES **42**
6 RESULTS AND DISCUSSION **47**
6.1 Megakaryocyte Isolation 47
6.2 Determination of Relation Between Flow Rate and Shear Rate and Shear Stress 48
6.2.1 Flow Simulation 50
6.2.2 Relationship Between Flow and Shear Stress/Shear Rate 50
6.3 Microfluidic Chip Design 54
6.3.1 COMSOL Multiphysics application 54
6.4 COMSOL Modeling 56
6.4.1 Response surface methodology 59
6.5 Fabrication of Different Geometries for Platelet Formation 67
REFERENCES **75**
A SIMULATION STUDIES **79**
PUBLICATIONS FROM THE THESIS **119**

LIST OF SYMBOLS

$	American Dollar
°C	Centigrade degree
°	Degree
g	Gram
kg	Kilogram
μL	Microliter
μm	Micrometer
mg	Milligram
mL	Milliliter
mm	Millimeter
mM	Millimolar
min	Minute
ng	Nanogram
Pa	Pascal
%	Percent
rpm	Revolutions per minute
s	Second

LIST OF ABBREVIATIONS

α	Angle between pressure channels
CFD	Computational fluid dynamics
MEP	Megakaryocyte erythroid progenitor
MK	Megakaryocyte
PET	Polyethylene terephthalate
PLT	Platelet
Q_1	Pressure channel rate
Q_2	Megakaryocyte channel rate
Q_3	Main channel rate
Re	Reynolds number
RSM	Response surface methodology
TPO	Trombopoietin
VWF	von Willebrand factor
w_1	Height of pressure flow
w_2	Height of megakaryocyte flow

LIST OF FIGURES

Figure 2.1 PLT production in bone barrow 6
Figure 2.2 Microfluidic chip 9
Figure 2.3 Shear stress effect on liquid layers 9
Figure 2.4 Number of published articles on PLT production 11
Figure 3.1 Microfluidic chip geometry 15
Figure 3.2 The design of the microfluidic bioreactor 15
Figure 3.3 Special clothes for the cleanroom 20
Figure 3.4 An image taken from out of the cleanroom 20
Figure 3.5 An image taken from inside of the cleanroom 21
Figure 3.6 The chemical bench in the cleanroom 22
Figure 3.7 The general look of cleanroom 22
Figure 3.8 Studying in cleanroom with special clothes 23
Figure 3.9 Acetate mask used in the production of microfluid channel 24
Figure 3.10 Heidelberg DWL 66 fs mask printer device 25
Figure 3.11 Chrome photomask after writing process 26
Figure 3.12 Chrome photomask production steps. A) Placing the cleaned chrome photomask in the spin coater and dropping the AZ 1505 positive photoresist B) AZ 1505 photoresist coated chrome photomask display C) AZ 1505 photoresist coated chrome photomask placed in the mask printer. D) Representation of chrome photomask in chrome etching chemical 27
Figure 3.13 Difference between positive photoresistn and negative photoresist in applications 29
Figure 3.14 A) Mold image produced using photolithography with SU-8 photoresist on silicon wafer B) Microscope image and dimensions of the micro-fluid channel produced 30
Figure 3.15 SUSS MicroTec Lithography Device 32
Figure 3.16 (A) The PDMS prepolymer and hardening agent were mixed in a 10:1 ratio. (B) Air bubbles in the mixture were removed by taking the vacuum desiccator. (C) The mixture was poured onto the silicon wafer mold. (D) Hardening for 3 hours at 65 °C on the heater. (D) The PDMS separeted from the silicon wafer was cut the size and the channel entrance and exit holes were drilled 34
Figure 3.17 Harrick plasma cleaner device 35

Figure 3.18 Binding between the PDMS and the glass surface by covalent bond interaction takes place between the surfaces [56] 36

Figure 3.19 Single channel microfluid chip..... 37

Figure 5.1 Isolation magnet and selection kit..... 42

Figure 5.2 Mice for isolation of MKs 43

Figure 6.1 Images of MKs (Day 1)..... 47

Figure 6.2 Images of MKs (Day 6)..... 48

Figure 6.3 Images of MKs (Day 10)..... 49

Figure 6.4 Microchip trial (MKs in the microchannel)..... 49

Figure 6.5 Microchip trial (size of MK inside chip: ~45 μm)..... 51

Figure 6.6 The relation between Velocity (μm/s) and Shear Stress (Pa) 52

Figure 6.7 The relation between velocity (μm/s) and shear rate (1/s)..... 52

Figure 6.8 The particle trajectories at flow velocity 6000 μm/s and particle diameters of 20 μm (a), 40 μm (b), 60 μm (c), 80 μm (d) 53

Figure 6.9 Effect of an angle between pressure channels at Q_1=10 μL/min, Q_2=5 μL/min, Q_3=5 μL/min. a: α=30°, b: α=60°, c: α=90° 55

Figure 6.10 Effect of flow rate ratios between main and pressure channels at α=60°, Q_2=5 μL/min. a: Q_1/Q_2=2, Q_3/Q_2=5, b: Q_1/Q_2=4, Q_3/Q_2=3, c: Q_1/Q_2=6, Q_3/Q_2=1..... 56

Figure 6.11 A: Shear rate distribution along the length of the microchip at Q_2=5 μL/min. (Q_1=24 μL/min and Q_3=6 μL/min) B: Flow rate distribution along the length of the microchip at Q_2=5 μL/min. (Q_1=24 μL/min and Q_3=6 μL/min) 57

Figure 6.12 A: Average and B: Maximum shear rate ranges at different flow rates..... 58

Figure 6.13 Contour-plot of percent of trapped particles: The effect of Q_1/Q_2 and angle. Other variable is held at zero level. Q_1=25 μm/min..... 63

Figure 6.14 Contour-plot of percent of trapped particles: The effect of Q_3/Q_2 and Q_1/Q_2. Other variable is held at zero level. Q_1=25 μm/min..... 64

Figure 6.15 Contour-plot of percent of trapped particles: The effect of angle and Q_3/Q_2. Other variable is held at zero level. Q_1=25 μm/min..... 65

Figure 6.16 MKs locations at different times in a microchannel at the optimum values of physical conditions. α=50.46°, Q_1=23.95 μL/min, Q_2=5 μL/min, Q_3=5.65 μL/min a: Near the beginning time of the process b: Near the mid-time of the process c: After the mid-time of the process d: Near the end time of the process..... 66

Figure 6.17 A general overview of chrome mask 67

Figure 6.18 Gradual narrowing and expanding channel design 68

Figure 6.19 Channels including pillars with different angles 69

Figure 6.20 Gradual narrowing channel design with one step 70
Figure 6.21 Gradual narrowing channel design with two steps..... 70
Figure 6.22 Channels including pillars with 90 x 10 μm with 2 μm apart..... 71
Figure 6.23 Repetitive gradual narrowing channel design with two steps in one microchip..... 72
Figure 6.24 One step repetitive tapering channel design in a single microchip 72

LIST OF TABLES

Table 2.1 Literature review of the PLT formation from MKs in a microchannel 12
Table 3.1 SU-8 2100 application parameters..... 33
Table 4.1 Statistical evaluation of the model used with ANOVA test 41
Table 5.1 Properties of mice..... 42
Table 6.1 Maximum shear stress and shear rate values for different velocities50
Table 6.2 Range and levels of independent variables for simulation studies... 59
Table 6.3 The actual values of simulation conditions and response variable .. 61
Table 6.4 ANOVA for response surface linear model 62
Table 6.5 Optimum values of independent variables obtained with RSM..... 65

ABSTRACT

Theoretical and Experimental Study of Platelet Generation from Megakaryocyte in a Microfluidic Platform

Günay ATAK

Department of Chemical Engineering

Doctor of Philosophy Thesis

Supervisor: Prof. Dr. Hasan SADIKOĞLU

Co- supervisor: Assist. Prof. Dr. Muhammed Enes ORUÇ

This thesis covers the design and fabrication steps of a microfluidic-based chip for the production of platelets (PLT) from megakaryocytes (MK). With the COMSOL program, the shear stress profiles were determined with the geometries drawn in the 2D environment, the channel geometry and shear rates were determined by the finite element method, the microfluidic chips were produced in different geometries containing 10-micron channels using the soft lithography technique and the chrome photomask, the sealing of the produced microfluidic chips were tested and the isolation procedure was determined for MKs obtained by differentiation of hematopoietic stem cells isolated from bone marrow of mice in culture medium, and the images of MKs obtained under microscope were reported. The PLT production process from MKs was examined in two stages; the first of these is to trap the MKs with the effect of flow, and the second is the elongation of the proPLTs. Within the scope of this thesis, only the first step of the process aimed at trapping more MK with the help of flow pressure was focused on. Based on the simulation and optimization results, the maximum number of

MKs was trapped when the angle between the pressure and the main flow channel of the microfluidic chip was 50.46 degrees. On the other hand, it was concluded that the contribution of the ratio of the velocity of the pressure flow to the velocity of the main flow is more significant than the angle between the flow channels on the percentage of MKs trapped. Throughout the entire study, 2D modeling was preferred as it can achieve numerically much higher spatial and temporal resolution compared to 3D simulation. The most important output of this thesis is that microfluidic-based chips are suitable platforms for the investigation of PLT production from MKs and will guide the studies to increase the PLT production efficiency. PLT production microbioreactors are open to research and development and there is a need to find solutions to the constraints they face.

Keywords: Microfluidics, biotechnology, mathematical modeling, platelet, Comsol multiphysics

ÖZET

Mikroakışkan Platformlarda Megakaryositten Trombosit Oluşumunun Teorik ve Deneysel Çalışması

Günay ATAK

Kimya Mühendisliği Anabilim Dalı

Doktora Tezi

Danışman: Prof. Dr. Hasan SADIKOĞLU

Eş-Danışman: Dr. Öğr. Üyesi Muhammed Enes ORUÇ

Bu tez, megakaryositlerden (MK) trombosit (PLT) üretiminin gerçekleştirilmesi için mikroakışkan tabanlı bir çipin tasarım ve üretim basamaklarını içermektedir. COMSOL programı ile 2D ortamda çizilen geometriler ile kayma gerilimi profilleri tespit edilerek sonlu elemanlar metodu ile kanal geometrisi ve kayma hızları belirlendi, yumuşak litografi tekniği ile krom fotomaske kullanılarak 10 mikronluk kanallar içeren farklı geometrilerde mikroakışkan çip üretimleri yapıldı, üretilen mikroakışkan çiplerin sızdırmazlıkları test edildi ve farelerin kemik iliğinden izole edilen hematopoetik kök hücrelerin kültür ortamında farklılaştırılmasıyla elde edilen MK' ler için izolasyon prosedürü belirlenerek elde edilen MK' lerin mikroskop altında görüntüleri rapor edildi. MK' lerden PLT üretim süreci iki aşamalı olarak incelendi; bunlardan birincisi MK' leri akış etkisiyle sıkıştırmak, ikincisi ise proPLT' lerin uzamasıdır. Bu tez çalışması kapsamında, akış basıncı yardımıyla daha fazla MK' yi yakalamayı amaçlayan sürecin sadece ilk adımına odaklanıldı. Simülasyon ve optimizasyon sonuçlarına dayanarak, mikroakışkan çipin basınç ve ana akış kanalı arasındaki açı 50,46 derece olduğunda, maksimum

sayıda MK hapsedildi. Öte yandan, basınç akışının hızının ana akış hızına oranının katkısının, hapsedilen MK' lerin yüzdesi üzerindeki akış kanalları arasındaki açıdan daha önemli olduğu sonucuna varıldı. Tüm çalışma boyunca, 3D simülasyona kıyasla sayısal olarak çok daha yüksek uzaysal ve zamansal çözünürlük elde edilebildiği için 2D modelleme tercih edildi. Bu tezin en önemli çıktısı, mikroakışkan tabanlı çiplerin MK' lerden PLT üretiminin incelenmesi için uygun platformlar olduğu ve PLT üretim veriminin arttırılması için yapılacak çalışmalara yön vereceğidir. PLT üretim mikrobiyoreaktörleri araştırma ve geliştirmeye açık olup karşı karşıya kalının kısıtlamalar için çözüm bulunmasına ihtiyaç duyulmaktadır.

Anahtar Kelimeler: Mikroakışkanlar, biyoteknoloji, matematiksel modelleme, trombosit, Comsol multiphysics

1
INTRODUCTION

1.1 Literature Review

PLTs are specialized cells produced by MKs in the bone marrow that represent the first defense against bleeding, yet they also play a pathological role in thrombosis, inflammation, and cancer [1-22]. Millions of PLT transfusions are conducted each year, and the supply of this blood component is limited. There are many diseases where PLT production or function is damaged with severe consequences for patients. With such clinical need, new insight into the formation of PLTs would have a major impact on patients and healthcare [9]. PLTs are essential for hemostasis and thrombosis and have important roles in injury repair, inflammatory reactions, angiogenesis, lymph-vessel separation, and tumor metastasis. In humans, approximately 10^{11} PLTs are produced each day, probably through the cytoplasmic fragmentation of MKs or formation of proPLTs, elongated pseudopods that extend from mature MKs and release PLTs [5].

More than 2.17 million apheresis equivalent PLT units are transfused yearly in the United States at a cost of >$1 billion per year. The demand for PLT transfusion has increased significantly over the past decade. However, PLTs have a shelf life of 5 days due to bacterial contamination and this leads to storage problems. This results in a near-static donor pool and significant PLT shortage resulting from PLT deterioration.

An efficient, donor-independent PLT bioreactor talented at generating clinically significant numbers of functional human PLTs is necessary to obviate risks associated with PLT supply and storage, and help meet growing transfusion needs [6]. There has been much interest in the possibility of using stem cells to produce PLTs in the laboratory for clinical use. Hematopoietic stem cells are progenitor cells that reside in the marrow and give rise to all of the various types of blood cells. Another source of stem cells are induced pluripotent stem cells, which are cells created from an adult cell, such as skin or hematopoietic cells, through the

introduction of specific genes that reprogram the cell and transform it into a pluripotent stem cell. Culture systems have been described for differentiating both hematopoietic stem cells and induced pluripotent stem cells into MKs and PLTs, but the yields have been meager. Despite the successful production of functional PLTs in the laboratory, reported yields have been far too low for clinical use and the field is currently at a technical impasse [7]. To overcome these limitations, functional human tissue models have been developed and studied to guess ex vivo outcomes for new insight on bone marrow functions in vivo. There are many challenges that these models must overcome, from faithfully mimicking the physiological composition and functions of bone marrow, to the collection of the PLTs generated and validation of their viability and function for human use. The overall goal is to identify innovative instruments to study mechanisms of PLT release, diseases related to PLT production and new therapeutic targets starting from human progenitor cells [8].

The bone marrow has been proposed to be a major site of PLT production, although there is indirect evidence that the lungs might also contribute to PLT biogenesis. MKs that release PLTs in the lungs originate from extrapulmonary sites such as the bone marrow; Lefrançairs et al. [23] observed large MKs migrating out of the bone marrow space. The contribution of the lungs to PLT biogenesis is substantial, accounting for approximately 50% of total PLT production or 10 million PLTs per hour. Furthermore, they identified populations of mature and immature MKs along with hematopoietic progenitors in the extravascular spaces of the lungs. Under conditions of thrombocytopenia and relative stem cell deficiency in the bone marrow, these progenitors can migrate out of the lungs, repopulate the bone marrow, completely reconstitute blood PLT counts, and contribute to multiple hematopoietic strains. These results identify the lungs as a primary site of final PLT production and an organ with considerable hematopoietic potential [23].

1.2 Objective of the Thesis

PLTs are small cells that provide blood circulation and are responsible for stopping bleeding. PLTs are formed by breaking down larger cells called MKs inside the body. PLTs that are needed in large quantities have a 5-day shelf life due to bacterial contamination and storage time limitation, and they must be produced by alternative methods. The aim of this thesis is to develop a microfluidic-based device that breaks MKs into PLTs. More specifically, the targets of the thesis are as follows:

- **Step 1 -** Determination of the channel sizes based on the desired shear stress value by finite element method: Simulation of microfluidic-chips will be done with the COMSOL Multiphysics program, a finite element analysis method. By considering different channel architectures, flow values will be changed and shear stress values will be determined.
- **Step 2 -** Fabrication of the microfluidic device in line with the specified geometries obtained by modeling: The production of the chip, which will be transformed from MKs to PLTs, is the most important part of the thesis. It is very important that the chip, which will consist of two parts, is leak-proof. In this context, the chip will be produced with the method called "soft lithography". A brief summary of the fabrication: In cleanroom conditions, molds will be produced first for micron channels. Then PDMS, an elastomer polymer, will be poured on the mold and the top of the chip will be prepared. After the surface modifications, the lower glass layer and the polymeric upper part will be sealed together.
- **Step 3 -** Isolation of MK: Performing stem cell isolation in the bone marrow of the mice and then MK differentiation will be performed and fed to the experimental environment with the help of pumps. With the help of EasySep™ Magnet and EasySep™ Mouse PE Positive Selection Kit specially produced for MK isolation, MK isolation from mouse blood will be performed.

1.3 Hypothesis

Although PLTs play a critical role in hemostasis, angiogenesis and congenital immunity, their production mechanisms are still poorly understood. Therefore, PLTs are supplied entirely from blood donors, despite serious clinical concerns due to their immunogenicity and the risk of sepsis associated with them. Although the demand for PLT transfusion has increased significantly over the past decade, this process has resulted in significant PLT shortage due to a static donor pool, a 5-day PLT shelf life due to bacterial contamination and PLT disruption associated with storage. For these reasons, PLTs must be produced by alternative methods.

Existing microfluidic chip architectures are used based on bone marrow structure and 30-70 PLT formation is provided per MK. In recent studies, it has become evident that after the disintegration of MKs into PLTs under high shear stress in the lungs, PLTs are produced in the lungs.

The study has a high specific value in that it aims to produce PLTs from MKs with a channeled microfluidic chip that mimics the structure of the lung vein. The architecture of the existing chips is based on the bone marrow structure and 30-70 PLTs are formed per MK. In a recent article published in the journal Nature, it has become clear that after the disintegration of MKs into PLTs in the lung, most of the PLTs are produced in the lungs. The main innovation of the study of this thesis will be the investigation of this fragmentation mechanism by transferring lung capillaries architecture to microfluidic systems for the first time. Since this design is scalable, it will enable the production of chips that allow for the production of high amounts of PLTs.

2
THEORETICAL BACKROUND

2.1 Platelets

PLTs are a component of blood and responsible for stopping the bleeding. They are small cells that are derived from the MK [1-22]. PLTs are vital for hemostasis and thrombosis also, they play an important role in wound repair, inflammatory reactions, angiogenesis, lymph vessel separation, and tumor metastasis. In humans, approximately 1×10^{11} PLTs are formed per day [5].

Once PLTs are needed in larger quantities, units are derived entirely from human donors [3, 24, 25]. In the United States, more than 2.17 million apheresis equivalent PLT units are transfused per year at a cost of $> 10^9$ $/year. Although the demand for PLT transfusion has increased significantly in the last decade, this process has resulted in significant PLT shortage due to the presence of a static donor pool, 5-day PLT shelf life due to bacterial contamination and storage-related PLT degradation. In addition, artificial PLTs that produce in biotechnological processes did not replace physiological PLT products. It is; however, artificial PLTs should be produced by instant, high-throughput and rapid methods [6].

Microfluidics is a multidisciplinary field of technology, engineering, and science which has a huge potential to advance PLT formation. In this way, PLTs can be produced instantaneously from MKs that isolated and stored in advance. So far different microchannel designs have been employed to investigate the PLT formation [26]. These designs allow exposing higher shear stresses on the MKs that provides different behavior of elongation and formation of PLTs in laminar regime [2][3][5][7][9][27-29].

It is known that MKs break down into PLTs during transit to capillaries under high shear stress in bone marrow. As seen in Figure 1, this formation is predicted to be caused by prolonged pseudopods (particles) extending from mature MKs and

releasing PLTs, which are caused by cytoplasmic degradation or pro-PLT formation of MKs [5].

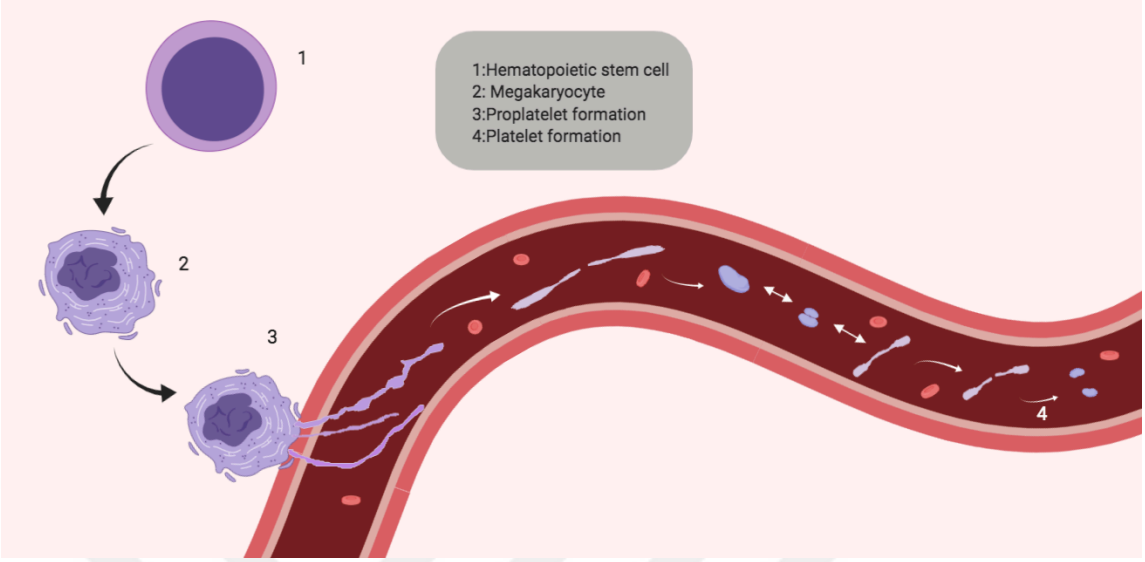


Figure 2.1 PLT production in bone barrow

Recent advances in the development of PLT production bioreactors aim to mimic the basic physiological properties of bone marrow, including extracellular matrix composition/hardness, tissue-specific microvascular endothelium, blood vessel architecture, and shear stress.

The first step of PLT production is the erosion of a MK. With the help of the erosion, ramified large pseudopodal-like structures to obtain uniform diameter (2-4 μm) tubular projections could be produced. ProPLT elongations extend outwardly at a steady rate of ~1 μm/min, and generally reach lengths of ~0.5-1 mm [15]. After entering the bloodstream, the proPLTs are converted to prePLT. Two PLTs are created from a proPLT with the help of the fission event [1].

However, it is not yet possible to fully understand how complex interactions in three-dimensional (3D) microenvironments regulate thrombopoietin, and the technical difficulties associated with the design and manufacture of biomimetic microfluidic devices are often underestimated and unreported.

Repetitive development of PLT bioreactors started with the seminal study of Lasky and Yang in 2003 and dramatically increased in recent years. In the literature, bone marrow geometry has been developed for PLT production and all designs

have developed in this direction [2][5][6][8][9]. The common aim of these studies is: Design and production of high-efficiency micro-bioreactors to obtain PLTs from MKs. Unfortunately, most of the studies have the same limitations: (i) Failure to achieve targeted PLT production efficiency, (ii) Accumulations, clogging, adhesions that occur in the designed microchannels, (iii) Inability to predict MK behavior at different shear stresses applied in microchannels.

Also, researchers have several approaches to micro-bioreactor geometries. Basically, they are focus on bone marrow geometry but they make some differentiations on the structural design. For example, they modified their micro-bioreactors with more than one inlet channels that have different angles to each other or added some slits or pores to their structures at different distances. When the studies about PLT productions investigate it can be observed that the effect of geometries cannot be explained very well [5][6][11]. PLT production should be examined not only in terms of yield but also in terms of fluid dynamics such as flow rate, shear rate, and shear stress. It is the point that needs to well-explanation of this kind of study.

2.2 Megakaryocytes

MKs derived from pluripotent stem cells and undergo multiple DNA replications without cell divisions by a unique process referred to as endomitosis [30]. Megakaryopoiesis is the process of MK maturation and differentiations from hematopoietic progenitor cell (HPC). On the other hand, thrombopoiesis is the process by which PLTs are released from MKs [14][30]. In the ex vivo human culture system, the time of the combination of the megakaryopoiesis and thrombopoiesis is occurring over two weeks although the time for in vivo is not known exactly [30].

During hematopoietic differentiation, HSC differentiate into a MK-erythroid precursor (MEP). MEP is a bipotential precursor that gives upward push to both megakaryocytic and erythroid lineages inside the bone marrow. The regulation of the MEP destiny is determined by using multiple transcription factors, together with MYB, RUNX1, GATA1, and FLI1. Expression of MYB in MEP favours the differentiation into erythropoiesis and MYB expression is down

regulated throughout megakaryocytopoiesis. GATA1 and FLI1 are vital all through MK differentiation. FLI1 is vital to enhance the pastime of GATA1 megakaryocytic promoters and repress the interest of erythroid promoters. RUNX1 has an important function in MK improvement and its deletion leads to impaired megakaryocytopoiesis. In addition, RUNX1 additionally interacts with GATA1 and FLI1 throughout MK differentiation. Another pivotal agent in MK lineage commitment is thrombopoietin (THPO, also termed TPO). THPO is a glycoprotein produced mainly via the liver and kidney that acts through the c-Mpl receptor and promotes MK differentiation, replication and maturation [7].

2.3 Microfluidics

Microfluidics are technology that processes small volumes of fluids (10^{-9} to 10^{-18} liters) with using channels different micron sizes. The first applications of microfluidic technologies have been beneficial analyzes carried out thanks to the advantages such as low sample usage, high sensitivity and high-resolution separation and detection, low cost and short analysis time [31]. The flow regime is laminar in microchannels [32-37]. Microfluidic systems (Figure 2.2) can be called lab-on-a-chip, bio-chip or micro-total-analysis-system depending on the area of use. Microfluidic systems can be considered as a miniature version of a traditional laboratory [31][38].

Microfluidics could be a central era in some of miniaturized systems which are being evolved for chemical, biological, and scientific applications [39]. In recent years, the generation of microfluidics has progressed swiftly and turn out to be an integral a part of many engineering and biomedical application [40]. Recent advances in microfluidics have brought forth new tools for analyzing flow-induced consequences on mammalian cells, with vital programs in cardiovascular, bone and most cancers biology. Micro scale systems have many advantages compared to macro scale systems. These advantages can never be achieved with macro scale. Microfluidics have developed very rapidly over the past 20 years and have become an indispensable part of biomedical applications. Microfluidics are dominated by the interface and diffusion forces that enable the processing and analysis of liquid samples on a micro scale [41].

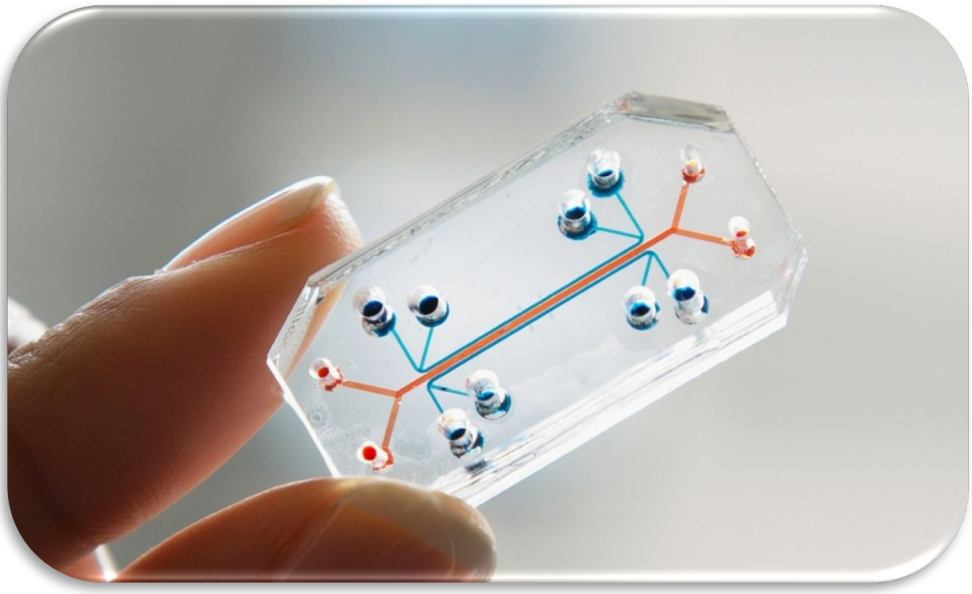


Figure 2.2 Microfluidic chip

Shear stress is a flow of outcomes from friction forces between liquid layers slipping over each other (Figure 2.3). The shear stress is maximal at the wall interface. For the case of steady incompressible laminar flow Navier–Stokes equations are used in Poiseuille flow. In biotechnological studies, microfluidic devices can be manipulated to mimic appropriate conditions for all types of cells. Some of the cells cultured in this way are bacteria, cancer cells, fibroblasts, etc. [42].

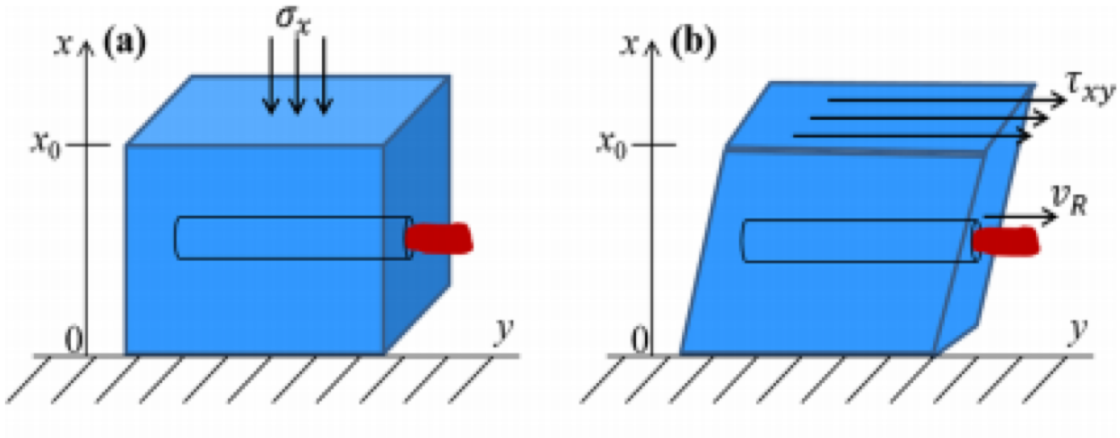


Figure 2.3 Shear stress effect on liquid layers

In biological analyses, the material of the microfluidic device is important. Silicon is steeply-priced and opaque to visible and ultraviolet light, so it can't be used with

traditional optical methods of detection. Also, glass is inappropriate material for the fabrication of microfluidic devices. So, neither glass nor silicone is suitable for work with biological systems [31].

When the studies conducted with microfluidic systems are examined, it is seen that the majority of the fabrications in these studies are carried out with a polymer called PDMS or poly (dimethyl siloxane) [43-50]. PDMS has a completely different structure than silicone and glass. This polymer is preferred due to its low cost, softness, elastomer and optical permeability properties [31][32][38][39][51][52].

2.4 Platelet formation in a microchannel

Recent advances in the development of PLT production bioreactors are intended to mimic the essential physiological properties of bone marrow, including extracellular matrix composition/stiffness, blood vessel architecture and shear stress, which are formed by tissue-specific microvascular endothelium. However, it is not yet possible to fully understand how complex interactions in three-dimensional (3D) micro-media regulate thrombopoietins, and technical difficulties in the design and manufacture of biomimetic microfluidic devices are often underreported and not appreciated. The recurrent development of PLT bioreactors started with the seminal work of Lasky and Yang in 2003 and accelerated in recent years (Figure 2.4). The 3D bioreactor, first published by Lasky and Yang (2003), has been used to capture embryonic stem cells in murines using a polyethylene terephthalate (PET) matrix and to provide direct hematopoietic differentiation using specific cytokines and inhibitors. Then, Sullenbarger et al., [27] reported a second 3D modular bioreactor containing polyester and hydrogel skeletons coated with fibronectin and thrombopoietin (TPO) that specifically promote MK maturation and proPLT formation from hematopoietic progenitor cells. Two years later, Lasky et al., brought operational improvements such as optimization of the bioreactor oxygen concentrations and medium perfusion, which resulted in a 3-fold increase in PLT production compared to previous iterations.

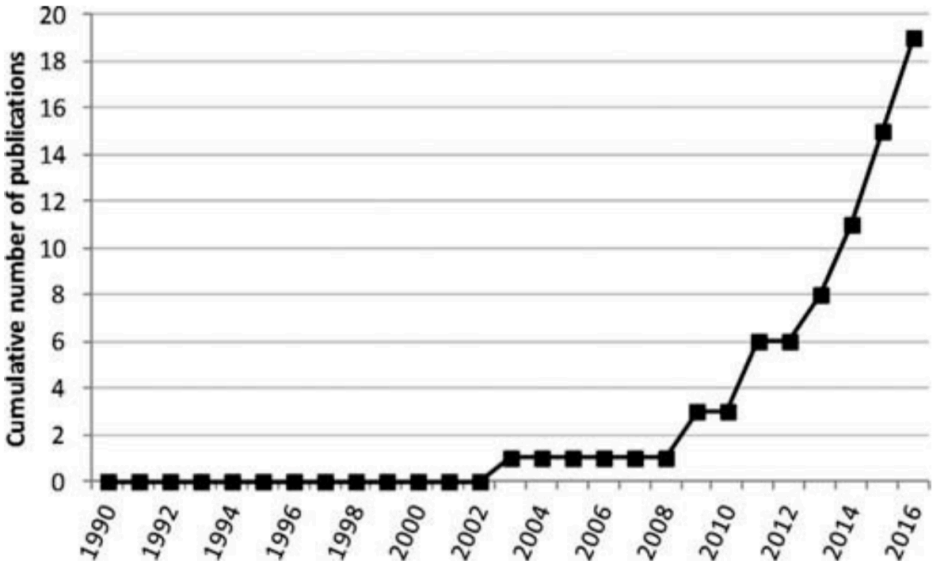


Figure 2.4 Number of published articles on PLT production

The concepts of continuous media perfusion, gas exchange and scaffold composition were introduced and advanced with the bioreactor designed by Lasky's research group; but the group was neither able to visualize the PLT production in real time nor to control the shear stress and pressure to mimic the fluid dynamics of the bone marrow properly [26].

Further efforts are underway to exploit new strategies and to conduct thrombopoiesis studies to produce PLTs for clinical transfusion. These include functional PLTs derived from clones of selected induced pluripotent stem cells (iPSC) in vitro, and MKs produced from functional PLTs infused in vivo in mice. Finally, it is known that several different proteins, such as fibrinogen (FBG) or von Willebrand factor (vWF), promote MK maturation and proPLT formation. However, many issues concerning the mechanisms underlying prothrombotic proliferation and PLT release, especially in humans, have not yet been solved. In particular, information on how the microenvironment surrounding MKs regulates PLT formation is necessary.

Table 2.1 summarizes the PLT production studies in the microbioreactors in the literature. The literature advances through bone marrow geometry for PLT production, and all designs have evolved in this direction. Because until recently, it was known that in human body, bone marrow was responsible for blood

production, and studies in the literature proceeded in this light of knowledge. However, Lefrançais et al., [23] noted that lungs play a key role in PLT production. Researchers who think that the lungs may be ideal bioreactors for PLT production due to the mechanical force of the blood, have indicated that this new knowledge will raise great repercussions in the scientific world. In this knowledge-based study on PLT production, microbioreactor designs will be more innovative and development-oriented, taking into account the lung geometry rather than bone marrow geometry.

Table 2.1 Literature review of the PLT formation from MKs in a microchannel

	Aim: Design and production of high-efficiency micro-bioreactors for obtaining PLTs from MKs	
	Limitations: • Failure to reach target PLT production yield • Accumulation, clogging, sticking in the designed microchannels • Failure to predict MK behaviors in different shear stresses applied in microchannels	
Literature	**Approach**	**Result**
Pallotta et al. 2011	As a result of studies carried out by PLTs containing microtubules coated with different protein constructs, the development of the process closest to the bone marrow structure has been achieved	To examine PLT production, an innovative 3D system has been developed that represents the first spatial reconstruction of the bone marrow environment. Passing through a vascular-like wall and spreading in a flow has been shown to be a fundamental step in creating functional PLTs
Nakagawa et al. 2013	Using a biomimetic artificial blood vessel system, evidence of the concept is demonstrated by a two-dimensional flow culture system, which allows the increase of PLT yield of human embryonic stem cell or pluripotent stem cell-derived MKs	To increase PLT yield, a new bioreactor was designed using two flows with a 60° angle between the main and the pressure flow. Thus PLT count increased 3.6-fold.

Table 2.1 Literature review of the PLT formation from MKs in a microchannel (Continued)

Thon et al. 2014	A scalable, third generation, human-derived pluripotent stem cell-derived MK-compatible PLT bioreactor was developed using biological inspiration engineering to fully integrate the major chemical and physical components of the bone marrow stroma under high-resolution live cell microscopy.	The designed bioreactor allowed for more than twice the PLT yield by expanding the control and stability of the microenvironment and greatly improving the duration of PLT release (reducing from 18 hours to 2 hours).
Avanzi et al. 2016	A method has been devised to reproduce the stages of MK differentiation and maturation, and a bioreactor is designed to mimic certain properties of the perivascular bone marrow microenvironment.	In the designed bioreactor, the number of PLTs obtained via shear flow from the MKs in the pseudo-3D membrane was increased efficiently.
Blin et al. 2016	Targeting the capture, extension and disintegration of MKs on hundreds of thousands of pillars placed in microchannels.	Unlike biomimetic membrane-based bioreactors, it has been shown that organized microchannels with microplate sequences can convert MKs and PLTs into high efficiency.
Martinez et al. 2017	A new 7 μm-slit bioreactor that mimic the bone marrow have been designed for PLT production. Not only shear forces but also flow patterns and uniform shear profiles have been analysis with CFD.	Shear rate in the slits increases from the inlet toward the outlet of the bioreactor and this reactor provides a more uniform shear profile compared to the literature.

3
MICROFLUDIC DEVICE

There is a static donor pool for platelets, which are needed in large quantities in the body. On the other hand, platelets have a shelf life of 5 days due to bacterial contamination and storage time restrictions. For these reasons, platelets must be produced by alternative methods. Existing microfluidic chip architectures are used based on the bone marrow structure, providing 30-70 platelet formation per MK. In recent studies, it has been clarified that most of the platelets are produced in the lungs, after imaging the fragmentation of MKs into platelets when they pass into capillaries under high shear stress in the lungs. For this reason, within the scope of the thesis studies, designs were made to target the production of platelets from MKs with a microfluidic chip with a channel that mimics the lung vascular structure, as well as the bone marrow structure.

3.1 Design of Microchips

Within the scope of the study, two different geometries were designed for the production of PLT from MKs. Simulation studies were carried out for both geometries, and the results were analyzed. After the simulation of these two designs, a geometry thought to be more suitable for the purpose was preferred, and studies were continued.

The geometry used in the initial design is a channel with pillars 500 μm wide, 50 μm deep, and 1200 μm long. The columns are arranged on an inclined hexagonal lattice. The angle between the central axis of the channel and that of the cage is fixed at 10° to ensure that each cell encounters at least one column. The diameter of the pillars is 20 μm, and the distance from the center to the center of these pillars is 85 μm. This geometry was suggested from Blin et al. (2016). Figure 3.1 shows this geometry. The geometry used in the second design is shown in Figure 3.2. The height of the channel is taken 50 μm in our simulations. It has an upper

stream, composed of pressure-flow (Q_1) and MK supply flow (Q_2), and a lower stream, called as main flow (Q_3).

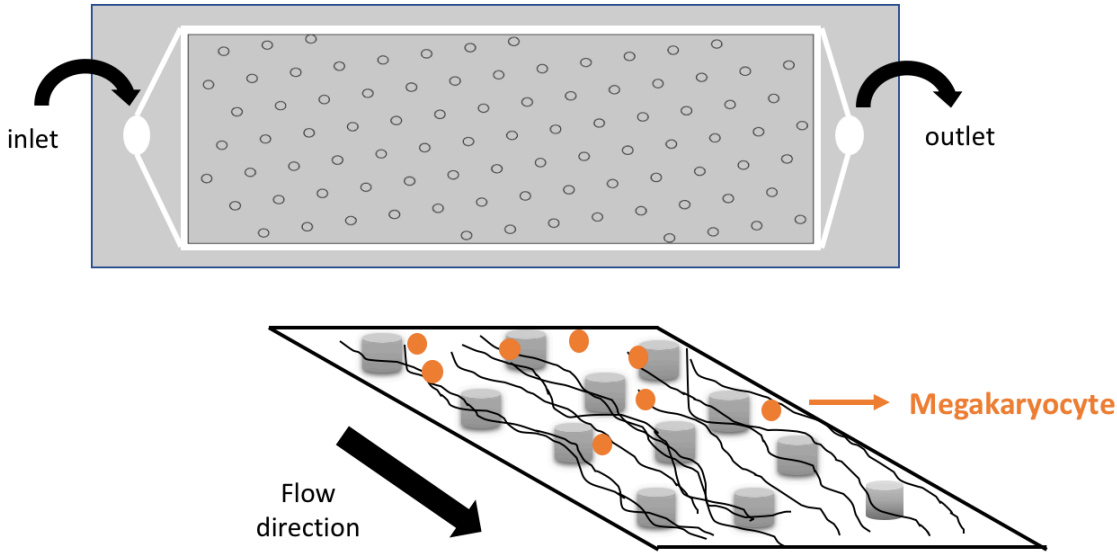


Figure 3.1 Microfluidic chip geometry

At the microscale, liquid streams flow laminarly at low Reynolds numbers (Re) - without turbulent mixing [22]. In this way, the flow that includes MKs can be suppressed by the pressure-flow by varying the flow rates of these inlets. The widths of the flows (w_1 and w_2) are linearly proportional to their flow rates. The inlet configuration of pressure and main streams in our design is Y-junction.

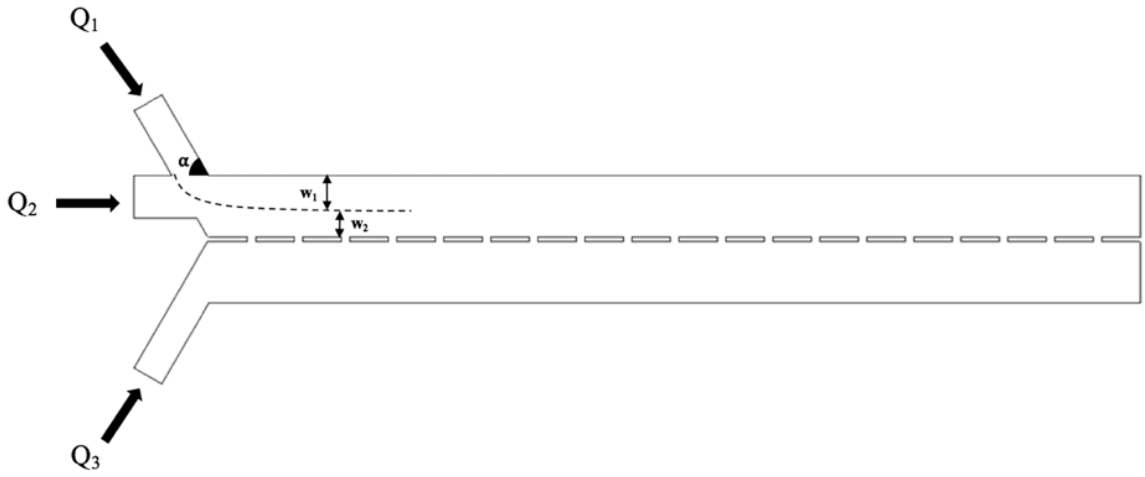


Figure 3.2 The design of the microfluidic bioreactor

3.2 Simulation of Microchips

The simulation of microfluidic chips will be done with the COMSOL Multiphysics package program, which is a finite element analysis method. Flow rates will be changed by considering different channel geometries and shear rate and shear stress values will be determined.

3.2.1 Finite element method

The description of the laws of physics for space- and time-dependent problems are usually expressed in terms of partial differential equations (PDEs). For the vast majority of geometries and problems, these PDEs cannot be solved with analytical methods. Instead, an approximation of the equations can be constructed, typically based upon different types of discretization. These discretization methods approximate the PDEs with numerical model equations, which can be solved using numerical methods. The solution to the numerical model equations is, in turn, an approximation of the real solution to the PDEs. The finite element method is used to compute such approximations.

3.2.2 COMSOL multiphysics

COMSOL Multiphysics® is a general-purpose platform software for modeling engineering applications. One can use the core package on its own or expand its functionality with any combination of add-on modules for simulating designs and processes based on electromagnetics, structural mechanics, acoustics, fluid flow, heat transfer, and chemical engineering behavior. The add-on modules and LiveLink™ products connect seamlessly via one integrated software environment. Shortly, it means that the modeling workflow remains the same regardless of what it is modelled.

COMSOL Multiphysics is an engineering design, and finite element analysis software environment for the modeling and simulation of any physics-based system. In other words, it is a powerful interactive environment for modeling and solving all kinds of scientific and engineering problems based on partial differential equations (PDEs). The COMSOL Multiphysics simulation software environment facilitates all steps in the modeling process – defining geometry,

meshing, specifying of any physics, solving, and then visualizing results. It is easy to access the power of COMSOL Multiphysics as a standalone product through a flexible graphical user interface or by script programming in the COMSOL Script language or the MATLAB language.

3.2.3 The governing equations and implementation of COMSOL

The Single-Phase Fluid Flow interfaces are based on the Navier-Stokes equations (3.1-3.2), which in their most general form as:

$$\frac{\partial \rho}{\partial t} + \nabla \cdot (\rho \mathbf{u}) = 0 \tag{3.1}$$

$$\rho \frac{\partial \mathbf{u}}{\partial t} + \rho(\mathbf{u} \cdot \nabla)\mathbf{u} = \nabla \cdot [-p\mathbf{l} + \tau] + \mathbf{F} \tag{3.2}$$

where **ρ** is the density (SI unit: kg/m^3), **u** is the velocity vector (SI unit: m/s), p is pressure (SI unit: Pa), **τ** is the viscous stress tensor (SI unit: Pa), **F** is the volume force vector (SI unit: N/m^3). For a Newtonian fluid, which has a linear relationship between stress and strain, Stokes deduced the following expression (3.3):

$$\tau = 2\mu\mathbf{S} - \frac{2}{3}\mu(\nabla \cdot \mathbf{u})\mathbf{l} \tag{3.3}$$

The Particle Tracing Module is available to assist with modeling problems. It is possible to model particle tracing with COMSOL Multiphysics provided that the impact of the particles on the flow field is negligible. First, it computes the flow field, and then, as an analysis step, it calculates the motion of the particles. Newton's second law defines the motion of a particle as (3.4):

$$m\frac{d^2\mathbf{x}}{dt^2} = \mathbf{F}(t, \mathbf{x}, \frac{d\mathbf{x}}{dt}) \tag{3.4}$$

where x is the position of the particle, m is the particle mass, and F is the sum of all forces acting on the particle. Examples of forces acting on a particle in a fluid are the drag force, the buoyancy force, and the gravity force.

The particle Reynolds number is defined as (3.5):

$$\mathrm{Re}_p = \frac{|\mathbf{u} - \mathbf{u}_p| 2\mathrm{r}\rho}{\mu} \tag{3.5}$$

where $\mathbf{u}$ is the velocity of the fluid, $\mathbf{u}_p$ is the particle velocity, r is the particle radius, ρ is the fluid density, and μ is the dynamic viscosity of the fluid.

$$\mathbf{F} = \pi r^2 \rho |\mathbf{u} - \mathbf{u}_p| (\mathbf{u} - \mathbf{u}_p) \left[1.84 Re_p^{-0.31} + 0.239 Re_p^{0.06}\right]^{3.45} \tag{3.6}$$

The empirical expression for the drag force, according to Khan and Richardson is in (3.6) [53].

3.2.4 Flow properties

The flow can be considered as laminar if the Reynolds number given in the (3.7) is smaller than 2000.

$$\mathrm{Re}_{\max} = \frac{\mathrm{u\ L}}{\mathrm{v}} \tag{3.7}$$

The Laminar Flow module of COMSOL uses the Eq. 3.8 and Eq. 3.9 for the flow at a steady state.

$$\rho(\mathrm{u} \cdot \nabla)\mathrm{u} = \nabla \left[-\mathrm{pl} + \mu(\nabla \mathrm{u})^{\mathrm{T}}) - \frac{2}{3}\mu(\nabla \cdot \mathrm{u})\right] + \mathrm{F} \tag{3.8}$$

$$\nabla(\rho \mathrm{u}) = 0 \tag{3.9}$$

The inlet conditions are entered to the system with the (3.10). In general, 1 meter of entrance length (L_{entr}) is taken.

$$L_{entr} \nabla_t \cdot [-\mathrm{pl} + \mu(\nabla_t \mathrm{u} + (\nabla_t \mathrm{u})^{\mathrm{T}})] = -\mathrm{p}_{entr} \cdot \mathrm{n} \tag{3.10}$$

3.2.5 Particle tracking

In the particle tracking, the Newtonian formulation is used with transient release type. The time derivative of momentum will yield the force applied to the particle at a given time, as calculated in Eq. 3.11.

$$\frac{d(m_p v)}{dt} = F_t \tag{3.11}$$

$$F = \frac{1}{\tau_p} m_p (u - v) \tag{3.12}$$

$$\tau_p = \frac{\rho_p d_p^2}{18\mu} \tag{3.13}$$

This force will be used by COMSOL to estimate the particle' position at the next iteration step by using the Stokes Law, which is given in (3.12) and (3.13).

3.3 Fabrication of Microchips

Microfabrication, the production of tiny structures, is very important to technology and science. Microstructures support lots of technologies and penetrate society through their role in some areas. Photolithography is a technique used for microfabrication. With the assist of photolithography, the patterning needed in microfabrication is achieved. Photolithography has some disadvantages such as;

- Expensive
- Difficulty in applied to non-polar surfaces
- Generally, there are limited alternative materials can be used
- Especially for the chemistry, biochemistry, and biology, it is difficult to control the chemistry of pattern surfaces

Because of the disadvantages, scientists wished to develop new techniques that complement photolithography. In 1998, a new technique called soft lithography was developed [54].



Figure 3.3 Special clothes for the cleanroom

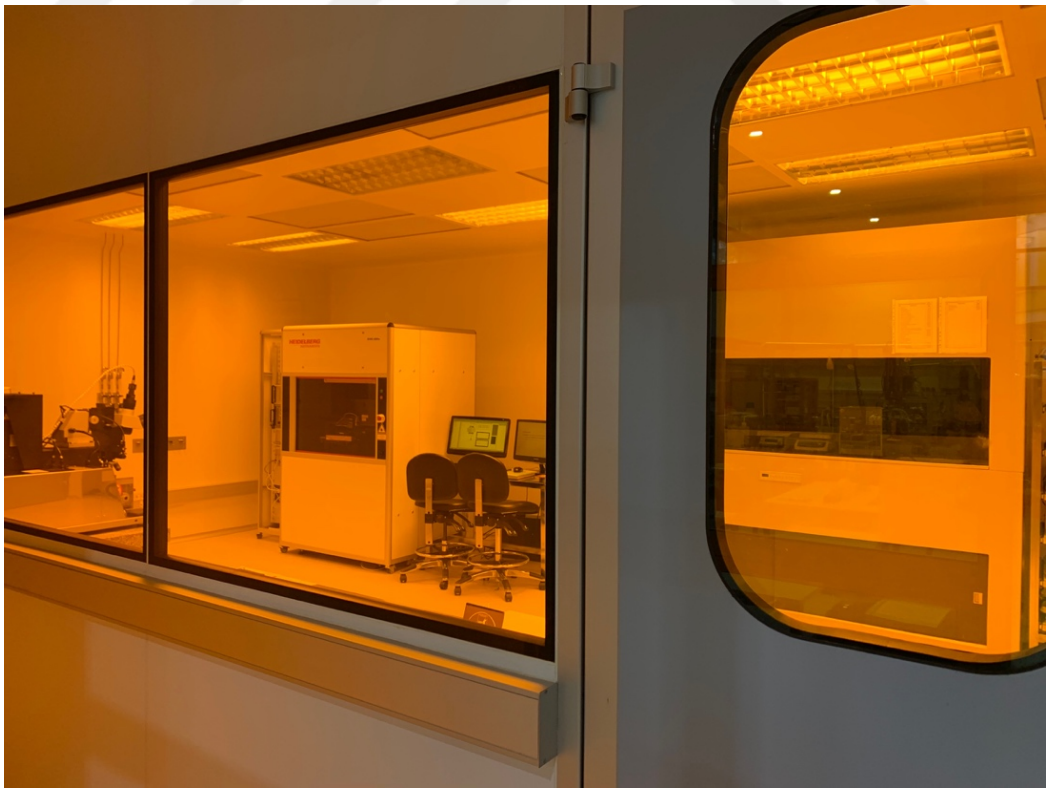


Figure 3.4 An image taken from out of the cleanroom

There are two main features for soft lithography; the first one is fabricating the pattern transfer elements by molding with the use of elastomeric materials and the second one is an improvement of techniques that mold various biochemicals [55].

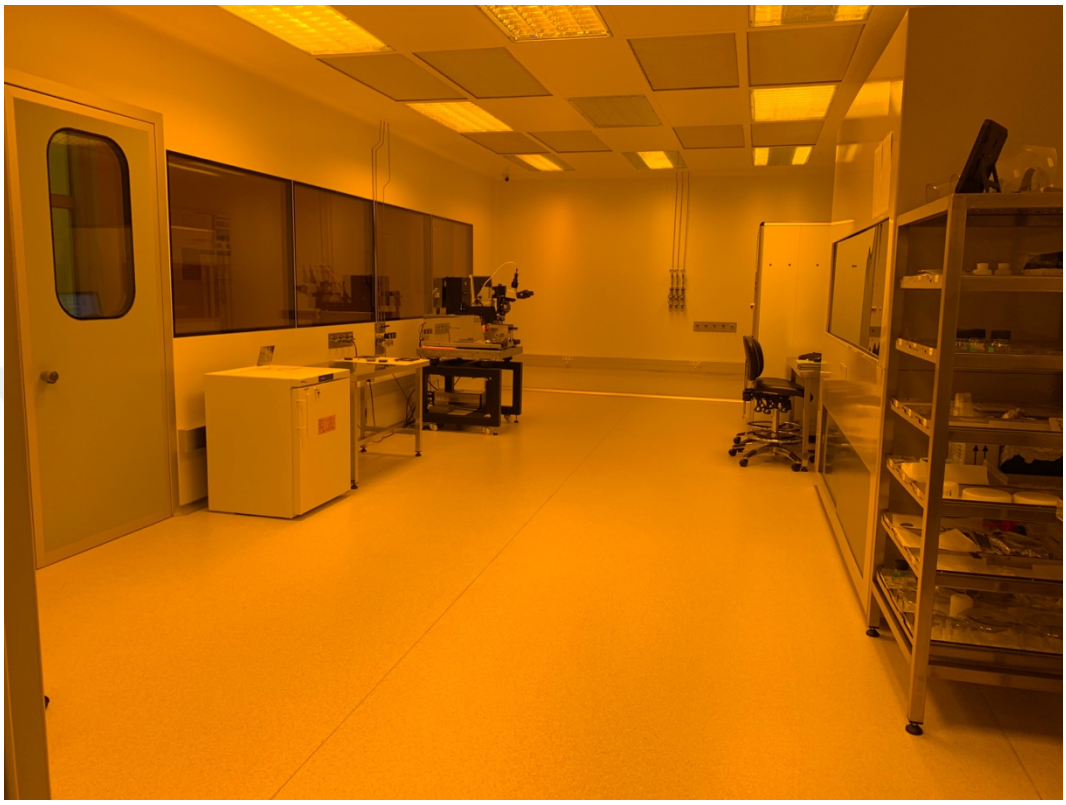


Figure 3.5 An image taken from inside of the cleanroom

Soft lithography is a various set of techniques that encompasses replica molding using an elastomeric material, especially polydimethylsiloxane (PDMS), to fabricate microfluidics and pattern the surfaces using PDMS stamps. The prevalent procedure used for making PDMS microchannels includes fabricating a silicon master with patterned features composed of a photoresist (e.g., SU-8). In this process, silicon wafers are coated with photoresist and then exposed to ultraviolet (UV) light through a mask with the desired pattern [56].

Cleanroom facilities and specific equipment are the basic requirements for the fabrication of microfluidics (Figure 3.3-3.8). There are several fabrication techniques and equipment for producing two- and three-dimensional microstructures with integrated modules [57].



Figure 3.6 The chemical bench in the cleanroom



Figure 3.7 The general look of cleanroom

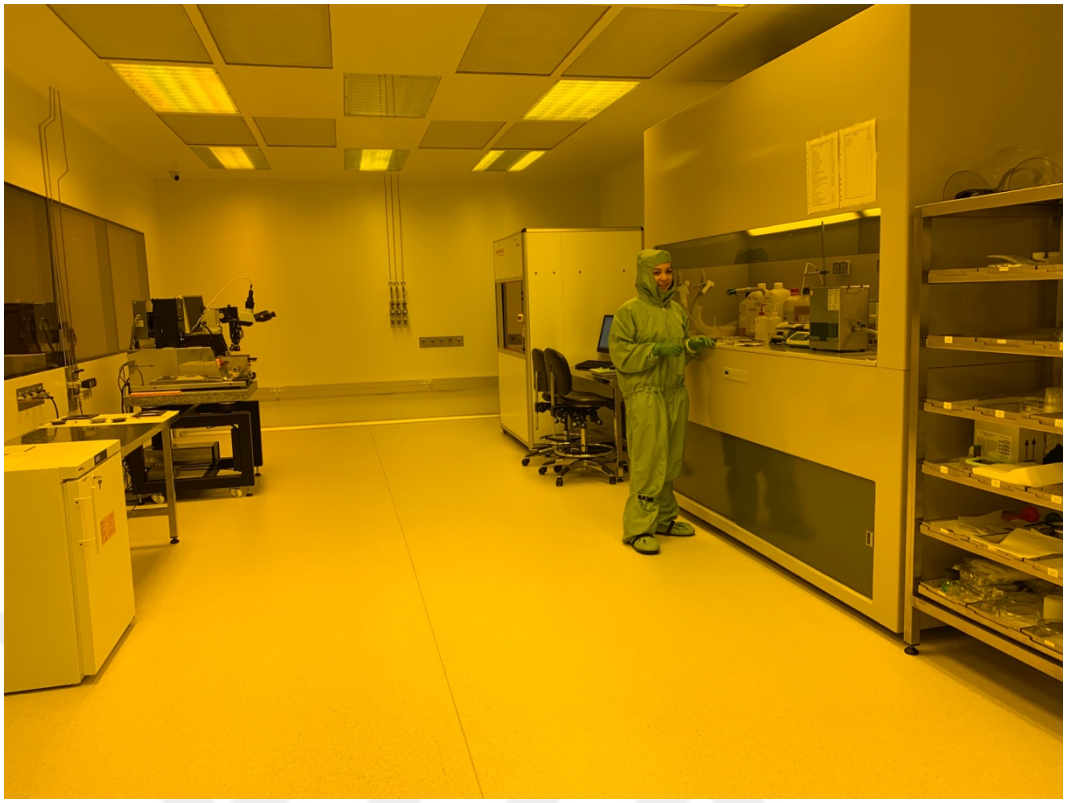


Figure 3.8 Studying in cleanroom with special clothes

3.3.1 Mask design

Lithography is a technique used to transfer the chip design determined by the designer to the silicon wafer. The design drawn by the computer program (CAD) is primarily transferred to the mask. The type of mask is determined according to the size of the chip dimensions. Chromium masks are preferred in thinner features, but acetate masks may be preferred for sizes over 50 μm. The produced microfluidic channel width (500 μm) allows the use of acetate masks, and the acetate mask used for the microfluidic channel is shown in Figure 3.9.

3.3.1.1 Chrome photomask production

As mentioned in the previous part, photolithography is based on the principle of coating a light-sensitive chemical material (photoresist) on a specified surface in the desired thickness and then transferring the mask pattern onto the surface by passing ultraviolet light (UV) over a pre-designed photomask. Accordingly, the photomask used for the photolithography process is an important factor in the

microfluidic channel fabrication process. In this part, the fabrication process of the chrome photomask used during the photolithography process is explained.



Figure 3.9 Acetate mask used in the production of microfluid channel

Within the scope of the targets determined in the study, the width of the microfluidic channels produced in the first stage was designed to be at least 50 μm, and the photomask used in the production phase of these microfluidic channels was determined as an acetate mask. Despite the restriction of the dimensions of microfluidic channels made with an acetate mask to a minimum of 50 μm, the microchip was efficient in the production stage in terms of fabrication quality, economy, and ease of production. However, in accordance with the studies carried out, the targeted microfluidic channel designs decreased to sub-10 μm. Since the previously used acetate mask is not suitable for use for new targets, chrome photomask production was targeted and produced successfully. Although the supply of the mask material and the production process is complex compared to the production of acetate masks, it allows the production of the channels of the desired width with the appropriate quality, making the production of chrome photomasks necessary.

Although the supply of the mask material and the production process is complex compared to the production of acetate masks, it allows the production of the

channels of the desired width with the appropriate quality, making the production of chrome photomasks necessary.

The transfer of the design to the chrome-plated glass surface and making it into a mask was done with the mask printer device (Heidelberg DWL 66fs) (Figure 3.10) located in Gebze Technical University Micro / Nano Device Production Laboratory.

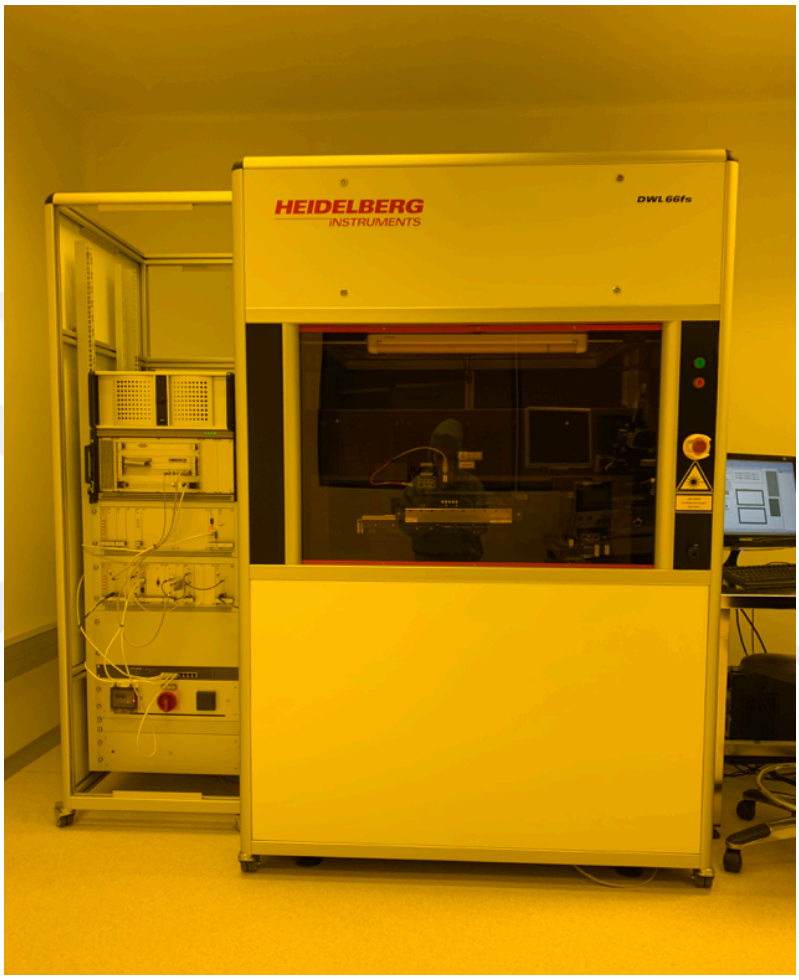


Figure 3.10 Heidelberg DWL 66 fs mask printer device

The first step of production is to create the mask design by a computer-aided design (CAD) software. Then maskless photolithography instrument prints the design on a photoresist coated chromium/glass substrate. The displayed pattern is developed in the particular developer solution of the photoresist to create a template on chrome (Figure 3.11). Depending on the type of photoresist used, chromium is etched from the areas where UV light is desired to be transferred. After the etching is complete, the remaining photoresist is removed, the plate is cleaned and then stored for use in an optical printer.

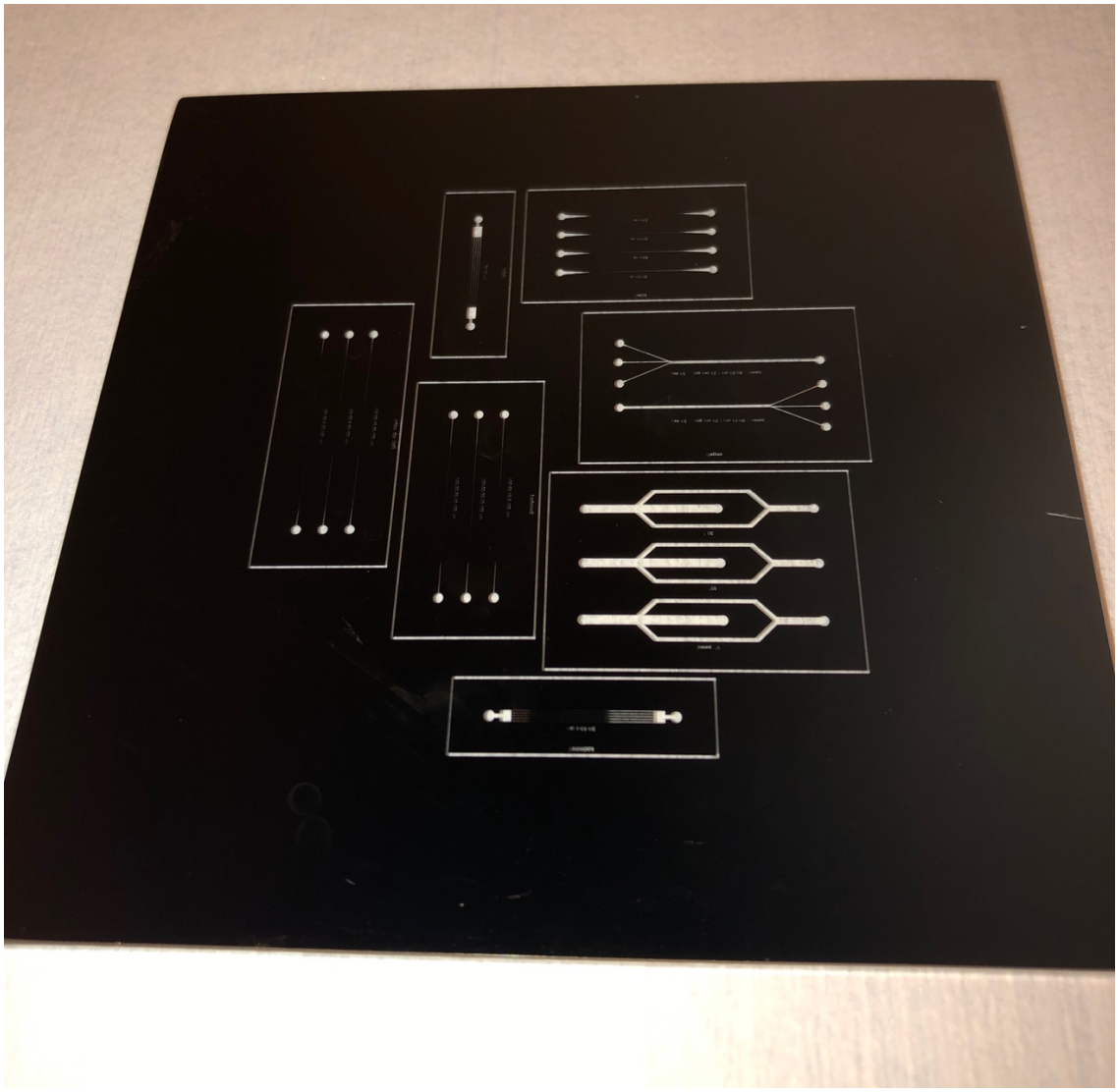


Figure 3.11 Chrome photomask after writing process

The 4 x 4 x 0.090-inch plate was cleaned with acetone and isopropyl alcohol for 3 minutes. Drying was carried out on the heating table at 110 °C for 20 seconds. AZ 1505 positive photoresist was coated at 3000 rpm, 30 sec and 1000 rpm/sec on the plate that was left to be cooled for 10 seconds, and then annealed on the heater table for 30 minutes at 103 °C. After the cooling process is completed, the plate was placed on the maskless lithography device (Heidelberg DWL 66fs), and the mask design, previously drawn in the CleWin design program, was transferred to the mask printer program. Writing took approximately 4 hours.

After the writing process, for the etching of the written parts of the AZ 1505 positive photoresist, the developer chemical was kept in AZ 726 MIF solution for 55 seconds and at the end of the process, the photoresist was transferred to the

design. The plate was washed with DI water for 30 seconds. Each micro fluid channel design was examined under an optical microscope to check the accuracy of the mask design.

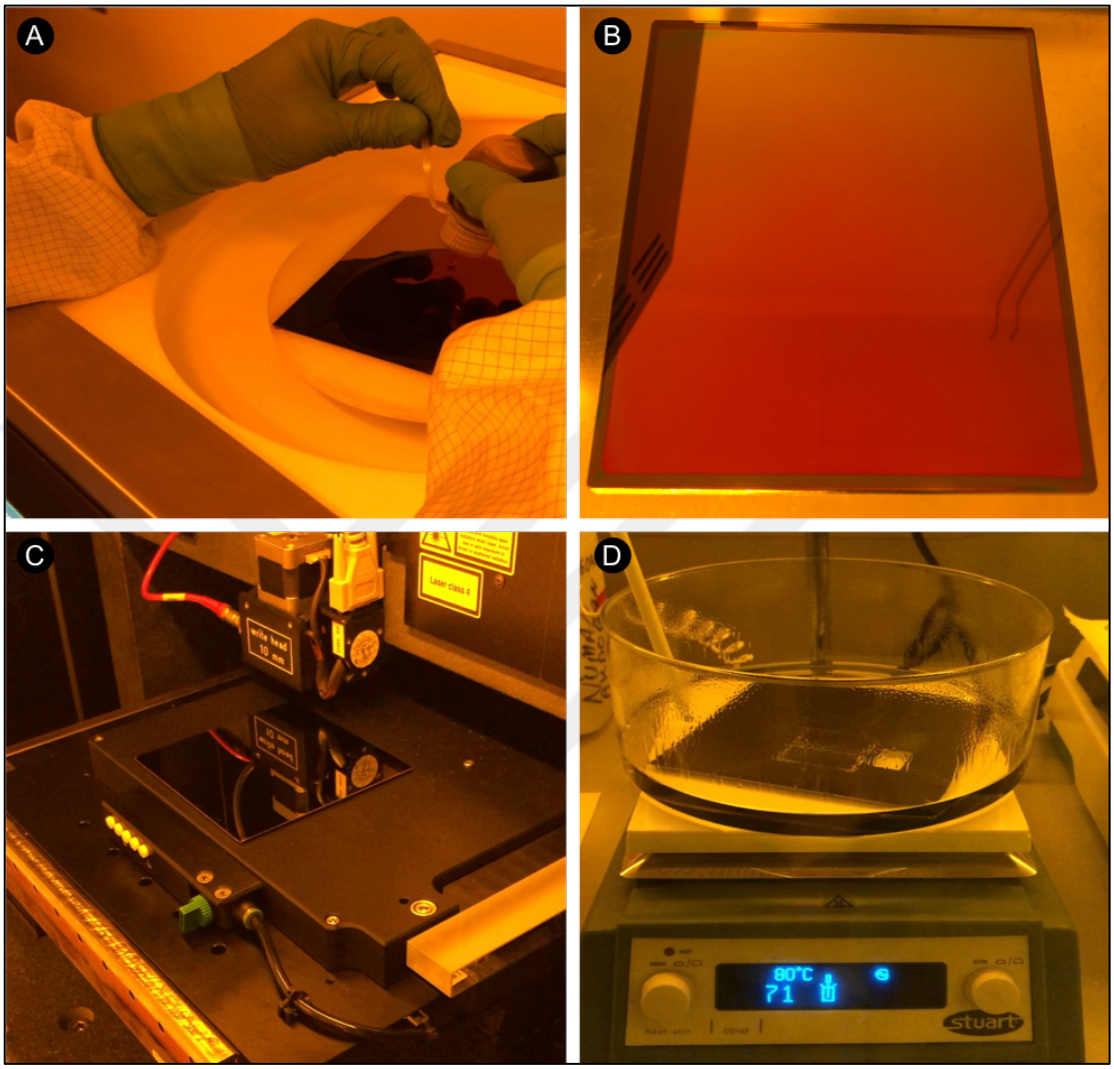


Figure 3.12 Chrome photomask production steps. A) Placing the cleaned chrome photomask in the spin coater and dropping the AZ 1505 positive photoresist B) AZ 1505 photoresist coated chrome photomask display C) AZ 1505 photoresist coated chrome photomask placed in the mask printer D) Representation of chrome photomask in chrome etching chemical.

Covering the plate with a positive photoresist ensures the correctness of the writing process after the mask was printed, without protecting the chrome structure yet, and protecting the resist-coated areas during the etching process of

the chromium on the mask. Thus, only chromium in places not covered with resist will be etch and transferred to the design mask. Finding the remnant of the photoresist previously covered in case it is possible, it was kept in AZ 1505 solvent (remover) for 5 minutes at 80 °C. The photomask, cleaned with acetone and isopropyl, was dried with nitrogen gas. Chrome photomask, which was made ready for use as a result of all these processes, was kept in a special box in a convenient way for continuous use. Production of chrome photomask is shown in Figure 3.12.

3.3.2 Silicon wafer mold production by photolithography

Photolithography is the process of patterning a photoresist (photosensitive polymer), which is coated on a silicon wafer, using a previously prepared mask. The UV light at a given wavelength is transmitted via a mask to the photoresist deposited on the silicon wafer in this wavelength. The micro- or nano-sized features on the mask are transferred to the wafer at the end of a series of chemical processes. Lithography is basically; It consists of mask design, photoresist coating process of silicon wafer, UV light exposing, and photoresist developing.

The medium in which the lithography is to be made must be free of particles and sterile. This is why lithography is carried out in areas called cleanrooms. The sub-structures of the microfluidic-based chip are fabricated on silicon wafer. The reason of the yellow light in cleanroom is to eliminate the UV spectrum may exist white light.

The photoresist is a coating material which is a photosensitive polymer structure. There are two types of photoresist as positive and negative. When a positive photoresist is used, the areas of the silicon wafer that are exposed to UV light dissolve during the following chemical etching process and move away from the silicon wafer surface. When a negative photoresist is used, light areas are hardened and insoluble during the wear process, and the photoresist in the unsealed area dissolves away from the silicon bottom surface. The positive and negative photoresist difference is shown in Figure 3.13.

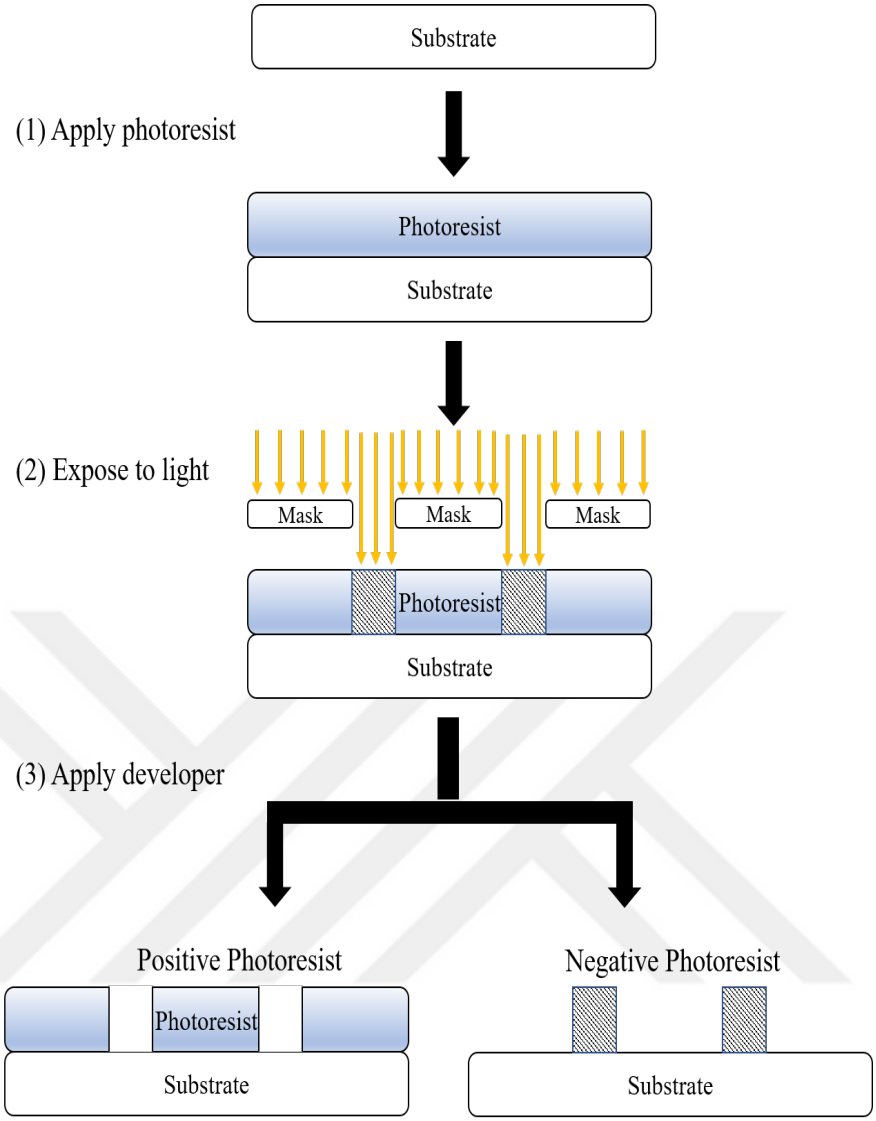


Figure 3.13 Difference between positive and negative photoresist in applications

In this study, firstly, 2500 mm long, 100 μm high, and 500 μm wide microchannel production was carried out in cleanroom conditions by the photolithography. Figure 3.14 shows the measured values under the microfluid channel and microscope image produced. The steps of manufacturing the microfluidic channel are described in detail below.

3.3.3 Photoresist coating process

Homogenous coating of the photoresist on the silicon wafer with the desired thickness is made by a spin coating device. The silicon wafer is centered on a vacuum tray with the spin coating device, and the vacuum is fixed on the table

when the silicon bottom is rotated at high speeds. The photoresist fluid, which is poured into the middle of the silicon bottom, is spread over the entire surface of the silicon wafer with centrifugal force, which is formed by the rotation of the silicon bottom.

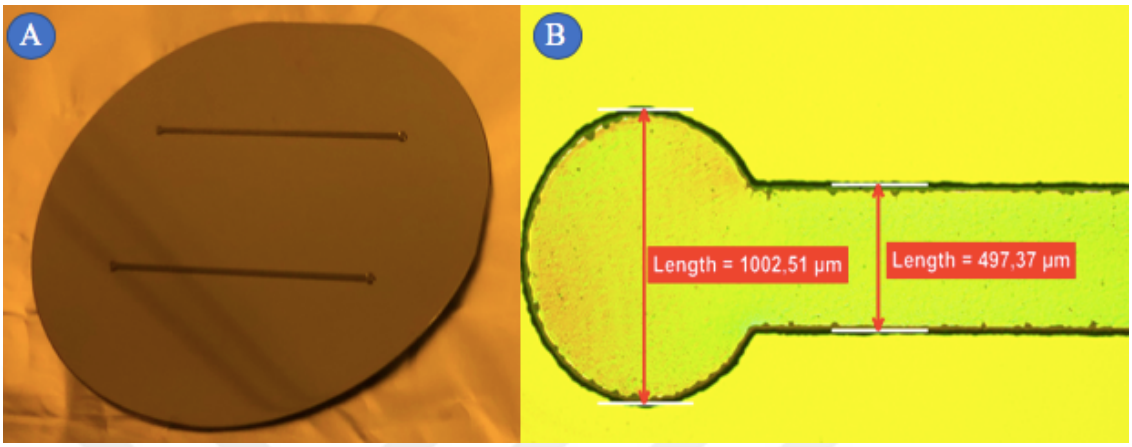


Figure 3.14 A) Mold image produced using photolithography with SU-8 photoresist on silicon wafer B) Microscope image and dimensions of the micro-fluid channel produced

The spin coating process controls these parameters; the rotational speed, the acceleration, and the number of times to repeat. These parameters affect the photoresist thickness and thickness change on the silicon wafer.

According to the information obtained from the application procedures of the SU-8 2100 negative photoresist, a coating of 100 µm was obtained at 30 sec, 3000 rpm, and 300 rpm/sec.

3.3.4 Soft baking of SU-8

The curing process is carried out by holding the silicon wafer on a table set to a certain temperature for a specific time. During this process, the amount of solvent in the layer of the photoresist, which is between 80-70 %, falls to about 20-10 %, and the resist in free volume decreases.

Curing is carried out for the following purposes;

- Improve adhesion of the photoresist to the surface.
- Blowing the solvent contained in the photoresist prevents the formation of bubbles caused by N_2 gas released during lithography.

- Decreasing the amount of solvent increases the difference between the dissolution rates of the light and unadorned areas during the wear process. The resolution of light-free areas is significantly reduced.

According to the information obtained from the application procedures of SU-8 2100 negative photoresist, curing was applied at 65 °C for 5 min and then at 95 °C for 20 min.

3.3.5 UV exposure

In the exposure process, the photoactive substance in the photoresist structure reacts with exposure to a particular wavelength of light. The parameters determined by the user in the UV beam device and affecting the size and profile of the shapes formed on the surface of the silicon wafer are the light wavelength and the application time. The unit of the illumination dosage is Joule / m^2, and the device adjusts the amount of energy per unit area by changing the length of time the curtain provides the passage of UV light. The microfluidic channel production was performed with the SUSS MicroTec MJB4 brand device and is shown in Figure 3.15. UV light exposure was applied for 10 sec in accordance with the information obtained from the application procedures of SU-8 2100 negative photoresist.

3.3.6 Post bake

According to the information obtained from the application procedures of SU-8, the final curing values were applied at 65 °C for 5 min and then at 95 °C for 10 min during the production of the microfluidic channel.

3.3.7 Chemical etching process (Developer)

The dissolution of the carboxyl acid formed in the photoresist structure by UV light in the subsequent step in the basic solution is defined as the chemical etching process. After this process, the shapes on the mask are transferred to the surface of the silicon wafer when using a negative photoresist.

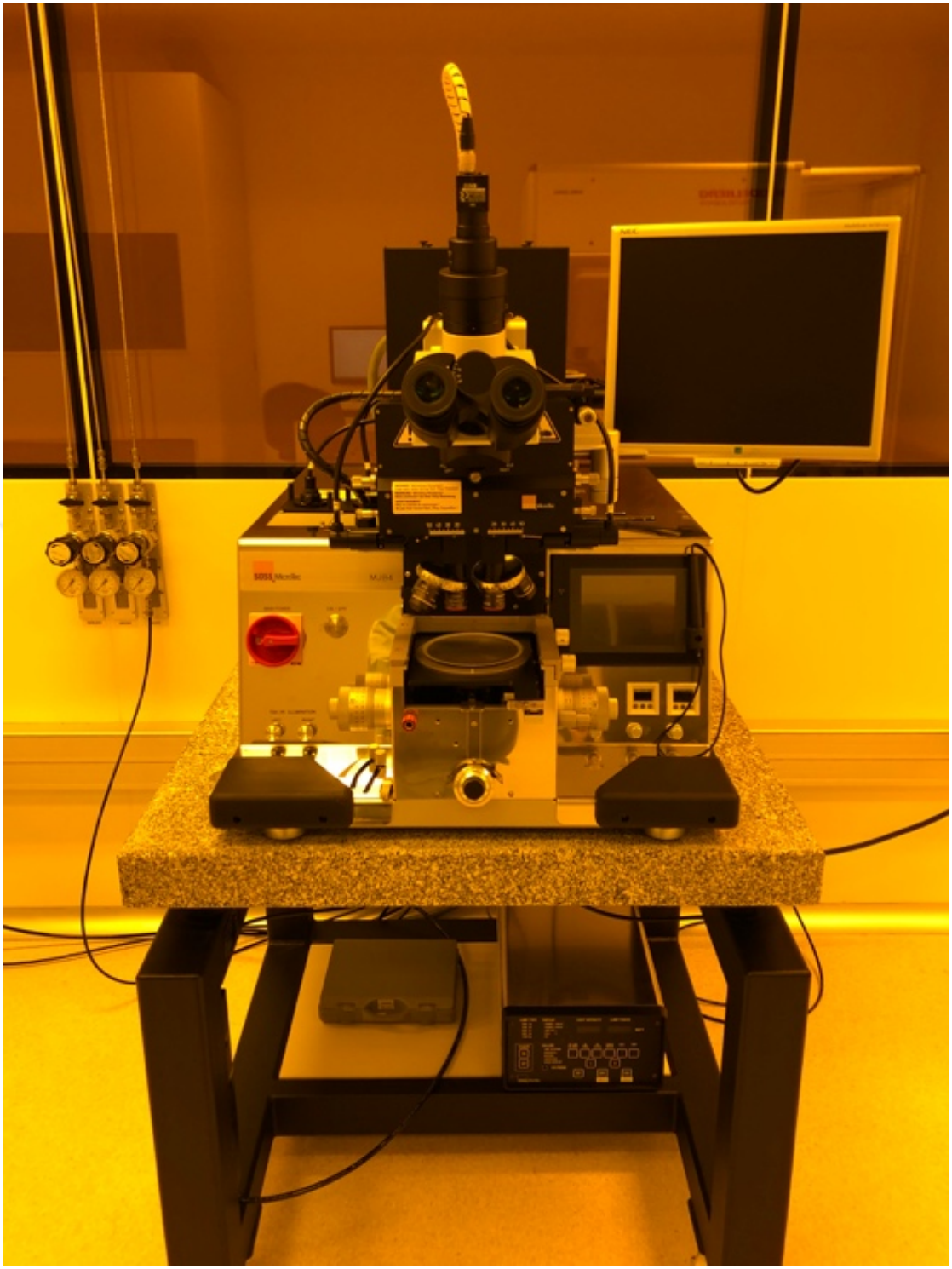


Figure 3.15 SUSS MicroTec Lithography Device

Based on the information obtained from the application procedures of the SU-8 2100, it was allowed to stand in SU-8 developer chemicals for 10 minutes, and the silicon wafer of the microfluidic channel was formed. After chemical etching, the resulting product is washed with deionized water and dried with nitrogen gas.

SU-8 2100 application parameters;

Application parameters determined according to SU-8 2100 negative photoresist thickness values are shown in Table 3.1.

Table 3.1 SU-8 2100 application parameters

Channel height	Coating speed, acceleration and duration	Pre-baking time	UV-lighting time	Last baking time	Chemical etching time
100 μm	1)500 rpm, 5-10 sec, acceleration: 100rpm/sec 2)3000 rpm, 30 sec, acceleration: 300rpm/sec	65 ºC-5min 95 ºC-20 min	9.6 sec	65 ºC-5 min 95 ºC-10 min	10 min
200 μm	1)500 rpm, 5-10 sec, acceleration: 100rpm/sec 2)1500 rpm, 30 sec, acceleration: 300rpm/sec	65 ºC-6.5 min 95 ºC-40 min	12.6 sec	65 ºC-5 min 95 ºC-14 min	16.5 min
250 μm	1)500 rpm, 5-10 sec, Acceleration: 100rpm/sec 2)1100 rpm, 30sec, acceleration: 300rpm/sec	65 º C-7 min 95 º C-52.5 min	14.4 sec	65ºC-5 min 95 ºC-17.5 min	18.5 min

3.3.8 PDMS chamber via soft lithography

Another critical step in microfluidic channel fabrication is PDMS chamber production. The SU-8 structure formed via photolithography on the silicon wafer transferred to the PDMS. The fabricated PDMS part was irreversibly bonded with the glass wafer. PDMS is a silicone-based organic polymer having the general formula $CH_3[Si(CH_3)_2O]_n$ $Si(CH_3)_3$. Biocompatibility, elastomeric structure, optically viewable, gas permeability for the cells are the unique properties of PMDS. PDMS, one of the strongest elastomers in terms of strength, provides the possibility of re-usability and provides multiple experiments on a microfluidic platform [58].

3.3.8.1 Preparation of the PDMS mixture

Firstly, a PDMS liquid mixture was prepared. The mixture consists of two materials, the liquid PDMS prepolymer, and the hardening agent. Air bubbles formed in the PDMS mixture, which was homogeneously mixed in a 10:1 ratio by weight. Since any air bubbles that could be formed along the microfluidic channel would disrupt the experimental course, the mixture was kept in the vacuum desiccator for 20 minutes, and the air bubbles were removed. Thus, the PDMS polymer mixture was made suitable for pouring onto the silicon wafer. The mold produced by photolithography was treated with isopropyl alcohol - acetone - isopropyl alcohol respectively and dried with nitrogen gas. The silicon wafer mold was placed in a petri dish, and the PDMS mixture prepared on it was poured slowly.

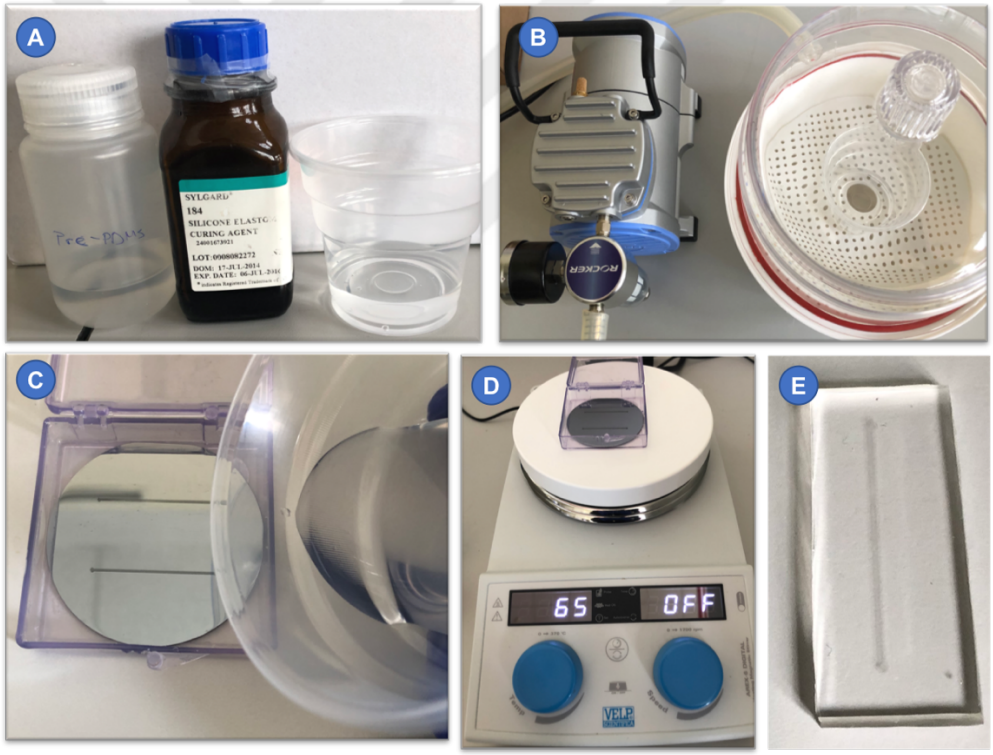


Figure 3.16 (A) The PDMS prepolymer and hardening agent were mixed in a 10:1 ratio. (B) Air bubbles in the mixture were removed by taking the vacuum desiccator. (C) The mixture was poured onto the silicon wafer mold. (D) Hardening for 3 hours at 65 °C on the heater. (E) The PDMS separated from the silicon wafer was cut to size and the channel entrance and exit holes were drilled

The petri dish was placed on the heater and the PDMS mixture was allowed to solidify at 65°C for 3 hours. The solidification takes place on the basis of the reaction between the hydrosilane (SiH) group in the PDMS polymer and the vinyl ($SiCH = CH_2$) group. The PDMS structure, which was allowed to cool, was separated from the silicon wafer. The produced PDMS structure is cut and arranged according to the dimensions to be used. The channel entry and exit holes were drilled using the punch. The PDMS mold of the microfluid chip design was produced as a result of the processes [59]. Figure 3.16 shows the construction steps of the PDMS mold.

3.3.8.2 Bonding of PDMS microfluidic chip

For microfluidic chip bonding, the PDMS mold and the glass wafer should be connected irreversibly.

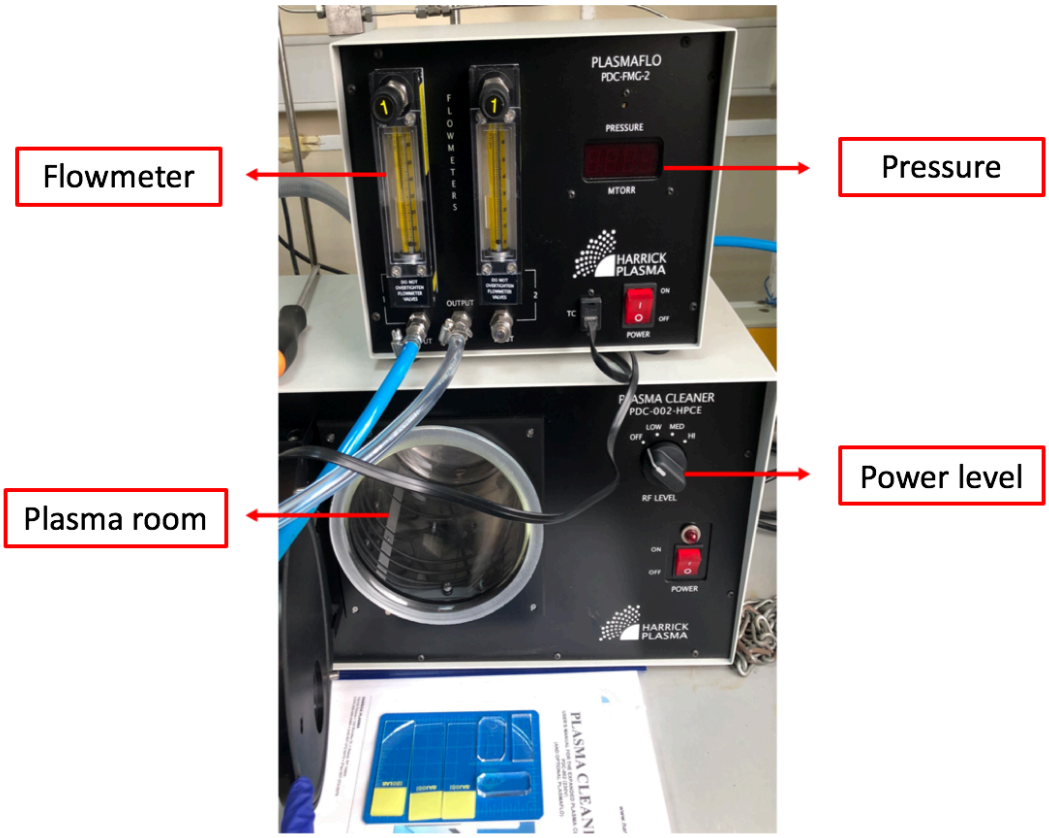


Figure 3.17 Harrick Plasma Cleaner device

The bonding of the PDMS chamber with the glass wafer was achieved by forming an oxygen plasma medium in the “Harrick Plasma Cleaner” device shown in Figure

3.17. The irreversible bonding of the glass surface and PMDS mold, which is an important step of the microfluidic channel fabrication, was performed using an oxygen plasma device. The Si-CH_3 bonds of the PDMS layer with the hydrophobic surface are combined with the oxygen atom in oxygen plasma and are converted to the Si-OH bonds, and thus the surface is rendered hydrophilic. Since this is a reversible process, the surfaces should be contacted with glass substrate immediately (less than 10 minutes) after the oxygen placement; otherwise, the surfaces will return to their hydrophobic state.

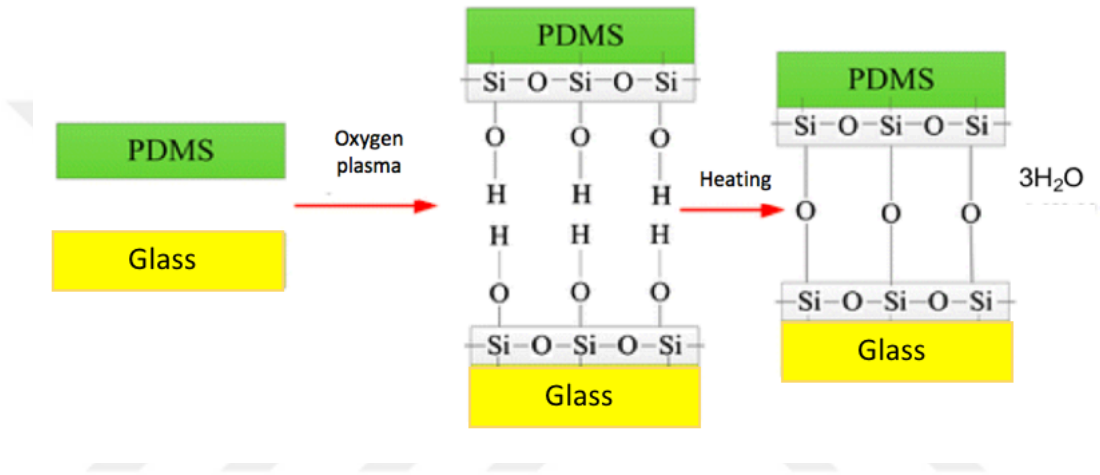


Figure 3.18 Binding between the PDMS and the glass surface by covalent bond interaction takes place between the surfaces [56]

When the glass surface and the PDMS layer are brought into contact, they have Si-O-Si bonds and are connected irreversibly. In this basic scope, the surfaces of the glass substrate and the PDMS layer were placed in the device, and the oxygen plasma was applied at 200 mTorr pressure at a 125 sccm flow rate for 90 seconds [60]. The parts with active surfaces removed from the plasma medium were contacted, and a covalent bond was formed between the surfaces, as shown in Figure 3.18.

It was heated at 65 °C for 45 min with the 0.5 kg weight on it. The parameters were determined within the scope of the literature research, and the wear on the surfaces is observed if it is applied more than the optimum dose.



Figure 3.19 Single channel microfluid chip

As a result of the process, the glass surface and the PDMS structure were bonded irreversibly, and the microfluidic channel design was completed. The single-channel microfluidic channel is shown in Figure 3.19.

4
RESPONSE SURFACE METHODOLOGY

It is a mathematical and statistical method used to solve related problems for science and engineering. It is widely used in mathematical modeling and optimization of technological processes. Response surface method; includes experimental strategy, mathematical model, and statistical results. The advantage of experimental design over other methods is that all parameters can be changed simultaneously. In experimental studies conducted with other methods, the parameters other than the investigated parameter can be kept constant and the change of that parameter can be examined. This requires a large number of experiments. In the experimental design, the number of experiments decreases as the factors can be examined simultaneously. The RSM method ensures that experiments are carried out at the points where most information is available. The steps to be determined in the experimental design methods are given below.

1. The condition and definition of the problem should be made.
2. Factors, levels, and range should be selected.
3. Answer variable should be selected.
4. Experimental design matrix should be created.
5. Experiments should be carried out.
6. Statistical analysis should be given.
7. Results should be evaluated.

The most crucial point to create the mathematical definition of the processes is achieving maximum information with a minimum number of experiments. Internal interactions and statistical design between variables are performed by conducting a series of experiments previously determined. Regression and correlation analysis accurately give process variables and optimum conditions. The mathematical function is the answer function that contains the optimum parameters (4.1)

$$Y=f(x_1, x_2, \ldots\ldots,x_k) + \lambda \quad (4.1)$$

Here x_1, x_2, …, x_k are independent variables and are called factors. The geometric representation of the response function in factorial dimensions is called the response surface. If the answer of the independent variables defining the system is linear, the function is given in the first order (4.2).

$$Y=B_0 + B_1x_1 + B_2x_2 + \ldots + B_kx_k + \lambda \quad (4.2)$$

If there is a curvature in the system, the identification is performed using high degree polynomials (4.3).

$$Y=B_0 + \sum_{i=1}^{n} B_i x_i + \sum_{ij}^{n} B_{ij} x_i x_{ij} + \sum_{j=1}^{n} B_{ij} x_j^2 + \lambda \quad (4.3)$$

Here, B_0 refers to the independent term of the regression equation, B_i the linear term, B_{ii} the second order term, B_{ij} refers to the inner interaction term, and λ is the error of observation or noise. Y shows the response for the given levels of the independent variables. In this experimental design method, the dimensionless coordinate system is studied, and independent variables are expressed as follows (4.4-4.5);

$$x_i = \frac{(X-X_i^*)}{\Delta x_i} \quad (4.4)$$

$$X_i^* = \frac{(Xi_1-Xi_{-1})}{2} \quad (4.5)$$

In the dimensionless coordinate system, the highest level is indicated by +1, the lowest level by -1, and the center point is indicated by 0. The number of experiments in the design is determined by equations (4.6) and (4.7).

$$N=2^k + 2k + n_0 \qquad k < 5 \quad (4.6)$$

$$N=2^{k-1} + 2^k + n_0 \qquad k \geq 5 \quad (4.7)$$

In these equations below, N indicates the number of experiments, n_0 shows the number of experiments at the central point, and there is no limit on the number.

In experimental planning, generally used one is central component design. Component designs are first order factorial designs with an increased number of points to determine the coefficients of the second order axes. In general, the central component design (with each variable coded as -1, + 1) with an increased number of points is applied. α; it is the axial point of the design, which expresses the distance from the center point and whose value is defined by the researcher using various criteria. Often the researcher performs multiple examinations at the center point for specific design features. In these experiments, the α value on the second order axis is calculated according to the following equations (4.8-4.9).

$$\alpha = 2^{k/4} \qquad k<5 \qquad (4.8)$$

$$\alpha = 2^{(k-1)/4} \qquad k\geq 5 \qquad (4.9)$$

Taylor series given in equation (4.10) is used to determine the model coefficients.

$$B_i = \frac{\partial f}{\partial x_i}_{xi=0;}\ B_{ij} = \frac{\partial^2 f}{\partial x_i\, x_j}_{x=0;}\ B_{ii} = \frac{\partial^2 f}{\partial x_i^2}_{x=0} \qquad (4.10)$$

The least squares method is used to find the coefficients of equality. The difference between the observed function values according to the least squares method and the calculated function value should be minimum.

The model used in this experimental design method was statistically evaluated by the ANOVA (Analysis of Variance) test (Table 4.1). Here the SSM represents the sum of squares of the model, SSE represents the sum of squares of the error, SST represent the sum of squares of the model and the error, MSM represents the ratio of the squares of model (SSM/f_3), MSE represents the ratio of the squares of error (SSE/f_2). After calculating the F value, the FP (f_2, f_3) value given from the Biometrika tables for the determined magnitude level and for the degrees of freedom f_1, f_2 are read and compared. If the calculated F value is greater than the value read from the table, it can be accepted that the regression model used expresses the system mathematically.

Table 4.1 Statistical evaluation of the model used with ANOVA test

	Degrees of freedom	**Sum of squares**	**Ratio of squares**	**F**
Model	f_3	$\Sigma (\bar{y}_i - \bar{y})^2$	SSM/ f_3	MSM/MSE
Error	f_2	$\Sigma (yi - \bar{y}i)^2$	SSM/ f_2	
Sum	f_1	$\Sigma (yi - \bar{y})^2$	SSM/ f_1	

5
ISOLATION OF MEGAKARYOCYTES

MKs, whose behaviors in microchip channels will be examined, will be isolated from mice. For this purpose, EasySep ™ Mouse PE Positive Selection Kit (STEMCELL) (Figure 5.1) was used, and an appropriate procedure wasapplied.



Figure 5.1 Isolation magnet and selection kit

Isolation experiments were carried out at Yeditepe University Regenerative Biology Laboratory. Mice were obtained from the Experimental Research Center of Yeditepe University Medical School. Mice for isolation of MKs are shown in Figure 5.2.

Properties of mice are shown in Table 5.1

Table 5.1 Properties of mice

Ancestry	Gender	Age
C57BL/6	♀	8-16 week

For PLT production from MK in a microchannel, the MK isolation procedure was determined and listed as below.



Figure 5.2 Mice for isolation of MKs

1. Mononuclear Cell Separation

a. Sample is reconstituted with PBS in 1: 1 ratio.

b. The patient stem cell is diluted with PBS at a ratio of 1:5.

c. The mononuclear cells were separated according to gradient difference in cells with histopaq at a ratio of 1: 2.

d. Centrifuge at 3000 rpm for 15 min, stop-start slow for 30 min. (put samples + adjust + stop-start slow button).

e. Add 3 x PBS to the MNHs collected on the 15-falcon and centrifuge at 1500 rpm for 5 min.

f. The supernatant can be spilled and washed again.

g. Add 3 ml of PBS and dissolve the pellet. (Counting for 3ml)

h. If Cytell Quick Count / Viability Reagent is used to count cells;
25 μl of sample + 0.5 Cytell (reagent) dye is added to the small vial and the light of hood is kept in the dark for 5 minutes. The thoma lamel is taken and the sample is inserted into the cavity. The Cytell device is switched on and the sample is placed. Quick Count is selected from the main screen. Adjustment and focus are made. The cell read at 3 ml is counted.

i. There are 3 ml x 10.000 (volume slide volume) x cell number (2 squared mean averages) if counting in the slide.

Easy Sep Human FITC Positive Selection Kit

Cells are centrifuged at 1500 rpm for 15 min. Supernatant is poured and dissolved in the prepared buffer (Recommended Medium).

Buffer Preparation (Recommended Medium);

Prepare 49 ml PBS with +1 ml FBS +100 μl EDTA and stand in ice.

(PBS + 2% FBS and 1mM EDTA)

Calculation of cell concentration;

Add 0.1-2.5 ml buffer if $1*10^8$ cells

If there is less than $1*10^7$ cells, it is resuspended with 0.1 ml.

* From each cell to small vials, three 200 μl will be allocated as UNS (Unstaining). Separated for both flow and culture. Separate 2-3 ml for culture.

a. Cells are added to a 5 ml polystyrene round bottom tube. UNC+ CD34+ CD41a (there will be 3 tubes)

b. 100 μl is added to 1 ml of FcR blocker. Mix is made.

c. To the samples 0.3-3 μg / ml is added to the FITC-conjugated antibody. Mix is made (pipetage). Incubate for 15 min at room temperature.

d. Add a total of 10 times buffer and centrifuge for 5 min at 1500 rpm. The top is poured and the pellet is resuspended with the buffer at initial rates (add 0.1-2.5 ml buffer if there are $1*10^8$ cells)

e. For example, 100 μl selection cocktail is added for 1 ml.

f. Incubate for 15 min at room temperature.

g. For 1 ml, 50 μl magnetic particles are added and pipetted up and down 5 times.

h. Incubate for 10 min at room temperature.

i. Add 2.5 ml buffer and pipette 2-3 times.

j. The tubes are placed on a magnet and incubated at room temperature for 5 min.

k. While the tubes are in the magnet, the supernatant is removed by pipetting. Add 2.5 ml of buffer into the tube and wait 5 minutes and discard the supernatant.

l. Cells adhering to the wall with the latest 2,3 ml buffer are dissolved.

m. The cells were filtered through 70 μm.

n. For flow cytometry, 100 μl of cells and 100 PBS are added to each well in 96 wells (two by two per sample).

o. Cell culture is done after flow. Media is prepared for cells.

2. Cell culture

a. Proper media (RPMI + 20% FBS + 1% PEN. STREP +30 ng / ml TPO + CC100) is prepared.

b. The filtered cells were centrifuged at 1500 rpm for 5-10 min. Dissolve in 3 ml media.

c. Add 1 ml media + 1 ml cells to each of the 6 wells. The incubator is removed. After 6 days, the medium is changed. The wells are divided into UNC + CD34 + CD41a + CD42.

3. Media Exchange

a. Change of first medium after 6 days the cells are examined by microscope and cytell. Flow cytometry counting is performed before centrifugation.

b. When the second medium is changed, the cells are taken from the incubator and examined in the microscope and cytell.

c. MKs are non-adherent cells. The washing solution is prepared. If there is contamination into 42 ml DPBS, 500 μl are placed in Pen + Strep. Cells are washed 6-7 times in the lower part and collected in 15 cups. The remaining cells are removed by pouring 2 cc of washing solution into discharged wells and washing 6-7 times. Microscope is examined to see if any cells. Wash if necessary again.

d. Centrifuge at 1500 rpm for 5 min. The supernatant is poured. The medium is prepared.

e. 25 ml (RPMI + 20% FBS) + 250 μl of pen + strep is added to the falcon tube (1%). The TPO is calculated and added to the medium a little more in each passage.

f. The supernatant is discarded from the falcon which is discharged from the centrifuge. The pellet is melted with 1 cc of medium. cells are stained if counted in the flow cytometer. 100 μl of cells +100 μl of PBS +0.2 μl of CD41a and CD34 are added to 96 well. When diluting the antibodies, 1: 1000 dilution is performed.

g. 0.2 μl of antibody (CD34 FITC + CD41a FITC) is added to the wells for a total of 200 μl.

h. 1cc cell +1 cc medium is added to wells. If contamination is present, 500 μl s of DPBS + Pen + Step was added to the middle of wells 6 of the wash water.

i. Sterilize with alcohol and remove the incubator.

j. The mouth is alcoholed at the outlet and in the inlet from the incubator.

4. Cytell cell look

a. Cytell opens. From the home screen, select Digital Image. Open the lid with automatic touch and place the cell flask.

b. For 6 wells, 6 costar or 12 costar or Bd for 12 wells.

c. 5 pieces filter camera view. Bright color is selected on the right side. This allows the normal microscope image. Other color filters read BLUE –DAPI, GREEN –FITC.

d. Focus is set. If it is read well, it is selected and the red arrow on the screen is displayed. The selection is made from different areas and the focus is adjusted and clarity is achieved.

e. When the ruler mark is pressed in the upper right corner, the cell size is measured with the ruler. The given 1-unit measure is divided by how many intervals and the cell size is measured.

f. To save the image: If the image is fine, click on the nested frame at the top right. The file is named.

6
RESULTS AND DISCUSSION

6.1 Megakaryocyte Isolation

With the single-channel microchip, the images of MK differentiation from blood samples for Day 1, Day 6 and Day 10 can be seen in Figure 6.1-6.3, respectively.

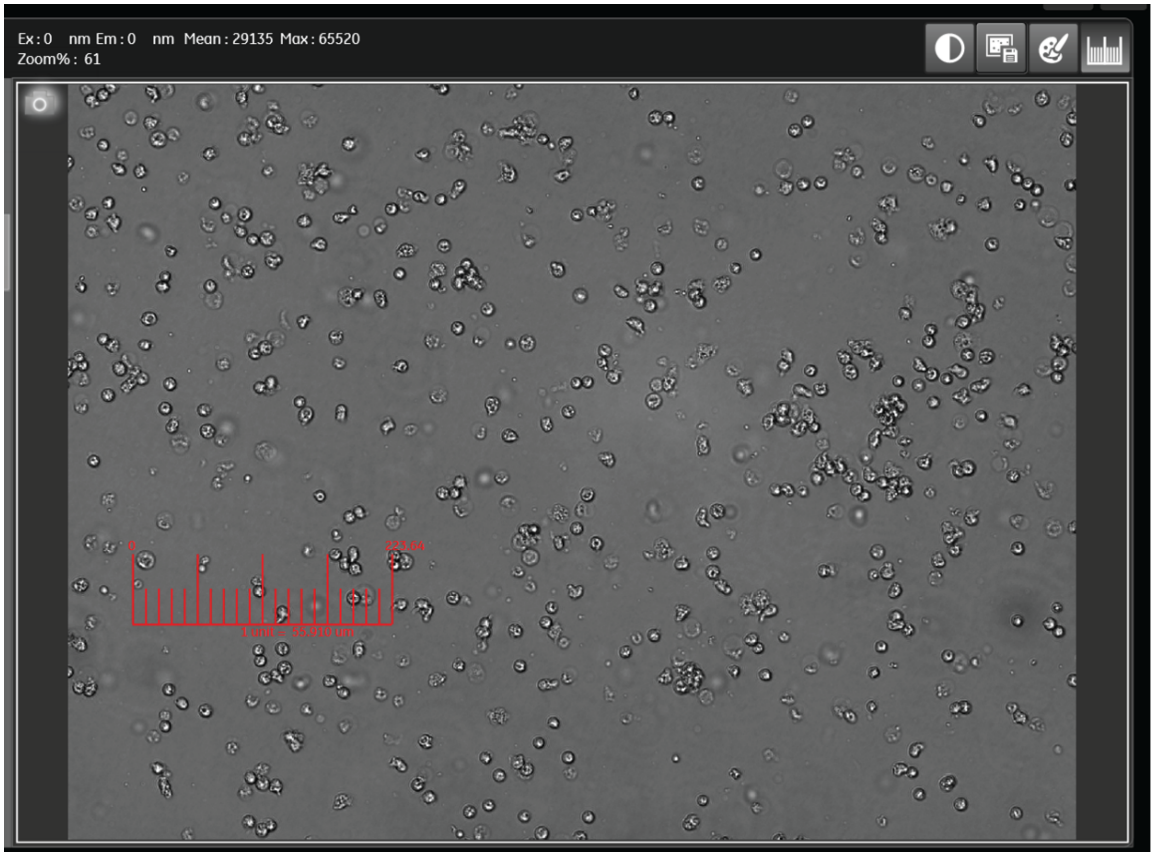


Figure 6.1 Images of MKs (Day 1)

MKs cultured 12 days and final sizes were nearly 45 μm. In this part, there were no clogging and imaging problems for the microchannel. The characteristic structure (granular) that MKs have could be seen under the microscope while fluid flow.

On the first day, MK's size is nearly 11 μm. At the end of the sixth day, it is seen that MKs become differentiated, and their sizes are around 22 μm.

On the 10^{th} day, MKs are continued to differentiate, and their sizes nearly 32 μm. After the 10^{th} day, contamination was observed and so that no more MK differentiation occurred after these days. If there were no contamination, the sizes of MKs would be around 50 μm.

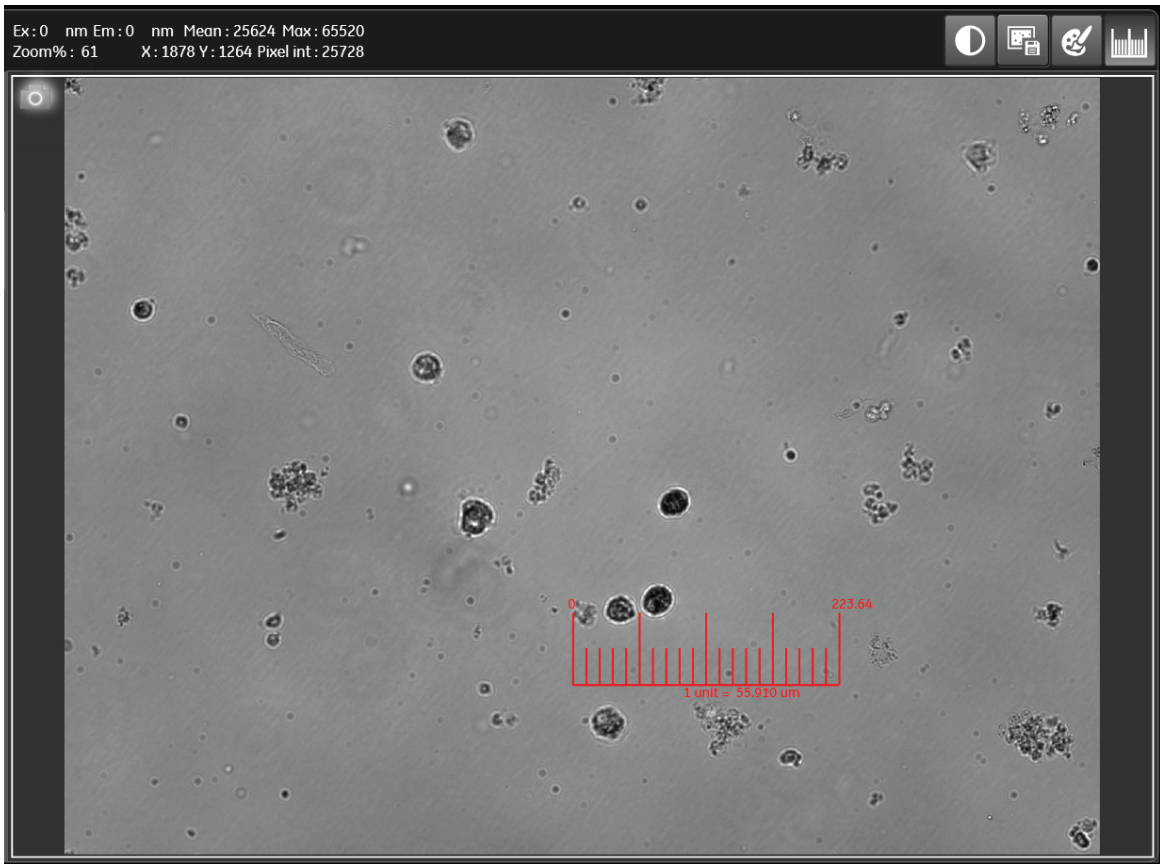


Figure 6.2 Images of MKs (Day 6)

6.2 Determination of Relation Between Flow Rate and Shear Rate and Shear Stress

A computational study was performed to determine the shear stress and shear rate by the finite element method, which is the first step of the thesis. A microchannel design shown in Figure 3.1 was developed. Analysis of the flow was performed by the COMSOL Multiphysics software package. The effects of flow rates and pillar sizes on the shear stress were investigated. Thus, we estimated the convenient flow rate regime.

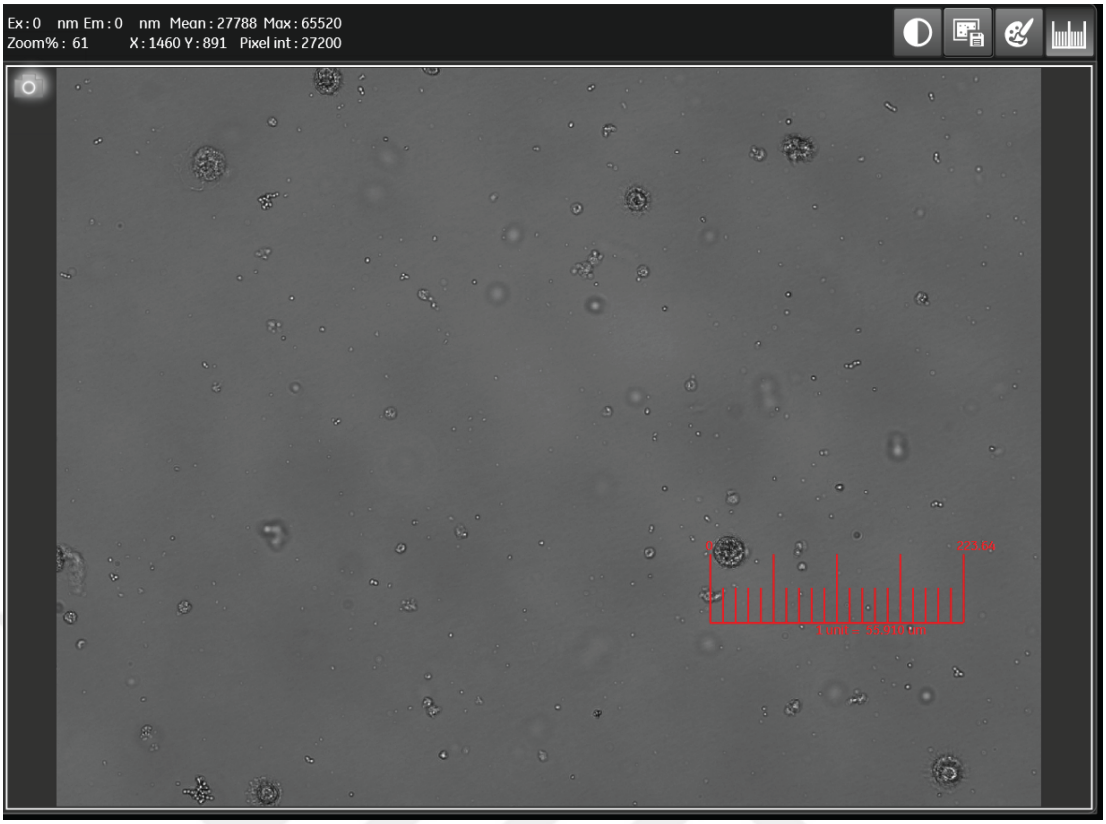


Figure 6.3 Images of MKs (Day 10)

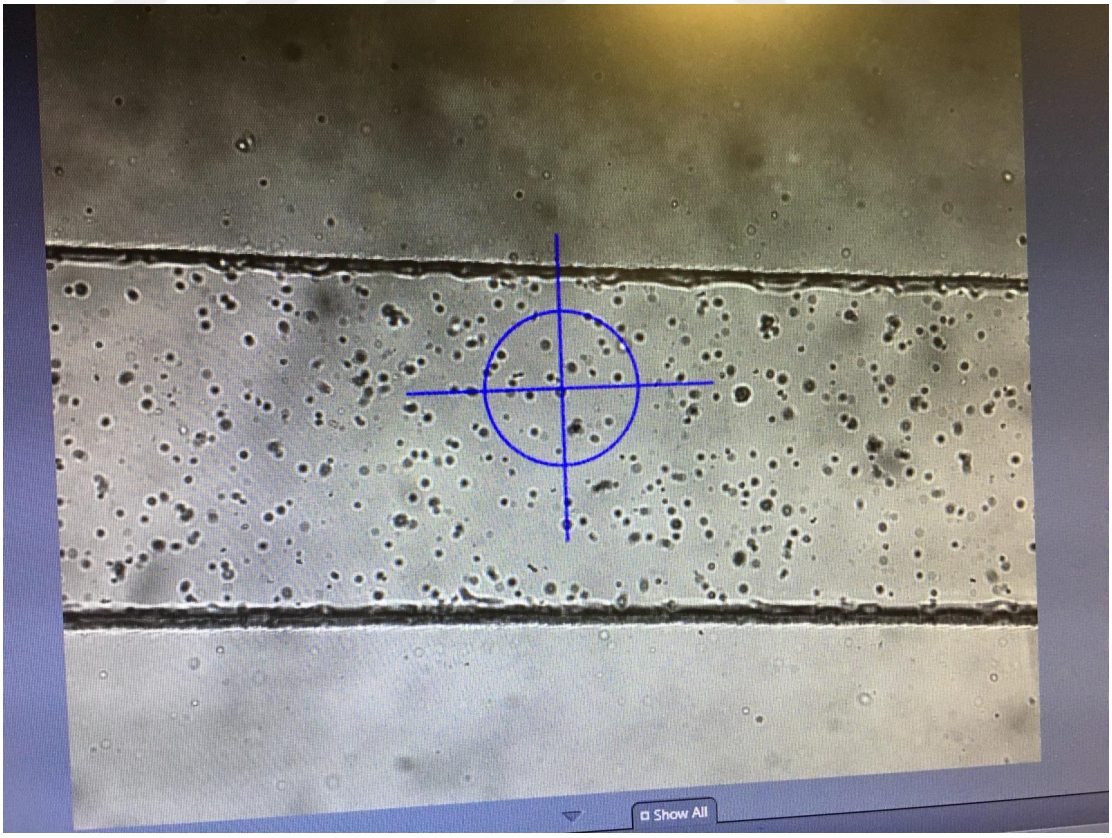


Figure 6.4 Microchip trial (MKs in the microchannel)

6.2.1 Flow Simulation

Different velocity values were tried for observed how flow, shear stress, and shear rate were affected by velocity variances. Also, particle tracking was applied to investigate the flow motion and particle distribution in a flow. Finally, streamlines were demonstrated to understand the flow aerodynamic (Appendix).

6.2.2 Relationship Between Flow and Shear Stress/Shear Rate

In literature, the flow limits are generally expressed in terms of maximum shear rate or shear stress instead of velocity or volumetric flow since the deterioration of the MKs occurs when a specific stress limit is reached, regardless of the geometry.

Table 6.1 Maximum shear stress and shear rate values for different velocities

Velocity (μm/s)	Max. Shear Stress (Pa)	Max. Shear Rate (1/s)
3000	0.98	998
3333	1.10	1108
3667	1.20	1220
4000	1.31	1331
4333	1.42	1443
4667	1.53	1554
5000	1.64	1665
5333	1.75	1776
5667	1.86	1887
6000	1.97	1999

In this step of thesis, we understood the relation between the velocity and the shear rate and the velocity and the shear stress. From the results of our simulations given in 3.2, Table 6.1 can be obtained. Since the literature suggested not to work above the shear rates 2000 1/s, we designed our simulations to result shear rates

between 1000 – 2000 1/s. Note that the negativity of shear stress from our results only dictates the direction of the pressure.

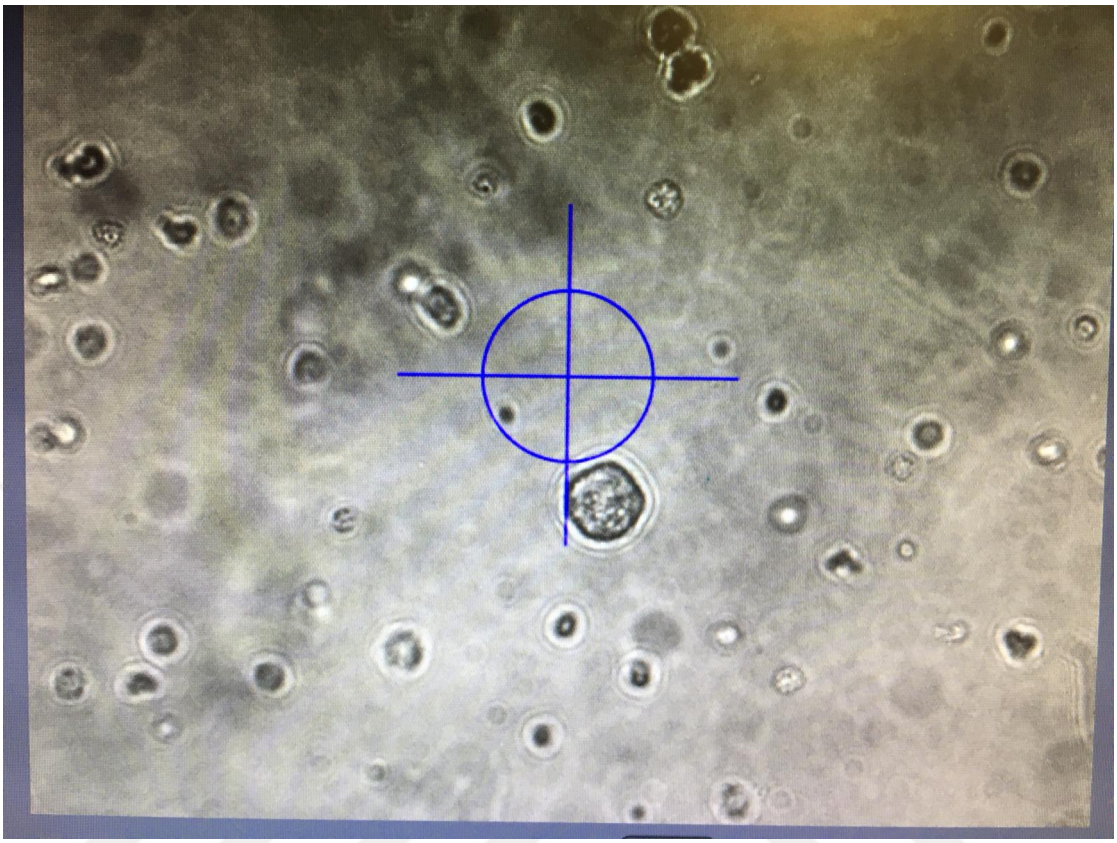


Figure 6.5 Microchip trial (size of MK inside chip: ~45 μm)

These results indicate a linear relation between velocity-shear stress and velocity-shear rate, as expected since water is a Newtonian fluid. The results are given in the Figure 6.6 and Figure 6.7.

In addition, using tracing mode, we worked on how the different size of MKs interacts with the pillars and passes through in the channel (Figure 6.8). Different MK sizes (20 μm, 40 μm, 60 μm, 80 μm) were tried for the flow, and particle trajectories were observed again without causing a flow related problem. As you see in Figure 6.8, red dots represent the MKs, and when the size of MKs increases, the flow rate of the MKs is reduced. This result can be easily observed from the position of the red dots, and it is an expected fact.

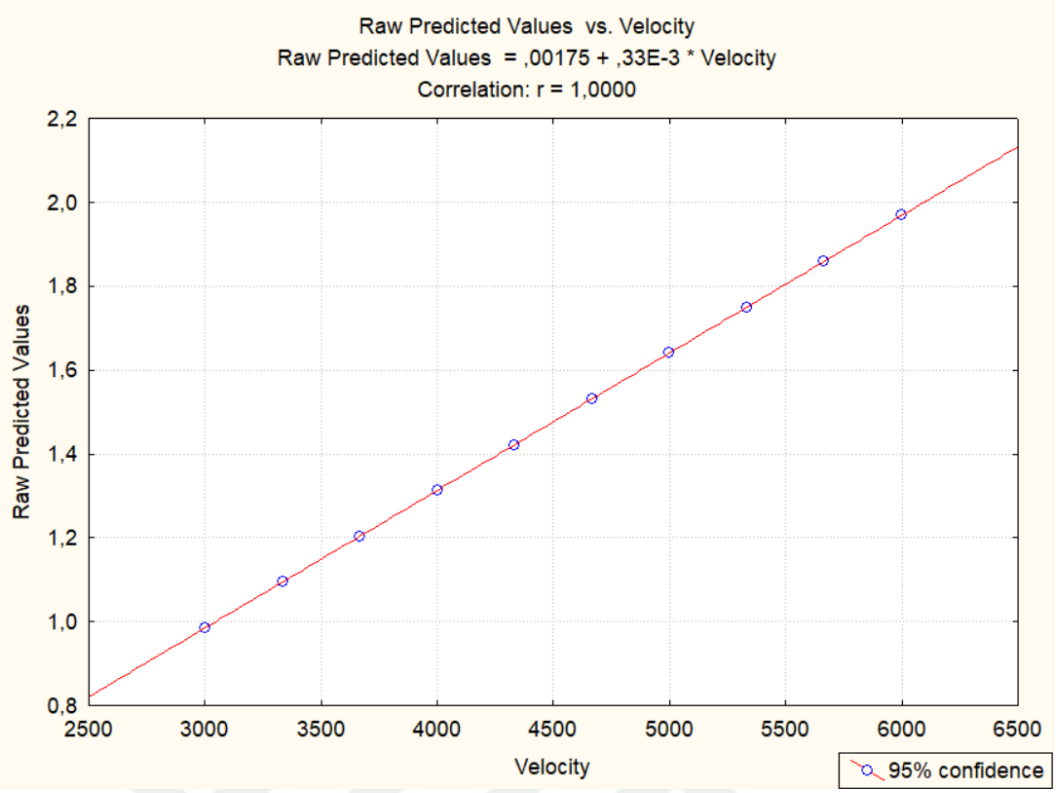


Figure 6.6 The relation between Velocity (µm/s) and Shear Stress (Pa)

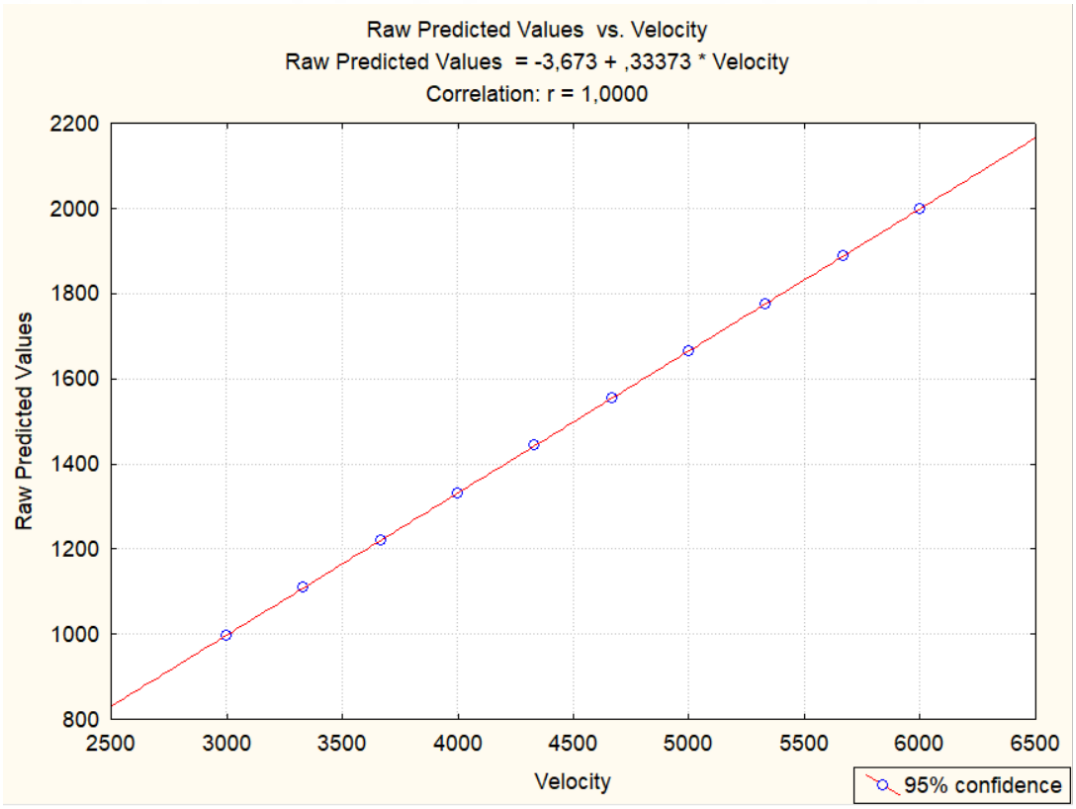


Figure 6.7 The relation between velocity (µm/s) and shear rate (1/s)

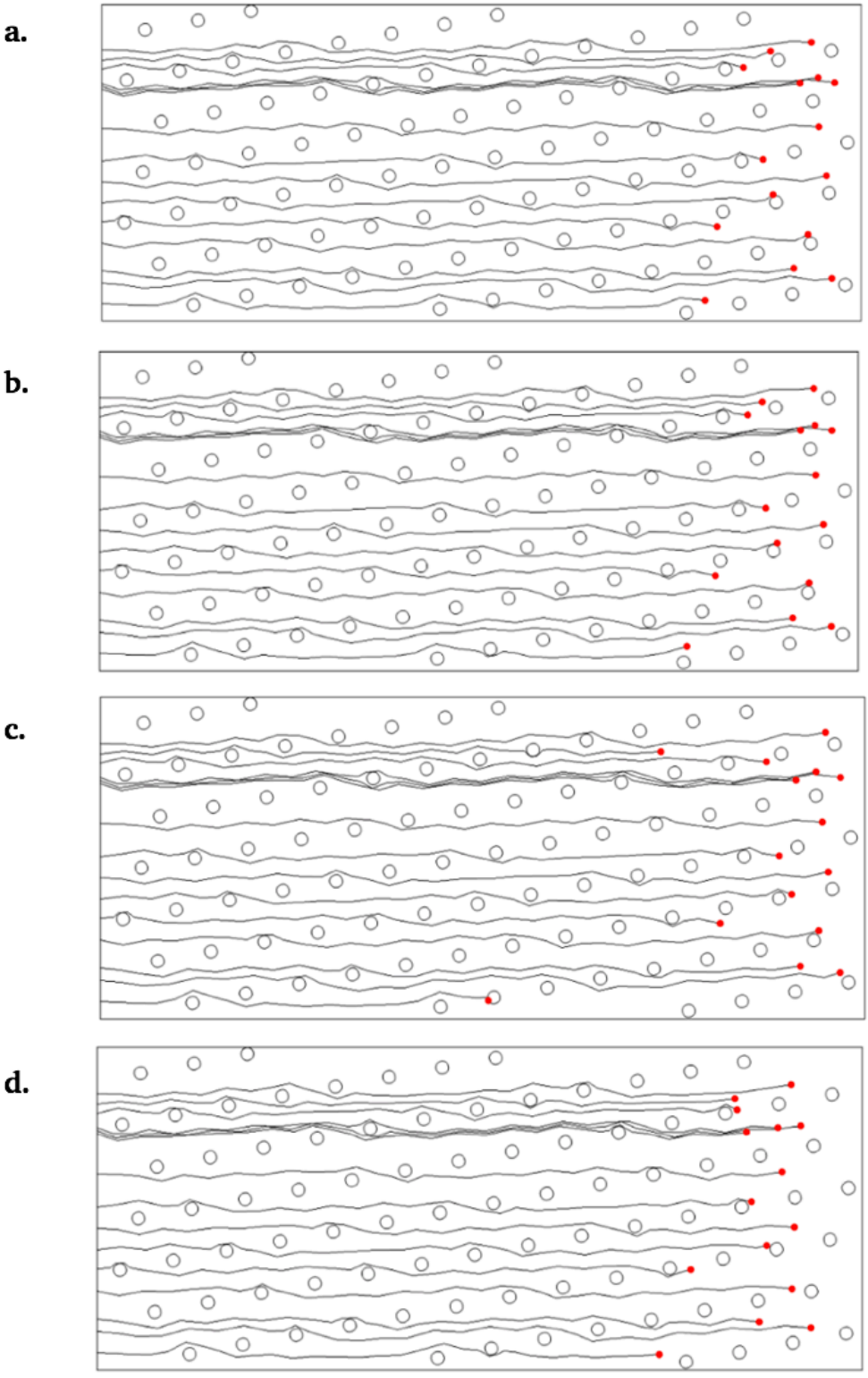


Figure 6.8 The particle trajectories at flow velocity 6000 μm/s and particle diameters of 20 μm (a), 40 μm (b), 60 μm (c), 80 μm (d)

6.3 Microfluidic Chip Design

The microfluidic chip designed in this context, whose flow simulation and mathematical modeling work has been carried out, is shown in Figure 3.2. The chip has three input channels; these are a central pressure channel (Q_1), a channel containing MKs (Q_2), and the main channel (Q_3) that creates the shear stress necessary for the MKs to elongate. For PLT formation from MKs, three different bioreactor flows with 30, 60, and 90-degree angles (α) between pressure channels, respectively, were designed and simulated. There are slits in the center of the channel throughout the entire channel, and the MKs will become PLTs as they pass through the slits. The slits are 10 μm wide and 90 μm long, with 20 μm intervals. The upper channel is responsible for confining the MKs to pass through the slits by applying pressure. The lower channel is responsible for the elongation of the MKs with the help of shear velocity. w_1 and w_2 are the heights of the currents Q_1 and Q_2 in the microfluidic channel.

6.3.1 COMSOL Multiphysics application

Computational fluid dynamics was used in the study to simulate and predict flow rates in a microchannel system using COMSOL Multiphysics. Computational fluid dynamics (CFD) is an approach that helps solve the limitations and problems associated with fluid flow. Numerical methods are used for the solution. The Navier-Stokes equations are the basis of CFD because they contain expressions for the conservation of mass, momentum, and energy. CFD has an essential role in the optimization of the biotechnological process. Thanks to CFD, we can develop and optimize the production of biotech products. COMSOL Multiphysics is a powerful interactive environment for modeling and solving all kinds of scientific and engineering problems based on partial differential equations (PDE). In COMSOL simulations, we aimed to determine velocity profiles and flow lines, to determine Q_1, Q_2 and Q_3 flow velocities to observe better dynamic behavior and to investigate the relationship between flow dynamics and the angle between main and pressure channels (Figure 6.9-6.10).

First, the effect of the angle between the main and pressure flows on the PLT production efficiency was investigated (Figure 6.9). As can be seen, bioreactors

with angles of 30, 60 and 90-degrees, respectively, were investigated at a constant flow rate. Colored dots represent MKs, and colored lines represent flow lines of Q_1, Q_2, and Q_3. Different colors indicate points at different speeds. When the red colored dot moves at maximum speed, the blue colored dot is at minimum speed.

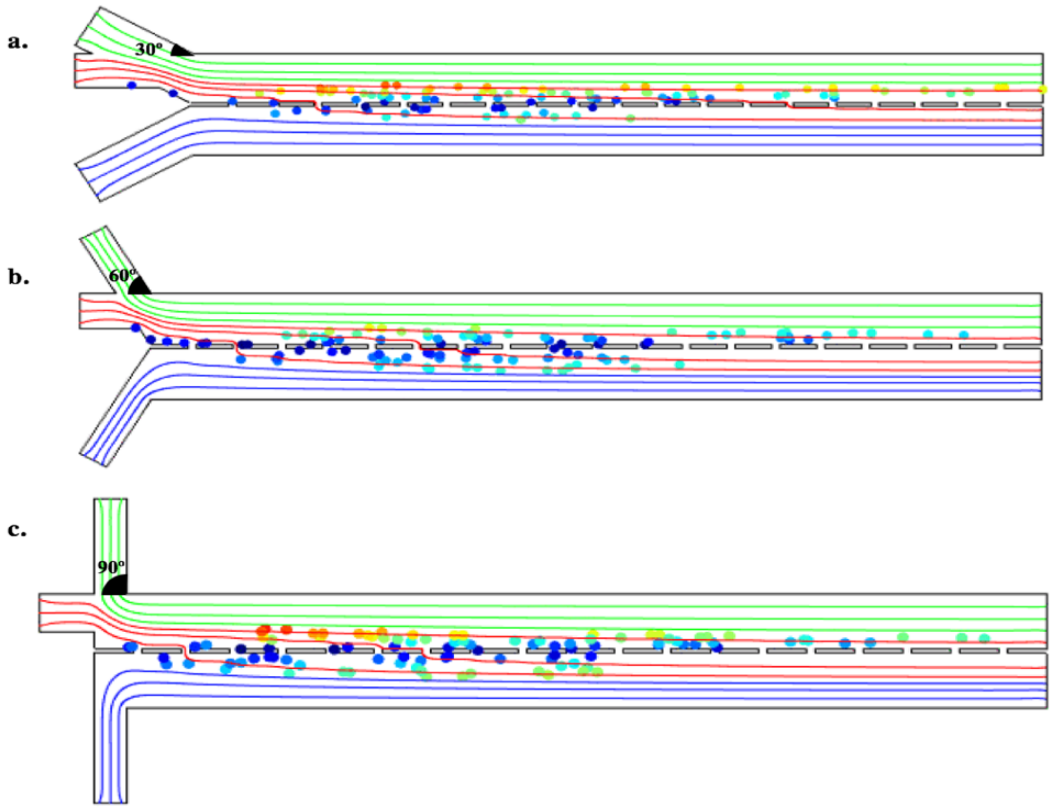


Figure 6.9 Effect of an angle between pressure channels at Q_1=10 μL/min, Q_2=5 μL/min, Q_3=5 μL/min. a: α=30°, b: α=60°, c: α=90°.

When the angle is 60 degrees, it is seen that more MK is trapped and passes through the slits. When the angle is 30 degrees, the overhead pressure flow is not very effective, causing some MKs to be unable to be trapped in the slits. On the other hand, for the 90-degree design, the pressure flow pushes most of the MKs through the first slits. This causes the MKs in that region to lose the distribution homogeneity along the slits, and agglomeration is observed. Homogeneous distribution is critical as elongation is not a rapid process when a MK is trapped.

Secondly, we investigated the effect of flow rates at 60-degree angle with different flow rates (Figure 6.10). When the ratio Q_3/Q_2 is higher than Q_1/Q_2, the pressure created by the upstream and downstream flows is very close to each other. MKs

follow upstream flow lines and cannot pass through slits. Conversely, when the Q_1/Q_2 ratio increases and Q_3/Q_2 decreases, more MK diffuses between the slits.

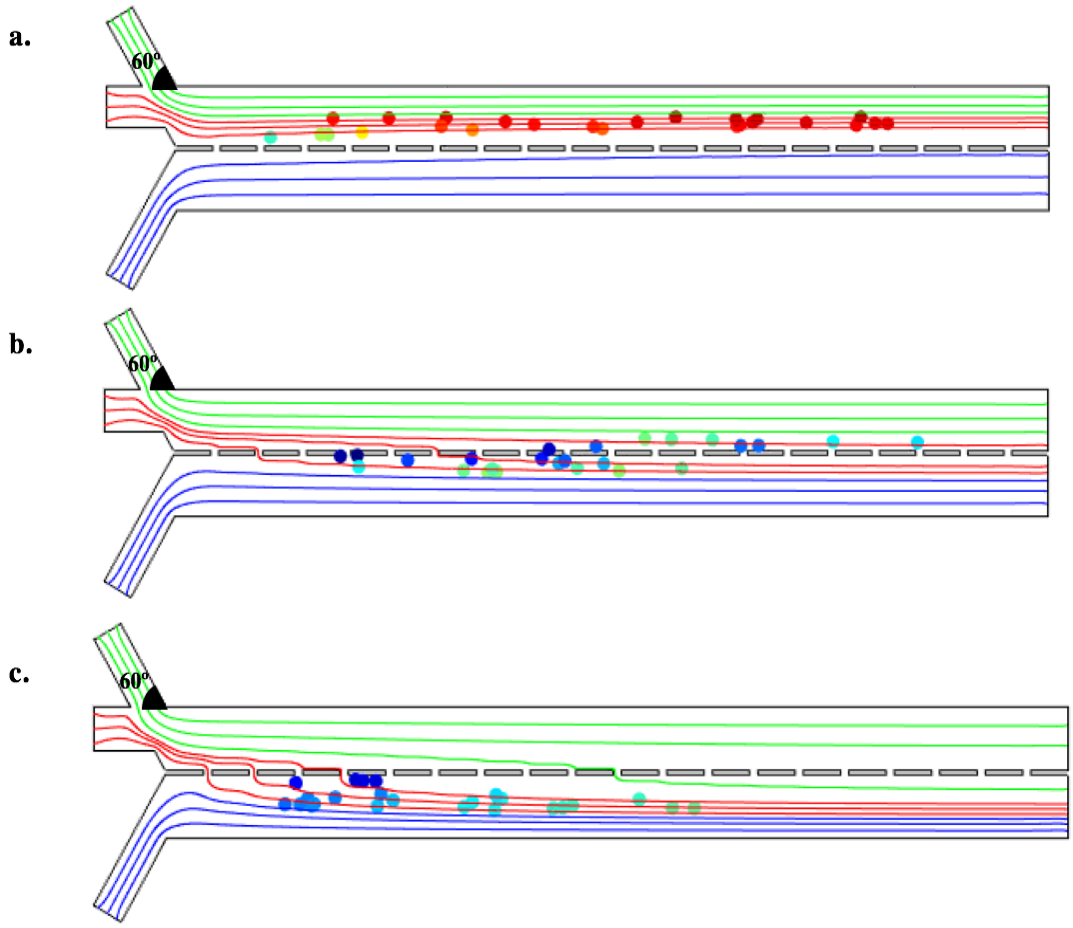


Figure 6.10 Effect of flow rate ratios between main and pressure channels at α=60°, Q_2=5 μL/min. a: Q_1/Q_2=2, Q_3/Q_2=5, b: Q_1/Q_2=4, Q_3/Q_2=3, c: Q_1/Q_2=6, Q_3/Q_2=1

6.4 COMSOL Modeling

In our design, we mimicked the bone marrow geometry for the trapping of MKs. We first investigated the appropriate flow rates that create a convenient shear rate for MKs elongation by CFD. When the Q_2 was set to 5 μL/min, the flow rate and the shear rate profiles were achieved as in Figures 6.11A and 6.11B, respectively. The flow rate and shear rate profiles are similar throughout the micro-bioreactor.

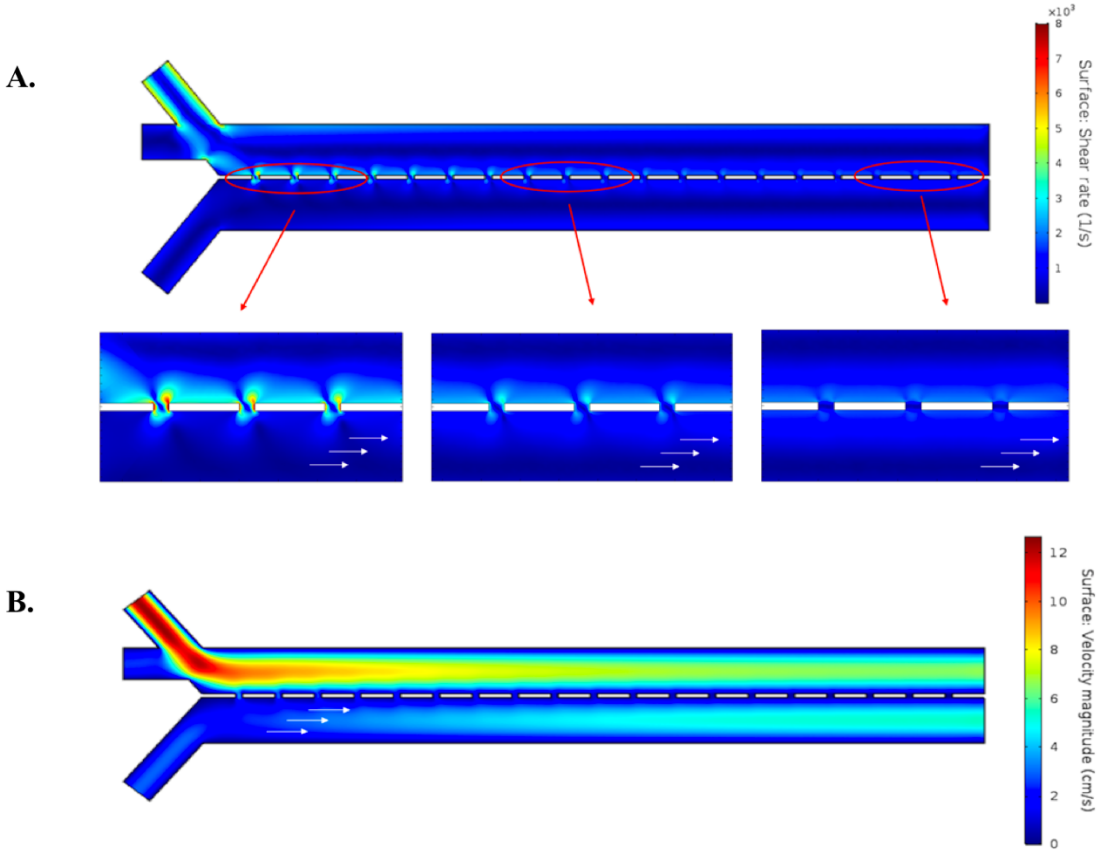


Figure 6.11 A: Shear rate distribution along the length of the microchip at Q_2=5 μL/min. (Q_1=24 μL/min and Q_3=6 μL/min) **B:** Flow rate distribution along the length of the microchip at Q_2=5 μL/min. (Q_1=24 μL/min and Q_3=6 μL/min)

Contrary to what Thon et al. [6] and Martinez et al. [11] mentioned, in our design, as it moves along the flow direction into the micro-bioreactor, the shear rate values acting around the slits decrease. The maximum shear rate is 6000 1/s at the first slit while counting all slits; the average shear rate is 3500 1/s. The literature makes it possible to find different shear rate values for PLT formation in bioreactors. Even though the shear rate ranges differ from 50 to 6000 1/s in experimental studies, the generally mentioned value range is above 1000 1/s [2][5][6][10][11][28]. Therefore, to decide the flow rates and predict the shear rates around the slits for the implementation of optimum shear rate ranges for PLT production in our system, we examined flow rates from 1 to 9 μL/min. According to our analyses, the applicable flow rate range is determined as 3 to 8

μL/min by considering shear rate values and 2 to 5 μL/min by considering maximum shear rate values (Figure 6.12). The shear rate values required for PLT production in the literature are consistent with the shear rate values we calculated for our design.

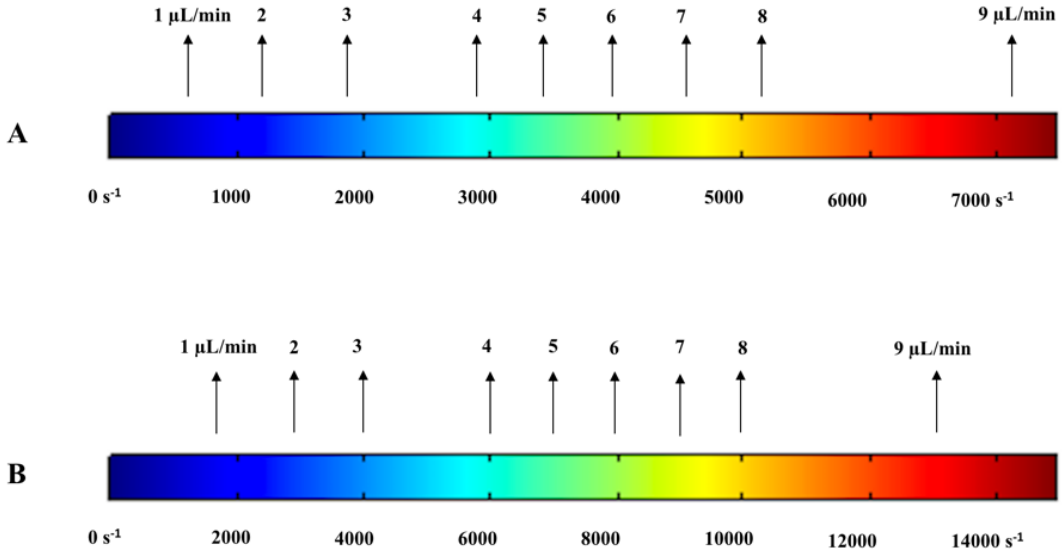


Figure 6.12 A: Average **B:** Maximum shear rate ranges at different flow rates

In the literature, only a few studies have a bioreactor design with more than one inlet channel. Thon et al. [6] have developed a biomimetic microfluidic PLT bioreactor that recapitulates bone marrow and blood vessel microenvironments. They reported that their design decreased the PLT release time from 18 hours to 2 hours and increased more than double the PLT yield. The design of the microfluidic bioreactor has two inlet channels and separated columns spaced 2 μm apart at the center of the bioreactor.

Nakagawa et al. [5] designed a new bioreactor with two flows in the concurrent direction. They reported that designing an angle of 60 degrees between the main and pressure flows promotes PLT generation compared to an angle of 90 degrees. The number of PLTs production increased by 3.6 times, bringing down the angle from 90 to 60 degrees. The increase, however, is not explained very well as if it is related to variation in the shear stress or the number of MKs trapped by the slits. Therefore, in this work, we modeled and simulated the flow dynamics in the microfluidic platform.

6.4.1 Response surface methodology

RSM is a combination of mathematical and statistical techniques in which various variables influence the response variable. Therefore, RSM was used before simulations to optimize the trapping of MKs with different geometries and operating conditions. With the help of RSM, mathematical models obtained by statistical techniques (linear, square polynomial functions and others) and with the help of designed experiments can be verified. A linear function is the simplest model that can be used for RSM.

If the answers fit Equation 6.1, the linear model can be applied.

$$Y = \beta_0 + \sum_{i=1}^{n} \beta_i x_i + \lambda \quad (6.1)$$

Here, n is the number of variables, β_0 represents the constant term, β_i represent the coefficients of the linear parameters, x_i represent the variables and λ is an error. The range and levels of the independent variables and the numerical values of the quantities are shown in Table 6.2.

Table 6.2 Range and levels of independent variables for simulation studies

Independent variables	Range and levels		
	-1	**0**	**+1**
Angle (˚), X_1	30	60	90
Q_1/Q_2, X_2	2	4	6
Q_3/Q_2, X_3	1	3	5

Angle, Q_1/Q_2 and Q_3/Q_2 were chosen as independent variables, and the response variable was determined as the percentage of trapped particles. 'Design Expert' software (Version 6.01, Stat-Ease, Inc., Minneapolis, USA) was used for the regression and graphical analysis of the obtained data. The statistical significance of the linear model was determined by analysis of variance (ANOVA). The effect of each parameter was evaluated by F-value and p-value. The R^2 value defines the property of fit of the linear model.

In this study, optimum operating conditions and flow dynamics for PLT formation from MKs in microchannels were determined with the combination of COMSOL Multiphysics and RSM. Accordingly, PLT production efficiency is significantly affected by the angle between the main and pressure flows and the ratio of these flow rates.

The results obtained from the RSM experiments carried out under the determined operating conditions are given in Table 6.3. The linear model equation is given in Equation (6.2). Where Y is the percentage of trapped MKs.

$$Y = 30.96 + 0.25\,X_1 + 16\,X_2 - 17.75\,X_3 \qquad (6.2)$$

In Table 6.4, the model F-value of 17.97 implies the model is significant. There is only a 0.01% chance that a "Model F-Value" this large could occur due to noise. Values of Prob>F less than 0.05 indicate model terms are significant. In this case, X_2 (0.0003) and X_3 (0.0001) are significant model terms. For the model, Prob> F (<0.0001) less than 0.05 indicates that the model represents the system well. Adeq Precision measures the signal to noise ratio.

A ratio greater than 4 is desirable. For the model, the ratio of 14.93 indicates an adequate signal. This model can be used to navigate the design space. These results indicate that Q_1/Q_2 and Q_3/Q_2 directly affect the percentage of trapped MK. Response surface method contour plots (Fig. 6.13-6.15) are plotted to estimate the effects of independent variables on the percentage of trapped MKs. Each contour curve represents an infinite number of combinations of two test variables; the other two are kept at zero levels.

The percentage of MK trapping increases with increasing Q_1/Q_2 ratio and angle (Figure 6.13-6.14). On the other hand, the percentage of MK trapping decreases with the increase in the Q_3/Q_2 ratio (Figure 6.14). This is thought to be due to the negative pressure effect. In our design, Q_2 is pressed from the top with the effect of Q_1, and MKs pass through the slits.

Table 6.3 The actual values of simulation conditions and response variable

#	Angle (˚)	Q_1/Q_2	Q_3/Q_2	Trapped MK (%)
1	60	4	3	72
2	30	6	3	56
3	90	2	3	8
4	60	4	3	68
5	90	6	3	100
6	60	2	5	0
7	60	4	3	72
8	60	4	3	72
9	30	4	5	0
10	60	4	3	72
11	90	4	1	100
12	30	4	1	100
13	30	2	3	0
14	60	2	1	64
15	60	6	5	72
16	90	4	5	8
17	60	6	1	100

Thanks to Q_3, the pressed and trapped MKs are elongated in the flow direction. So, if the ratio of Q_3 is increased, it will cause a negative effect on the process. MKs are pushed upwards before reaching the slits. This means that the MKs are directed in the opposite direction.

Table 6.4 ANOVA for response surface linear model

Source	Sum of Squares	df	Mean Square	F-Value	p-value Prob > F
Model	18724	3	6241.33	17.97	< 0.0001
X_1	450	1	450	1.30	0.2756
X_2	8192	1	8192	23.58	0.0003
X_3	10082	1	10082	29.03	0.0001
Residual	4515.53	13	347.35		
Lack of Fit	4502.73	9	500.30	156.34	< 0.0001
Pure Error	12.8	4	3.2		
Cor Total	23239.53	16			

R^2=0.81

Adeq Precision=14.93

The optimum conditions obtained by RSM with the Design Expert (6.01) program to maximize the percentage of trapped MK are given in Table 6.5. With these optimum values, the percent of trapped MK was obtained at 100. In order to verify these results, a simulation study was carried out it these conditions, and the percent of trapped MKs was obtained at 100. The relative deviation between the computer solution and the experimental results was calculated as <1%. In Figure 6.16, MKs locations can be seen clearly that at different times in a microchannel at the optimum values of angle, Q_1, Q_2, and Q_3 in COMSOL simulation. The whole MKs pass through the slits at the end of the process.

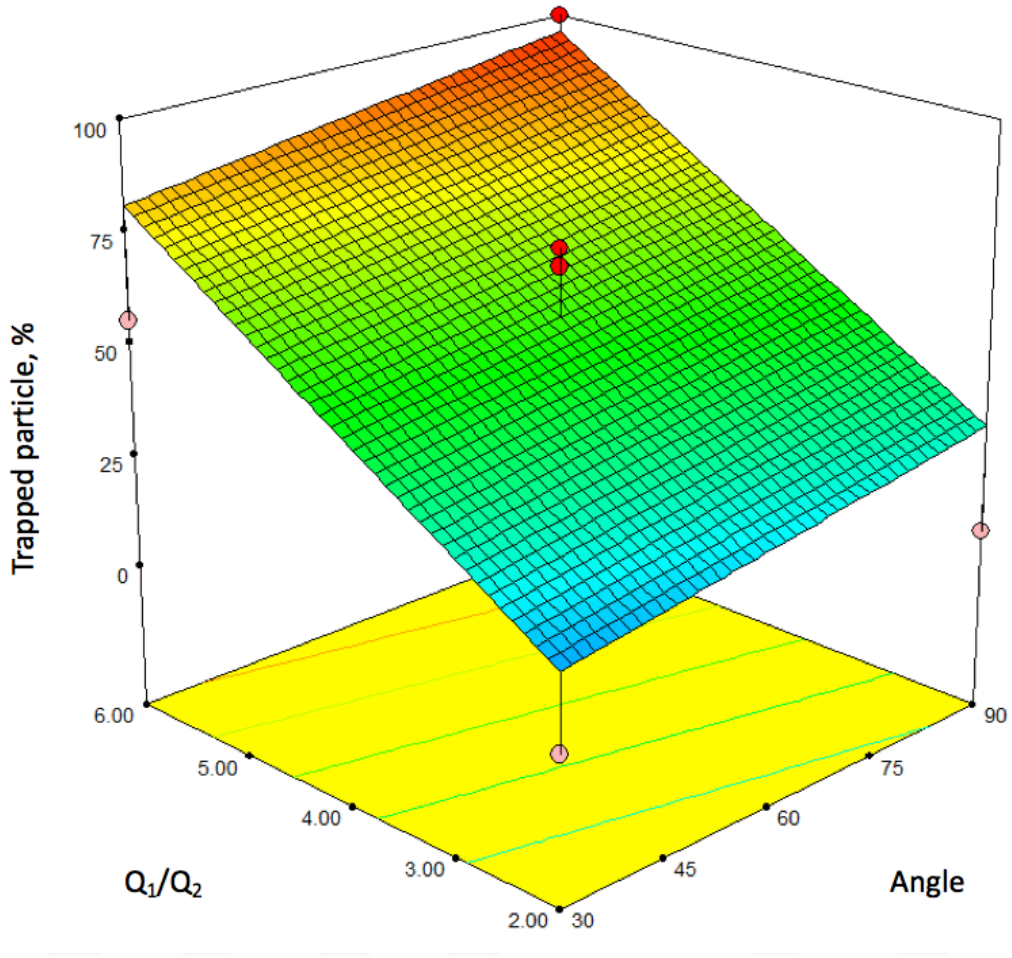


Figure 6.13 Contour-plot of percent of trapped particles: The effect of Q_1/Q_2 and angle. Other variable is held at zero level. Q_1=25 μm/min.

Only a few studies have a bioreactor design with more than one inlet channel in the literature. Nakagawa et al. [5] designed a new bioreactor. They reported two flows in different directions in which the angle between the main and pressure flows are 60 degrees rather than 90 degrees is optimal. They observed that between the directions of flow is 60 degrees lead to pressure and shear stress applied to MKs to promote PLT generation. According to their research, with the help of a new bioreactor design with two flows with a 60 degrees angle between the main and pressure flows, the number of PLTs production increased by 3.6 times. Thon et al. [6] have developed a biomimetic microfluidic PLT bioreactor that recapitulates bone marrow and blood vessel microenvironments. They reported that their design decreased the PLT release time from 18 hours to 2 hours and increased more than double the PLT yield. The microfluidic bioreactor design

has 2 inlet channel and separated columns spaced 2 μm apart at the center of bioreactor.

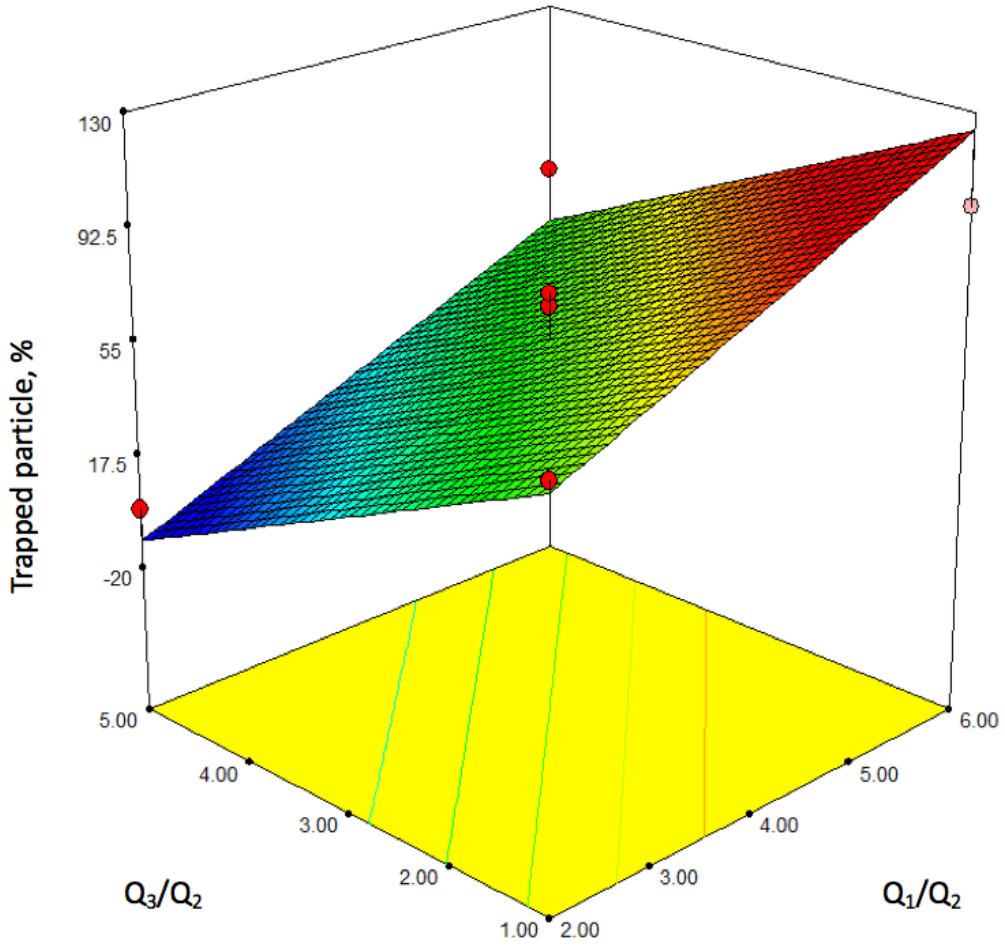


Figure 6.14 Contour-plot of percent of trapped particles: The effect of Q_3/Q_2 and Q_1/Q_2. Other variable is held at zero level. Q_1=25 μm/min.

The PLT production process from MKs can separate 2 stages; the first is trapping the MKs, the second is the elongation of proPLTs. In this study, we only focused on the first step of the process. We aimed to trap more MKs with the help of flow pressure. So, we were not interest in limitations like clogging, adhesion, etc. Because these are the second stage challenges. When the RSM results investigate carefully, we can clearly say that the ratio of bottom pressure flow to main flow has more effect than the angle between the flow directions on the percent of trapped MKs.

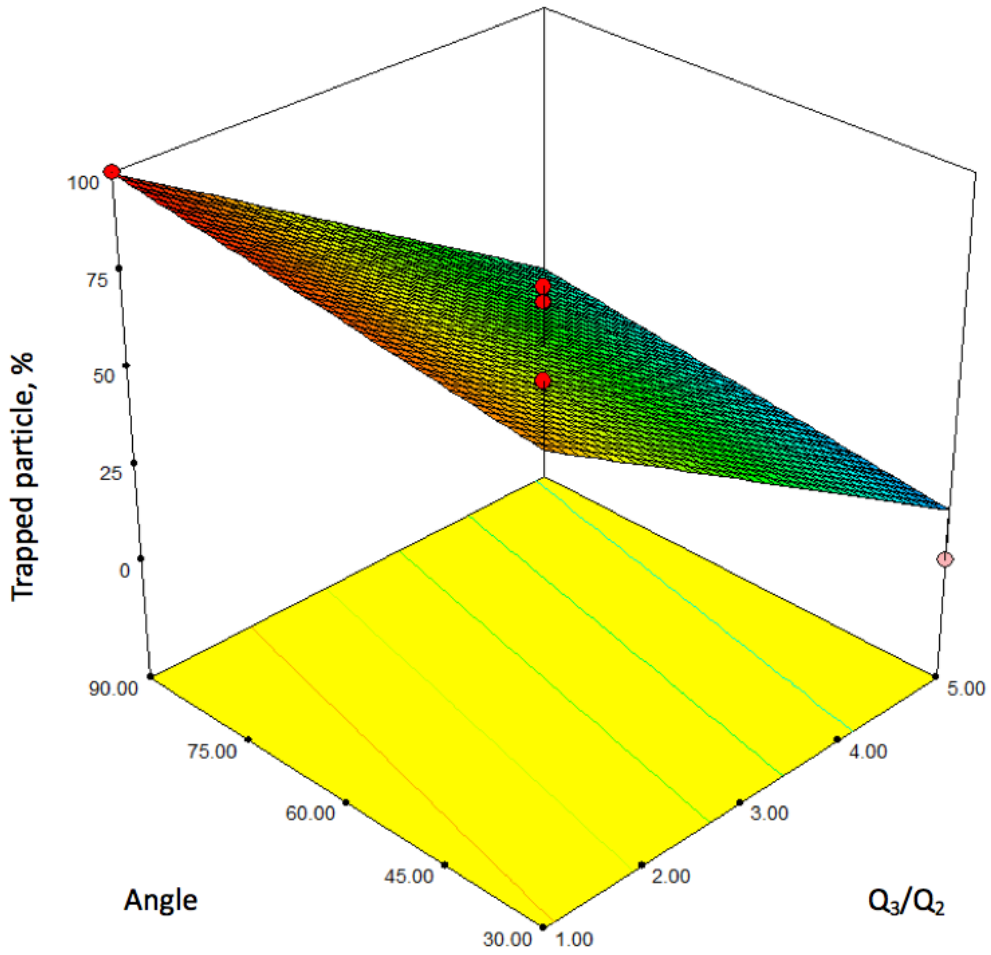


Figure 6.15 Contour-plot of percent of trapped particles: The effect of angle and Q_3/Q_2. Other variable is held at zero level. Q_1=25 μm/min.

After reviewing the literature, this is probably the first study to design PLT formation, involving tracing MKs and observing their behavior under different conditions. As known, computational fluid dynamics modeling is essential for a well-understanding of fluid dynamics in MKs [26].

Table 6.5 Optimum values of independent variables obtained with RSM

Independent variables	Optimum value
Angle, °	50.46
Q_1/Q_2	4.79
Q_3/Q_2	1.13

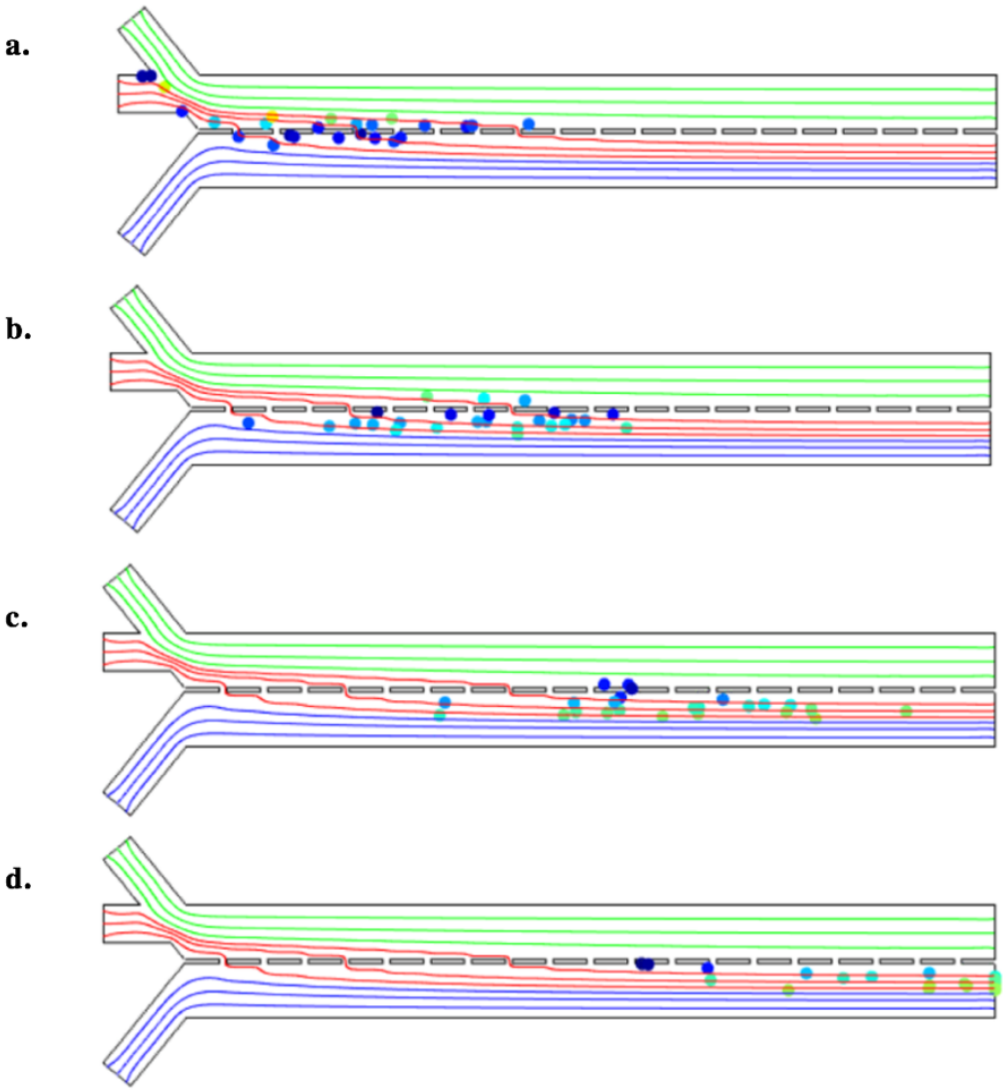


Figure 6.16 MKs locations at different times in a microchannel at the optimum values of physical conditions. α=50.46°, Q_1=23.95 μL/min, Q_2=5 μL/min, Q_3 = 5.65 μL/min a: Near the beginning time of the process b: Near the mid-time of the process c: After the mid-time of the process d: Near the end time of the process

Through simulation and modeling studies, we believe that once the well-understood flow behavior of MKs is provided, the efficiency of PLT production can be increased in a short time as less effort will be required to conduct experimental studies. This saves us time. We continue to work on computational fluid dynamics optimization to increase PLT production efficiency. Our future direction is to

model MK elongation and combine it with our current work to generate PLT. In this way, our knowledge of manufacturing high-throughput bioreactors for PLT production will expand.

6.5 Fabrication of Different Geometries for Platelet Formation

There are two approaches for PLT production from MKs. The first is like the bone marrow; the second is like the pulmonary vascular structure in the human body. The second is more complex than the other. Because the lung structure is slightly different and the lungs contain a large number of vessels of different diameters.

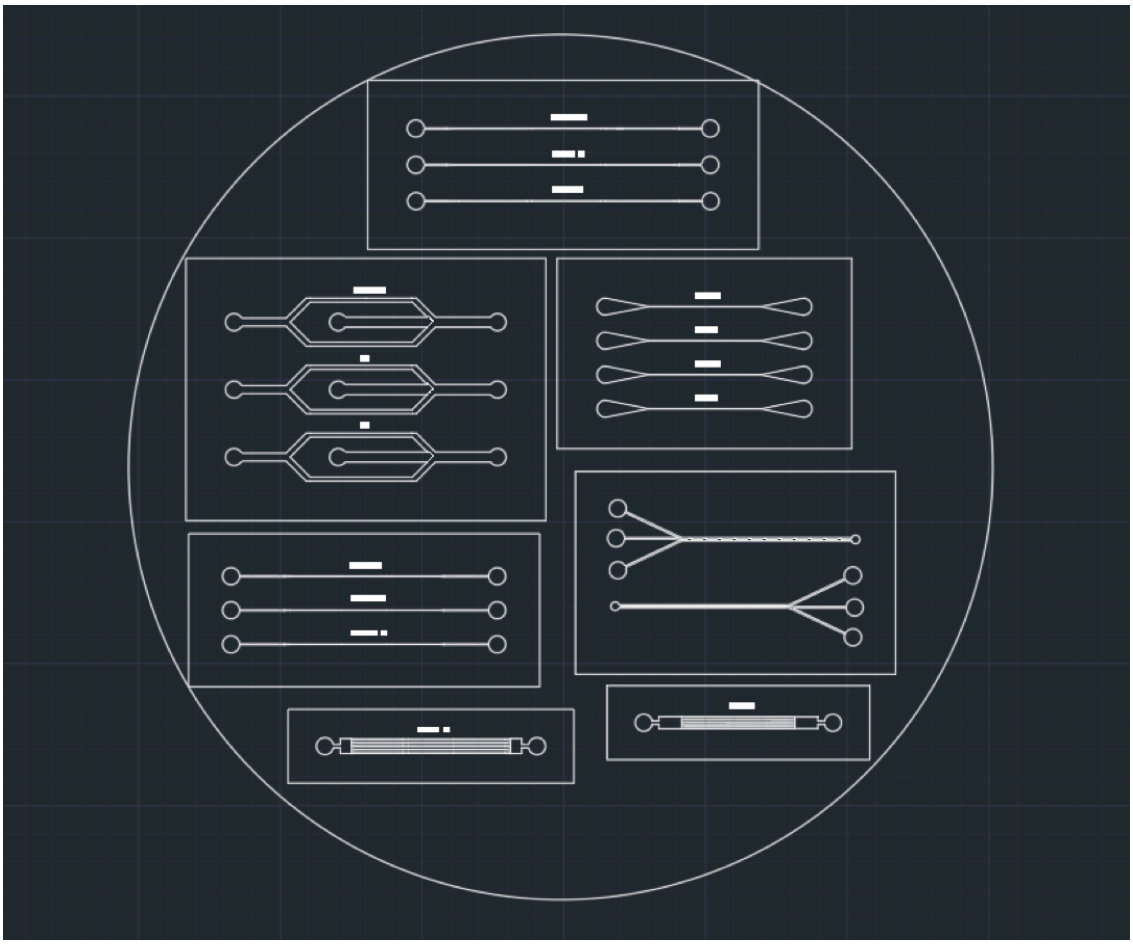


Figure 6.17 A general overview of chrome mask

The main focus for the bone marrow structure is to create shear rate in the main stream. A single channel of standard diameter is sufficient for bone marrow geometry. A shear rate can be created in the main stream by adding a pressure stream. However, it is more challenging to create a geometry for the lung

structure. Gradually narrowing channels were designed to create narrowing areas, or obstacles were added to a channel at different angles. As mentioned before, the chrome photomask production method was used for channels below 10 μm. The designs are shown in Figure 6.17.

Each design for the lung geometry is detailed in Figures 6.18-6.24. Figure 6.18 includes three microchannels with the same approach with different sizes. In this design, a channel structure can be likened to a cone, which gradually narrows and then expands gradually. With the progressive narrowing of the microchannel from the channel's entrance, it is expected that the MKs will elongate and turn into PLTs by breaking off in the narrowest region corresponding to the middle of the channel.

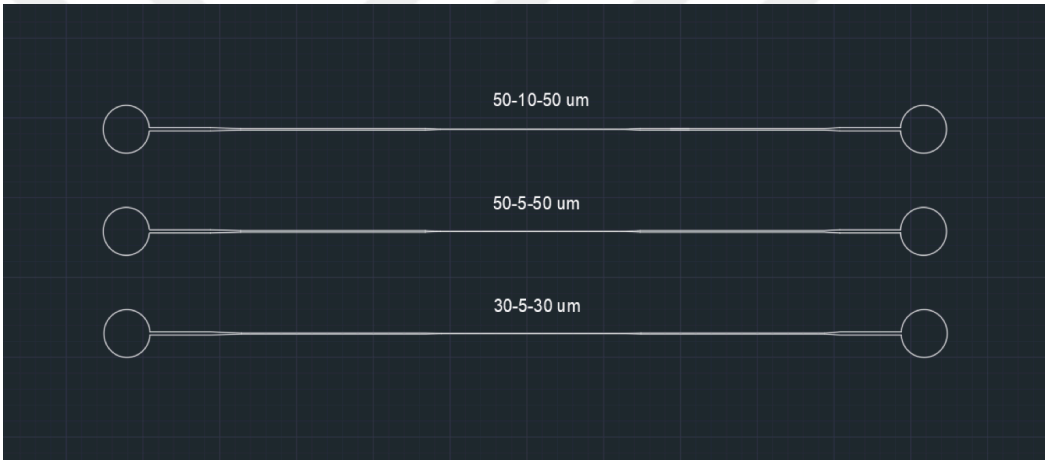


Figure 6.18 Gradual narrowing and expanding channel design

Then, in the last region, where the channel widens again, a PLT pool is expected to form. The microchip, shown in Figure 6.18, was produced under cleanroom conditions. Figure 6.19 includes three designs created with the same approach, but only the angle of placement of the pillars located inside the chip is different. This geometry is designed considering that the MKs that will pass through the elliptical pillars placed in the chip will elongate and break, with the MK feeding from the middle inlet and the pressure flow feeding on the main inlet. One of the most important features of this design is the distance between the elliptical pillars placed at specific angles to the center of the chip. Here, the distances between the pillars are around 7 μm, and the production of this microchip design is challenging and requires experience. The microchip, the design of which is shown in Figure

6.19, has been successfully produced under cleanroom conditions. Figure 6.20 includes a design that narrows in one step and can be compared to a cone. This microchannel design differs from the design in Figure 6.18 because it does not include an expansion area following the narrowing.

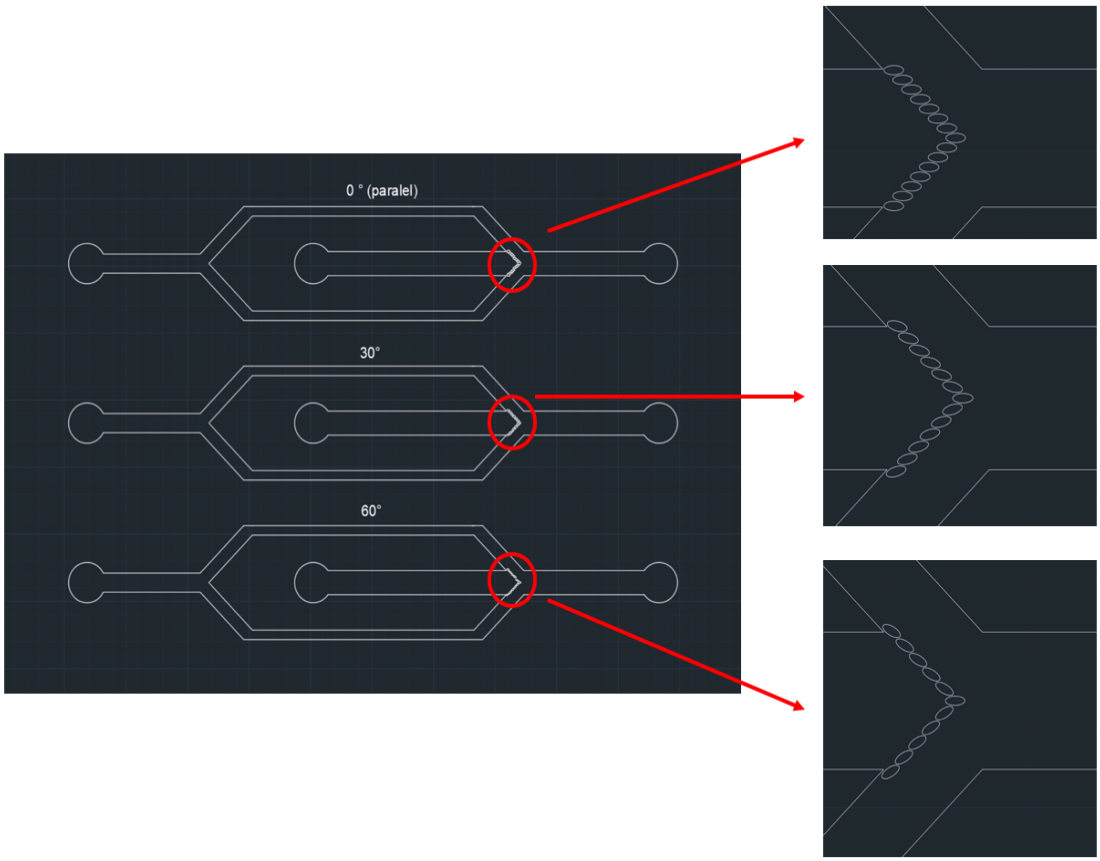


Figure 6.19 Channels including pillars with different angles

With the gradual narrowing of the microchannel from the channel's entrance, it is expected that the MKs will elongate and eventually turn into PLTs by breaking off with the flow effect. The microchip dimensions of the designed geometry are detailed in the figure. The microchip, which is shown in Figure 6.20, has been successfully produced under clean room conditions.

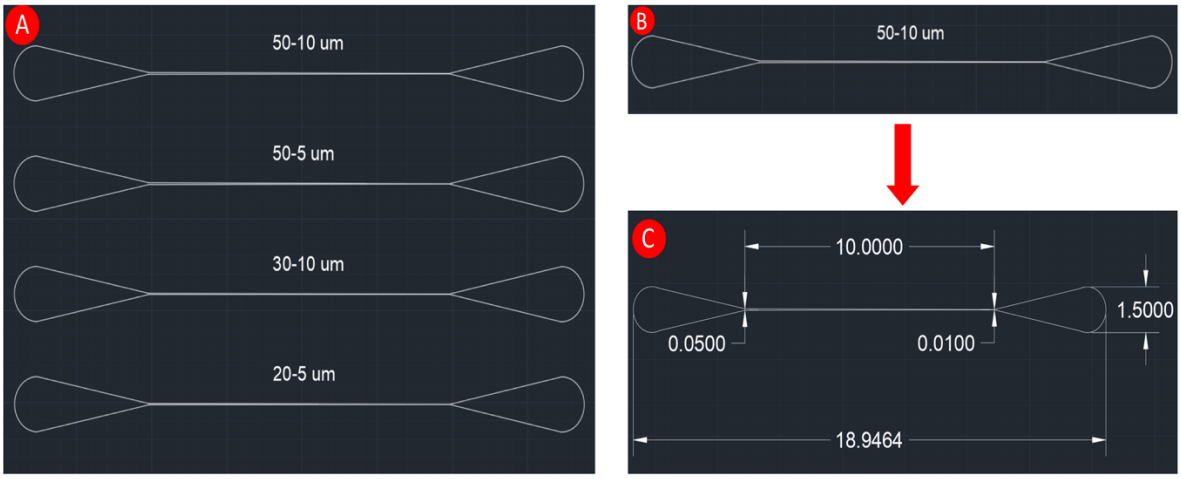


Figure 6.20 Gradual narrowing channel design with one step

Figure 6.21 includes a design that narrows in two steps and can be compared to a cone. The difference of this microchannel design from the design in Figure 6.20 because it does not contain a second narrowing area following the first narrowing.



Figure 6.21 Gradual narrowing channel design with two steps

With the gradual narrowing of the microchannel in two steps from the channel's entrance, it is expected that MKs of different sizes will elongate without accumulation and eventually break off with the effect of flow and turn into PLTs. The microchip dimensions of the designed geometry are detailed in the figure. The microchip, which is shown in Figure 6.20, has been successfully produced under cleanroom conditions.

Since the microfluidic chip design seen in Figure 6.22 is one of the designs that can be used most effectively within the scope of the thesis objectives, modeling and optimization studies have been carried out on this design.

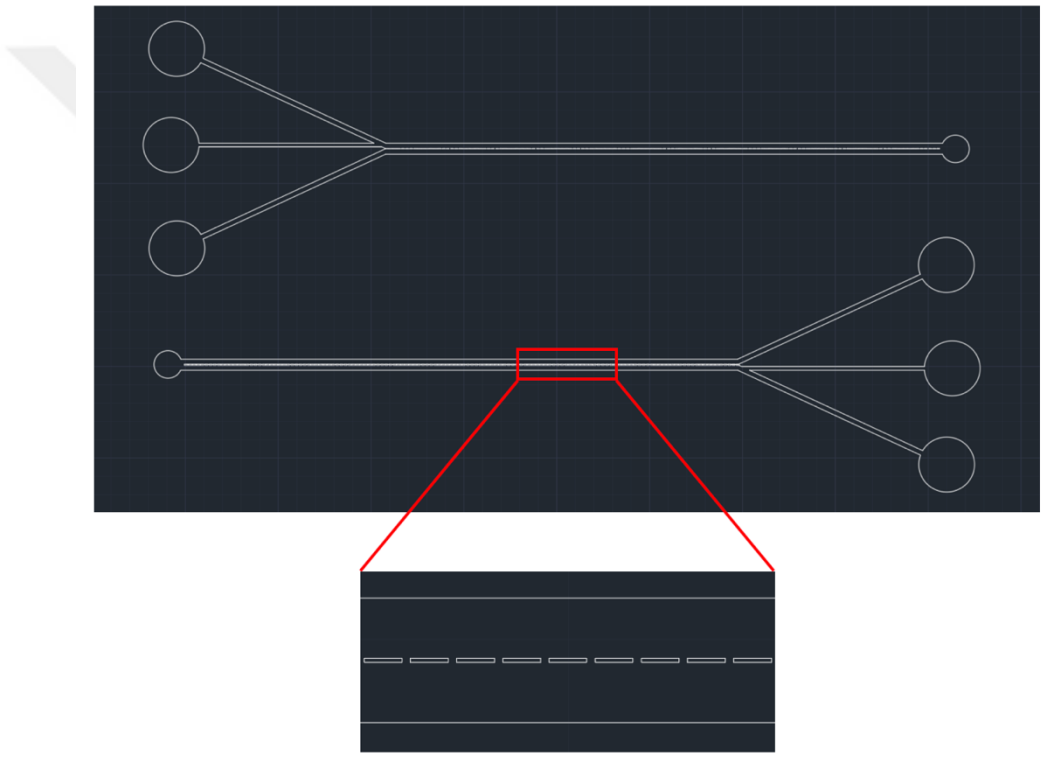


Figure 6.22 Channels including pillars with 90 x 10 μm with 2 μm apart

The details of the flow dynamics foreseen in the designed geometry are examined in detail in Sections 6.3-6.4. The microchip, the design of which is shown in Figure 6.22, has been successfully produced under clean room conditions. Figure 6.23 includes a design in which the flow fed from a single inlet will be directed to 5 separate microchannels, and each of these channels can be narrowed in two steps and resemble a cone.

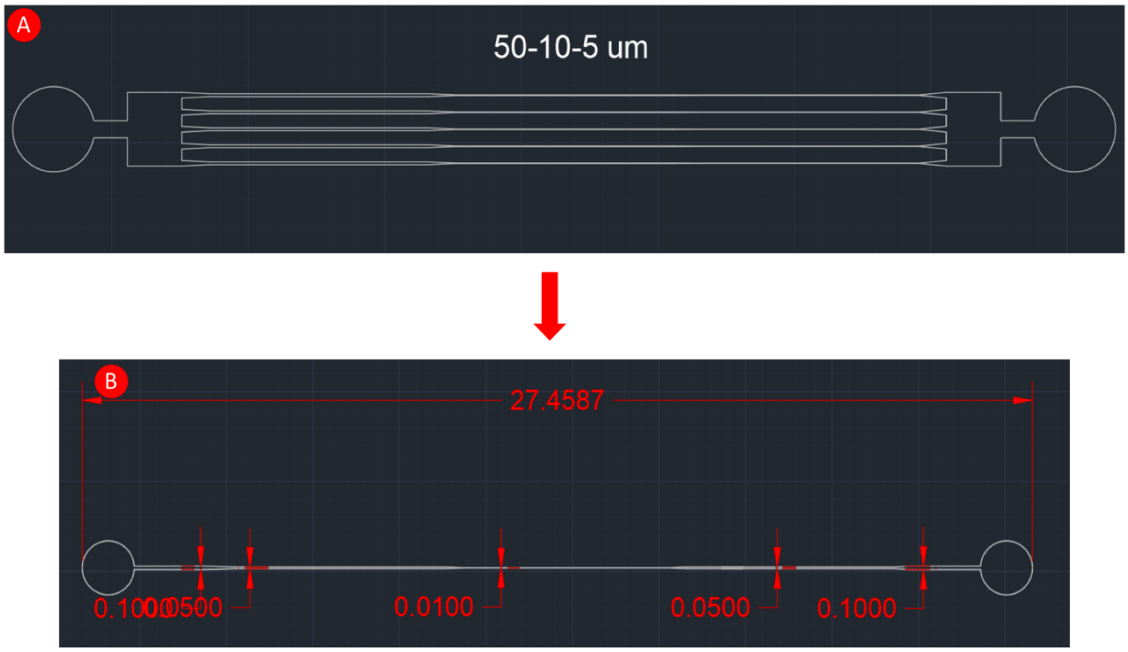


Figure 6.23 Repetitive gradual narrowing channel design with two steps in one microchip

Although this microchannel design is very similar to the design of the microchannels seen in Figure 6.21, there are some differences. Each microchannel of the microchip in Figure 6.21 has different dimensions, but each channel has its input and output. In Figure 6.23, the microchip containing five microchannels has a single input and a single output. The microchip, the design of which is shown in Figure 6.23, has been successfully produced under cleanroom conditions.

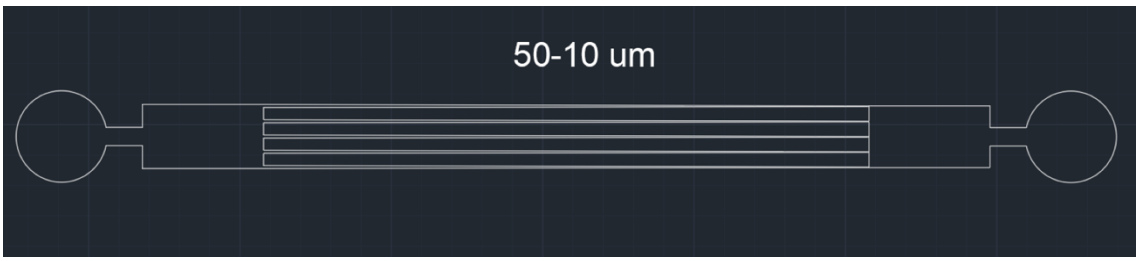


Figure 6.24 One step repetitive tapering channel design in a single microchip

Figure 6.24 includes a design in which the flow fed from a single inlet will be directed to 5 separate microchannels, and each of these channels can be narrowed in one step and resemble a cone. Although this microchannel design is very similar to the design of the microchannels seen in Figure 6.20, there are some differences. Although each microchannel of the microchip in Figure 6.20 has different dimensions, each channel has its own input and output. In Figure 6.24, the

microchip containing five microchannels has a single input and a single output. The microchip, the design of which is shown in Figure 6.24, has been successfully produced under clean room conditions.

The objectives set at the beginning of the thesis and significant outcomes are given below:

Objective 1: Determination of channel geometry and shear stresses by finite element method

The results of the studies carried out to achieve this goal are detailed under the heading 6.4. As foreseen in plan B of this target, 3D simulation studies were very time-consuming, so 2D simulations were carried out. These studies were carried out at Yildiz Technical University.

Objective 2: Microfluidic chip fabrication

The results of the studies carried out to achieve this goal are detailed under the heading 6.5. Although it has successfully produced channels under 10 microns and achieved success for this target, the supply of chrome masks for this process has been quite difficult and time consuming. The necessity of obtaining the chrome mask from abroad and the possibility of X-ray rays to disrupt the structure of the chrome mask made this process difficult. With the Ancar chrome mask being supplied without any problems, the desired microchip production was accomplished without the need for any B plan. These studies were carried out at Gebze Technical University.

Objective 3: Isolation of MK

The results of the studies carried out to achieve this goal are detailed under the heading 6.1. The isolation procedure was determined for MKs obtained by differentiation of hematopoietic stem cells isolated from the bone marrow of mice in culture medium, and the images of the obtained MKs under the microscope were reported. These studies were carried out at Yeditepe University.

If all the studies carried out within the scope of the thesis study are evaluated, the PLT production process from MKs can be examined in two stages; the first of these is to compress the MKs with the effect of flow, and the second is the elongation of

the proPLTs. Within the scope of this thesis, only the first step of the process is focused on, which aims to capture more MK with the help of flow pressure.

As stated in the literature, it is an undeniable fact that the angle between the main and pressure flows should be close to 60 degrees in the microchip geometry where PLT formation will be examined [5]. While the current studies give results on PLT production efficiency, in this study carried out within the scope of the thesis, the results are given over the imprisoned MKs. Although there is such a difference, the simulation results are in line with the literature data. Therefore, this study is promising.

Based on our simulation and optimization results, the maximum number of MKs is trapped when the angle between the pressure and the main flow channel is 50.46 degrees. On the other hand, we conclude that the contribution of the ratio of the velocity of the pressure flow to the velocity of the main flow is more significant than the angle between the flow channels on the percentage of MKs trapped. Given the nature of PLT formation, the effect of the angle between the main and pressure flows will not be sufficiently effective on its own unless the necessary MK confinement and elongation effects occur. In this study, 2D modeling was performed to simplify the system, since the width of the microchannel is large enough. Also, 2D modeling is preferred over 3D modeling because in 2D modeling, much higher spatial and temporal resolution can be achieved numerically compared to a similar 3D simulation [61]. In addition, 2D can be used instead of 3D in cases where the channel width is neglected [62][63].

It is clear that the physical interaction of biological particles and the walls of microchannels is important [64]. However, we ignored this interaction, which may be a limitation in our simulations. From a general point of view, it is necessary to examine the passage of MKs through crevices/obstacles more regularly. Best results will be obtained considering the elongation process after passing through the slit.

REFERENCES

[1] K. R. Machlus and J. E. Italiano, “The incredible journey: From megakaryocyte development to platelet formation,” *J. Cell Biol.*, vol. 201, no. 6, pp. 785–796, 2013.

[2] C. A. Di Buduo *et al.*, “Programmable 3D silk bone marrow niche for platelet generation ex vivo and modeling of megakaryopoiesis pathologies,” *Blood*, vol. 125, no. 14, pp. 2254–2264, 2015.

[3] A. C. Schlinker, K. Radwanski, C. Wegener, K. Min, and W. M. Miller, “Separation of in-vitro-derived megakaryocytes and platelets using spinning-membrane filtration,” *Biotechnol. Bioeng.*, vol. 112, no. 4, pp. 788–800, 2015.

[4] A. Baigger, D. Eicke, R. Blasczyk, C. Figueiredo, "Large-scale cultures and bioreactors for the production of megakaryocytes and platelets," *Scientific reports*, vol. 8, no. 1, pp. 1-11, 2017.

[5] Y. Nakagawa, S. Nakamura, M. Nakajima, H. Endo, T. Dohda, N. Takayama, ... & K. Eto, "Two differential flows in a bioreactor promoted platelet generation from human pluripotent stem cell–derived megakaryocytes," *Experimental hematology*, vol. 41, no. 8, pp. 742-748, 2013.

[6] J. N. Thon, L. Mazutis, S. Wu, J. L., Sylman, A. Ehrlicher, K. R. Machlus,... & D. A. Weitz, "Platelet bioreactor-on-a-chip," *Blood*, vol. 124, no. 12, pp. 1857-1867, 2014.

[7] M. P. Avanzi, O. E. Oluwadara, M. M. Cushing, M. L. Mitchell, S. Fischer, and W. B. Mitchell, “A novel bioreactor and culture method drives high yields of platelets from stem cells,” *Transfusion*, vol. 56, no. 1, pp. 170–178, 2016.

[8] A. Balduini, C. A. Di Buduo, and D. L. Kaplan, “Translational approaches to functional platelet production ex vivo,” *Thromb. Haemost.*, vol. 115, no. 2, pp. 250–256, 2016.

[9] I. Pallotta, M. Lovett, D. L. Kaplan, & A. Balduini, "Three-dimensional system for the in vitro study of megakaryocytes and functional platelet production using silk-based vascular tubes," *Tissue Engineering Part C: Methods*, vol. 17, no. 12, pp. 1223-1232, 2011.

[10] A. Blin, A. Le Goff, A. Magniez, S. Poirault-Chassac, B. Teste, G. Sicot, ... & D. Baruch, "Microfluidic model of the platelet-generating organ: beyond bone marrow biomimetics," *Scientific reports*, vol. 6, pp. 1-8, 2016.

[11] A. F. Martinez, R. D. McMahon, M. Horner, and W. M. Miller, “A uniform-shear rate microfluidic bioreactor for real-time study of proplatelet formation and rapidly-released platelets,” *Biotechnol. Prog.*, vol. 33, no. 6, pp. 1614–1629, 2017.

[12] G. Ingavle, N. Shabrani, A. Vaidya, and V. Kale, “Mimicking megakaryopoiesis in vitro using biomaterials: Recent advances and future opportunities,” *Acta Biomater.*, vol. 96, pp. 99–110, 2019.

[13] S. Nishimura *et al.*, “IL-1α induces thrombopoiesis through megakaryocyte rupture in response to acute platelet needs,” *J. Cell Biol.*, vol. 209, no. 3, pp. 453–466, 2015.
[14] X. Sim, M. Poncz, P. Gadue, and D. L. French, “Understanding platelet generation from megakaryocytes: Implications for in vitro-derived platelets,” *Blood*, vol. 127, no. 10, pp. 1227–1233, 2016.
[15] J.N. Thon and J.E., Italiano, “Platelet Formation,” *Semin. Hematol.*, vol. 47, no. 3, pp. 220–226, 2010.
[16] M. Bender *et al.*, “Microtubule sliding drives proplatelet elongation and is dependent on cytoplasmic dynein,” *Blood*, vol. 125, no. 5, pp. 860–868, 2015.
[17] S. J. Lu *et al.*, “Platelets generated from human embryonic stem cells are functional in vitro and in the microcirculation of living mice,” *Cell Res.*, vol. 21, no. 3, pp. 530–545, 2011.
[18] K. R. Machlus, J. N. Thon, and J. E. Italiano, “Interpreting the developmental dance of the megakaryocyte: A review of the cellular and molecular processes mediating platelet formation,” *Br. J. Haematol.*, vol. 165, no. 2, pp. 227–236, 2014.
[19] J. N. Thon *et al.*, “Microtubule and cortical forces determine platelet size during vascular platelet production,” *Nat. Commun.*, vol. 3, no. May, pp. 852–859, 2012.
[20] J. N. Thon, D. A. Medvetz, S. M. Karlsson, and J. E. Italiano, “Road blocks in making platelets for transfusion,” *J. Thromb. Haemost.*, vol. 13, no. S1, pp. S55–S62, 2015.
[21] Y. X. Ru, S. X. Dong, H. yue Liang, and S. X. Zhao, “Platelet production of megakaryocyte: A review with original observations on human in vivo cells and bone marrow,” *Ultrastruct. Pathol.*, vol. 40, no. 4, pp. 163–170, 2016.
[22] J. N. Thon and S. M. Karlsson, “Scale-up of platelet production from human pluripotent stem cells for developing targeted therapies: advances & challenges,” *Cell Gene Ther. Insights*, vol. 3, no. 9, pp. 701–718, 2017.
[23] E. Lefrançais *et al.*, “The lung is a site of platelet biogenesis and a reservoir for haematopoietic progenitors,” *Nature*, vol. 544, no. 7648, pp. 105–109, 2017.
[24] T. Matsunaga *et al.*, “ Ex Vivo Large-Scale Generation of Human Platelets from Cord Blood CD34 + Cells ,” *Stem Cells*, vol. 24, no. 12, pp. 2877–2887, 2006.
[25] Y. Ito *et al.*, “Turbulence Activates Platelet Biogenesis to Enable Clinical Scale Ex Vivo Production,” *Cell*, vol. 174, no. 3, pp. 636-648.e18, 2018.
[26] J. N. Thon, B. J. Dykstra, and L. M. Beaulieu, “Platelet bioreactor: accelerated evolution of design and manufacture,” *Platelets*, vol. 28, no. 5, pp. 472–477, 2017.
[27] B. Sullenbarger, J. Hwan Bahng, R. Gruner, N. Kotov, and L. C. Lasky, “Prolonged Continuous In Vitro Human Platelet Production Using 3D Scaffolds.,” *Exp. Hematol.*, vol. 37, no. 1, pp. 101–110, 2009.
[28] C. Dunois-Lardé, C. Capron, S. Fichelson, T. Bauer, E. Cramer-Bordé, and D. Baruch, “Exposure of human megakaryocytes to high shear rates accelerates platelet production,” *Blood*, vol. 114, no. 9, pp. 1875–1883, 2009.

[29] A. M. Mitchell WB, "(12) United States Patent," 2017.
[30] M. T. Rondina and A. S. Weyrich, "Regulation of the genetic code in megakaryocytes and platelets," *J. Thromb. Haemost.*, vol. 13, no. S1, pp. S26–S32, 2015.
[31] G. M. Whitesides, "The origins and the future of microfluidics," *Nature*, vol. 442, pp. 368–373, 2006.
[32] C. G. Yang, Z. R. Xu, and J. H. Wang, "Manipulation of droplets in microfluidic systems," *TrAC - Trends Anal. Chem.*, vol. 29, no. 2, pp. 141–157, 2010.
[33] Z. Zhang and S. Nagrath, "Microfluidics and cancer: Are we there yet?," *Biomed. Microdevices*, vol. 15, no. 4, pp. 595–609, 2013.
[34] J. M. Chan, K. H. K. Wong, A. M. Richards, and C. L. Drum, "Microengineering in cardiovascular research: New developments and translational applications," *Cardiovasc. Res.*, vol. 106, no. 1, pp. 9–18, 2015.
[35] G. C. Kocal *et al.*, "Dynamic Microenvironment Induces Phenotypic Plasticity of Esophageal Cancer Cells under Flow," *Sci. Rep.*, vol. 6, no. June, pp. 1–11, 2016.
[36] A. Siddique, T. Meckel, R. W. Stark, and S. Narayan, "Improved cell adhesion under shear stress in PDMS microfluidic devices," *Colloids Surfaces B Biointerfaces*, vol. 150, pp. 456–464, 2017.
[37] L. Lu, G. X. Zheng, Y. S. Yang, C. Y. Feng, F. F. Liu, and Y. H. Wang, "Measurement of Giardia lamblia adhesion force using an integrated microfluidic assay," *Anal. Bioanal. Chem.*, vol. 409, no. 5, pp. 1451–1459, 2017.
[38] K. F. Lei, "Microfluidic systems for diagnostic applications: A review," *J. Lab. Autom.*, vol. 17, no. 5, pp. 330–347, 2012.
[39] J. C. Mcdonald *et al.*, "Fabrication of microfluidic systems in poly (dimethylsiloxane)," *Electrophoresis*, vol. 21, no. 1, pp. 27–40, 2000.
[40] N. T. Nguyen, M. Hejazian, C. H. Ooi, and N. Kashaninejad, "Recent advances and future perspectives on microfluidic liquid handling," *Micromachines*, vol. 8, no. 6, 2017.
[41] E. W. K. Young and C. A. Simmons, "Macro- and microscale fluid flow systems for endothelial cell biology," *Lab Chip*, vol. 10, no. 2, pp. 143–160, 2010.
[42] J. Shemesh, I. Jalilian, A. Shi, G. Heng Yeoh, M. L. Knothe Tate, and M. Ebrahimi Warkiani, "Flow-induced stress on adherent cells in microfluidic devices," *Lab Chip*, vol. 15, no. 21, pp. 4114–4127, 2015.
[43] E. Gutierrez, B. G. Petrich, S. J. Shattil, M. H. Ginsberg, A. Groisman, and A. Kasirer-Friede, "Microfluidic devices for studies of shear-dependent platelet adhesion," *Lab Chip*, vol. 8, no. 9, pp. 1486–1495, 2008.
[44] M. J. Rosenbluth, W. A. Lam, and D. A. Fletcher, "Analyzing cell mechanics in hematologic diseases with microfluidic biophysical flow cytometry," *Lab Chip*, vol. 8, no. 7, pp. 1062–1070, 2008.
[45] F. J. Tovar-Lopez *et al.*, "A microfluidics device to monitor platelet aggregation dynamics in response to strain rate micro-gradients in flowing blood," *Lab Chip*, vol. 10, no. 3, pp. 291–302, 2010.
[46] A. M. Forsyth, J. Wan, W. D. Ristenpart, and H. A. Stone, "The dynamic behavior of chemically 'stiffened' red blood cells in microchannel flows,"

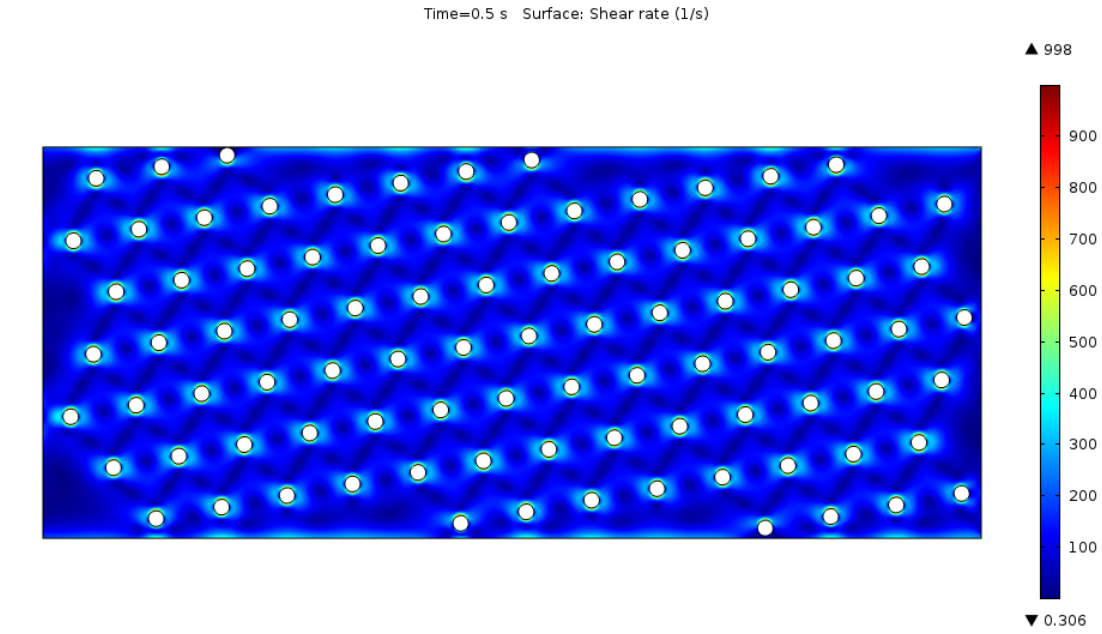
Microvasc. Res., vol. 80, no. 1, pp. 37–43, 2010.
[47] M. Li, D. N. Ku, and C. R. Forest, "Microfluidic system for simultaneous optical measurement of platelet aggregation at multiple shear rates in whole blood," *Lab Chip*, vol. 12, no. 7, pp. 1355–1362, 2012.
[48] G. Luka *et al.*, "Microfluidics integrated biosensors: A leading technology towards lab-on-A-chip and sensing applications," *Sensors (Switzerland)*, vol. 15, no. 12, pp. 30011–30031, 2015.
[49] E. Yeom, J. H. Park, Y. J. Kang, and S. J. Lee, "Microfluidics for simultaneous quantification of platelet adhesion and blood viscosity," *Sci. Rep.*, vol. 6, pp. 1–11, 2016.
[50] L. L. Lee PJ, Hung PJ, Rao VM, "Nanoliter Scale Microbioreactor Array for Quantitative Cell Biology," *Biotechnol. Bioeng.*, vol. 94, no. 1, pp. 1–14, 2006.
[51] J. C. Love, J. R. Anderson, and G. M. Whitesides, "F abrication of Microfluidic Systems by Soft," *Methods*, no. July, pp. 523–528, 2001.
[52] N. Gaio *et al.*, "Cytostretch, an Organ-on-Chip platform," *Micromachines*, vol. 7, no. 7, pp. 1–14, 2016.
[53] C. Multiphysics, "CFD Module User 's Guide," *COMSOL Multiphysics*, 2016.
[54] Y. Xia and G. M. Whitesides, "Soft Lithography," *Annu. Rev. Mater. Sci.*, vol. 28, no. 1, pp. 153–184, 1998.
[55] G. M. Whitesides, E. Ostuni, X. Jiang, and D. E. Ingber, "Soft Lithography in Biology," *Annu.Rev.Biomed*, vol. 3, pp. 335–373, 2001.
[56] G. S. Fiorini and D. T. Chiu, "Disposable microfluidic devices: Fabrication, function, and application," *Biotechniques*, vol. 38, no. 3, pp. 429–446, 2005.
[57] P. S. Dittrich and A. Manz, "Lab-on-a-chip: Microfluidics in drug discovery," *Nat. Rev. Drug Discov.*, vol. 5, no. 3, pp. 210–218, 2006.
[58] D. C. Duffy, J. C. McDonald, O. J. A. Schueller, and G. M. Whitesides, "Rapid prototyping of microfluidic systems in poly(dimethylsiloxane)," *Anal. Chem.*, vol. 70, no. 23, pp. 4974–4984, Dec. 1998.
[59] R. S. Kane, S. Takayama, E. Ostuni, D. E. Ingber, and G. M. Whitesides, "Patterning proteins and cells using soft lithography," in *The Biomaterials: Silver Jubilee Compendium*, Elsevier Ltd, 2006, pp. 161–174.
[60] L. Xiong, P. Chen, and Q. Zhou, "Adhesion promotion between PDMS and glass by oxygen plasma pre-treatment," *J. Adhes. Sci. Technol.*, vol. 28, no. 11, pp. 1046–1054, Jun. 2014.
[61] G. Boffetta and R. E. Ecke, "Two-dimensional turbulence," *Annu. Rev. Fluid Mech.*, vol. 44, pp. 427–451, 2011.
[62] Y. Zhang and X. Chen, "Dielectrophoretic microfluidic device for separation of red blood cells and platelets: a model-based study," *J. Brazilian Soc. Mech. Sci. Eng.*, vol. 42, no. 2, 2020.
[63] Y. Zhang and X. Chen, "Blood cells separation microfluidic chip based on dielectrophoretic force," *J. Brazilian Soc. Mech. Sci. Eng.*, vol. 42, no. 4, pp. 1–11, 2020.
[64] Z. B. Sendekie, A. Gaveau, R. G. H. Lammertink, and P. Bacchin, "Bacteria Delay the Jamming of Particles at Microchannel Bottlenecks," *Sci. Rep.*, vol. 6, pp. 1–10, 2016.

A

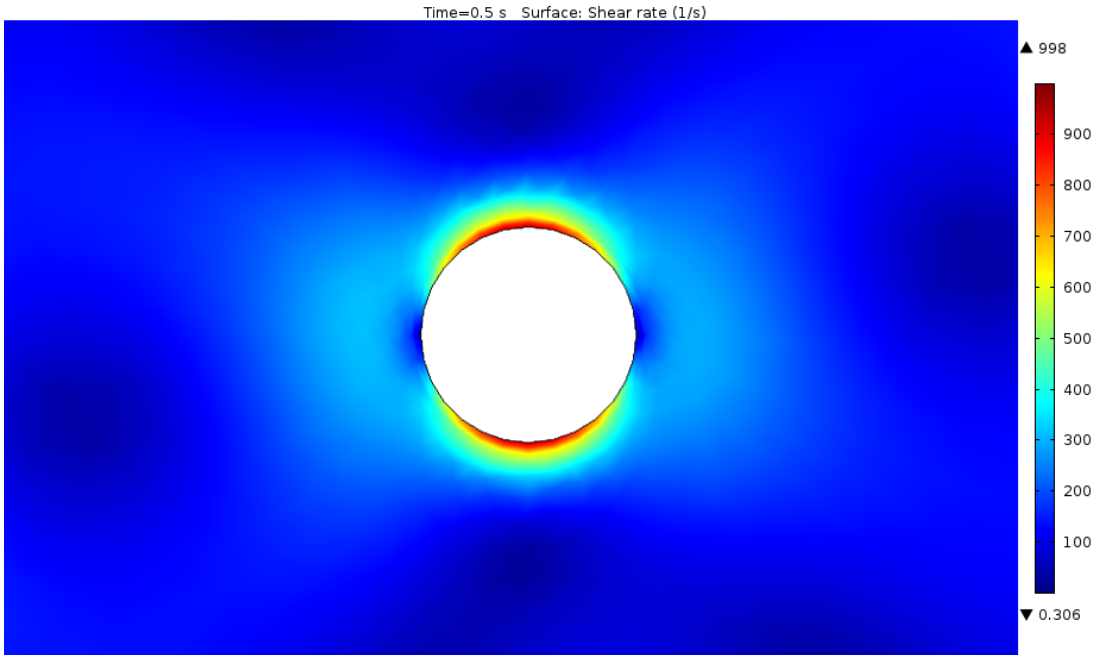
SIMULATION STUDIES

1. Results Obtained at Velocity 3000 μm/s

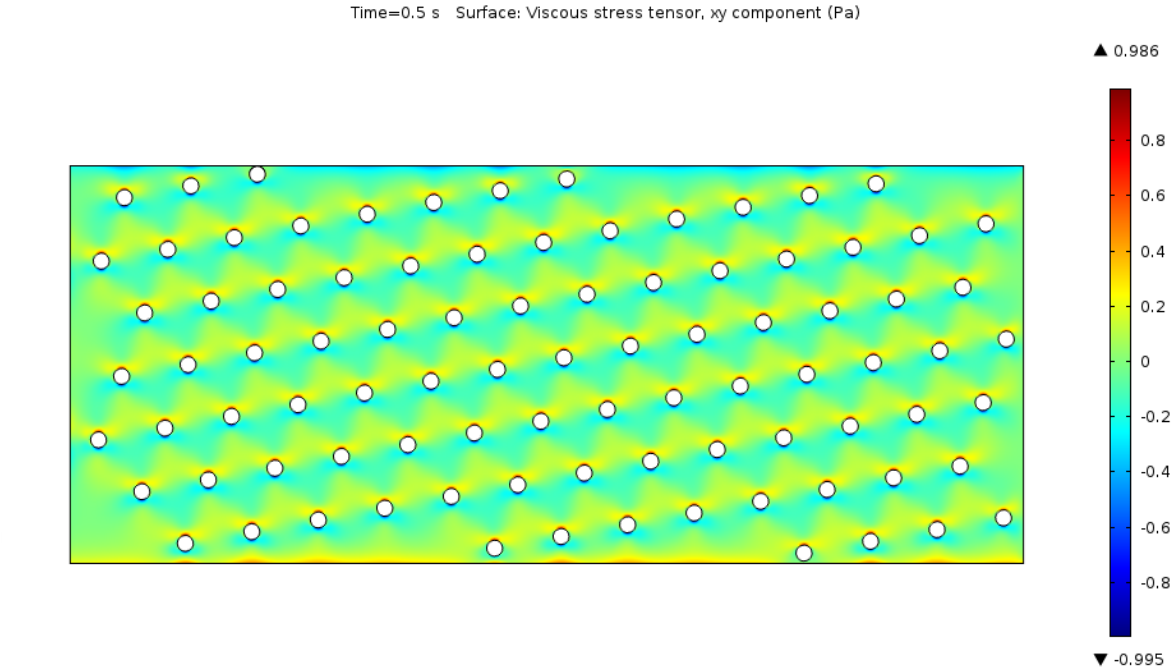
a



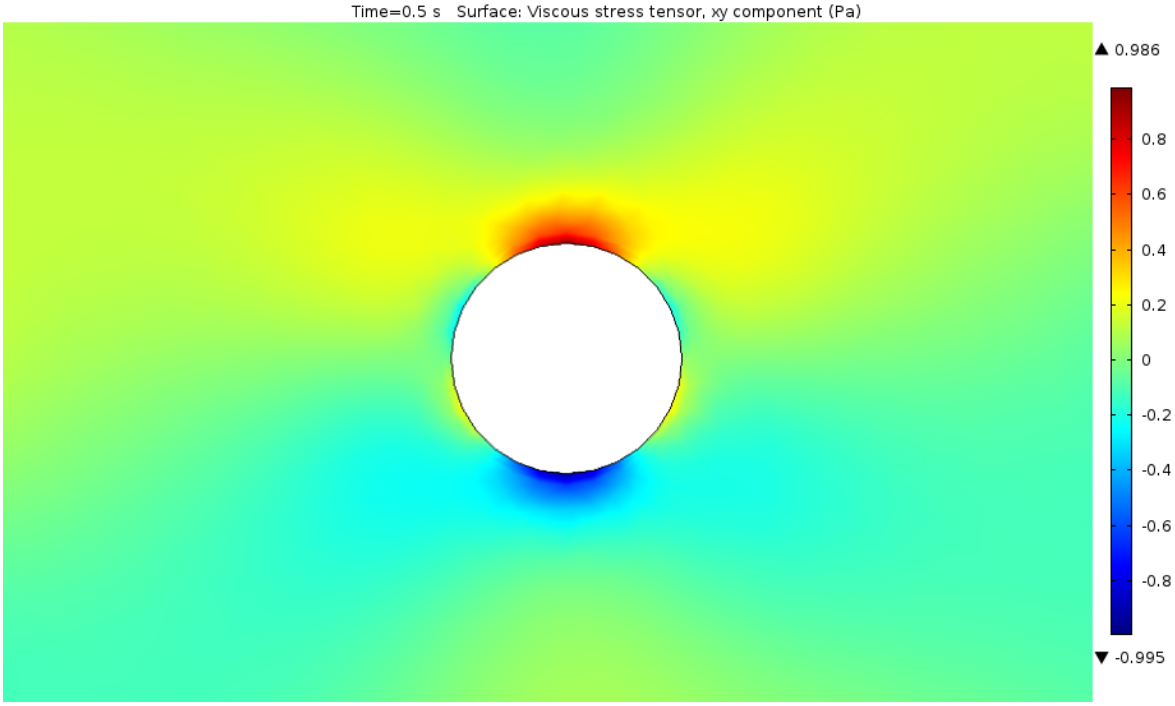
b



c

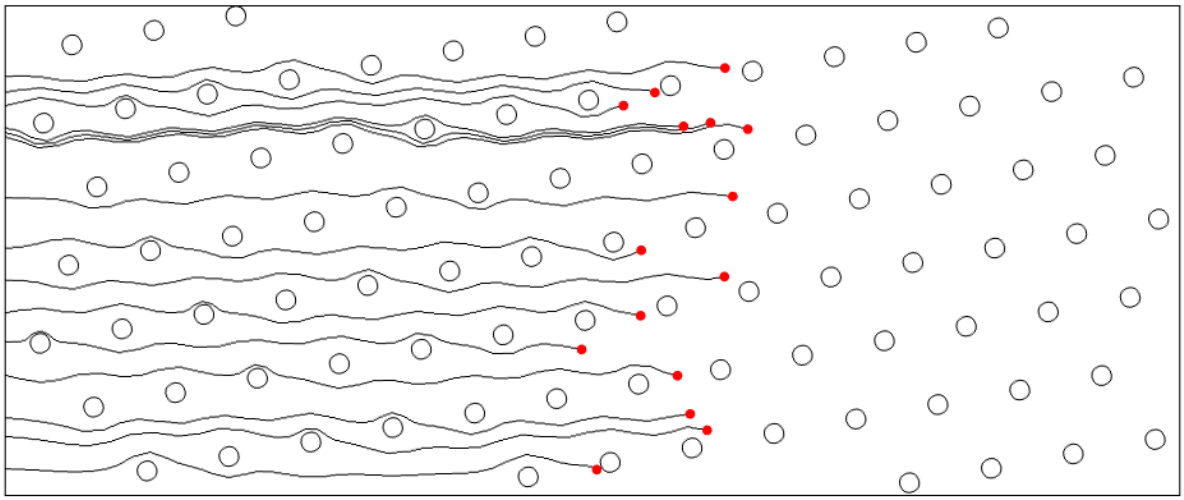

Time=0.5 s Surface: Viscous stress tensor, xy component (Pa)
▲ 0.986
0.8
0.6
0.4
0.2
0
-0.2
-0.4
-0.6
-0.8
▼ -0.995

d


Time=0.5 s Surface: Viscous stress tensor, xy component (Pa)
▲ 0.986
0.8
0.6
0.4
0.2
0
-0.2
-0.4
-0.6
-0.8
▼ -0.995

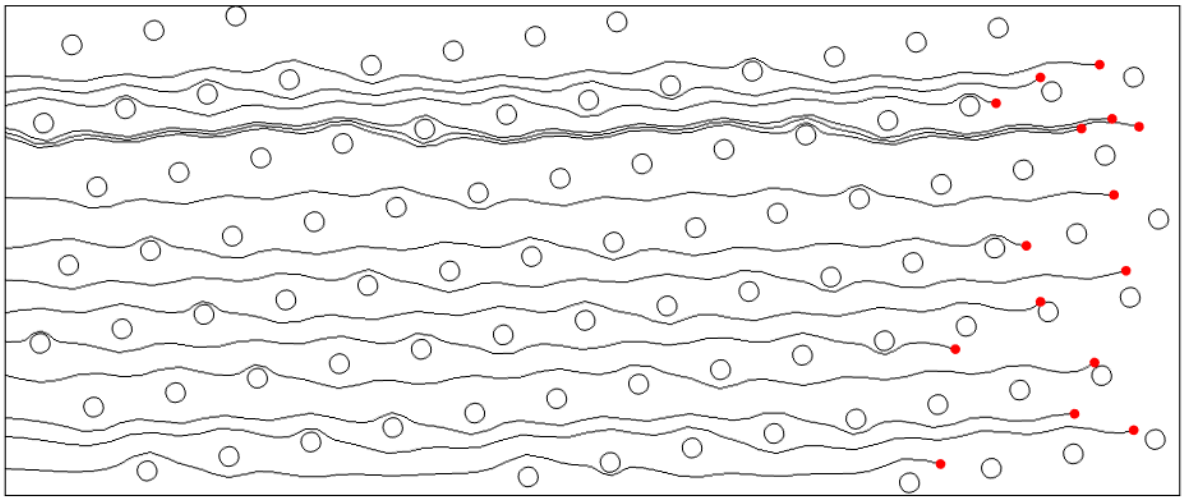
e

Time=0.2 s Particle trajectories

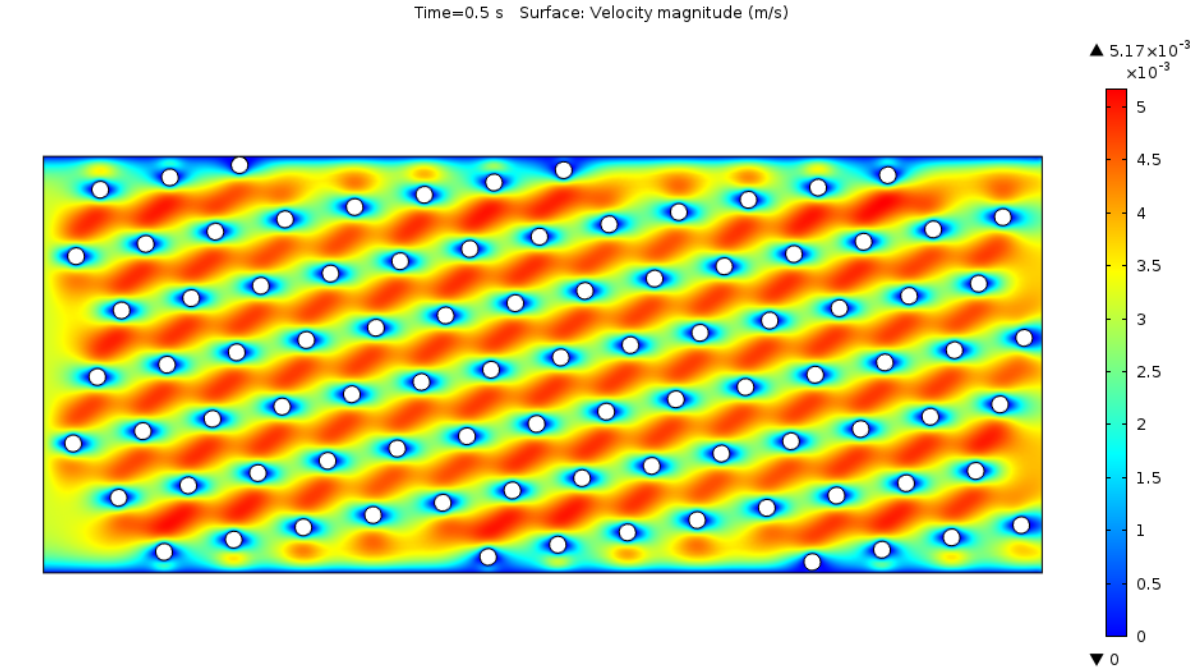


f

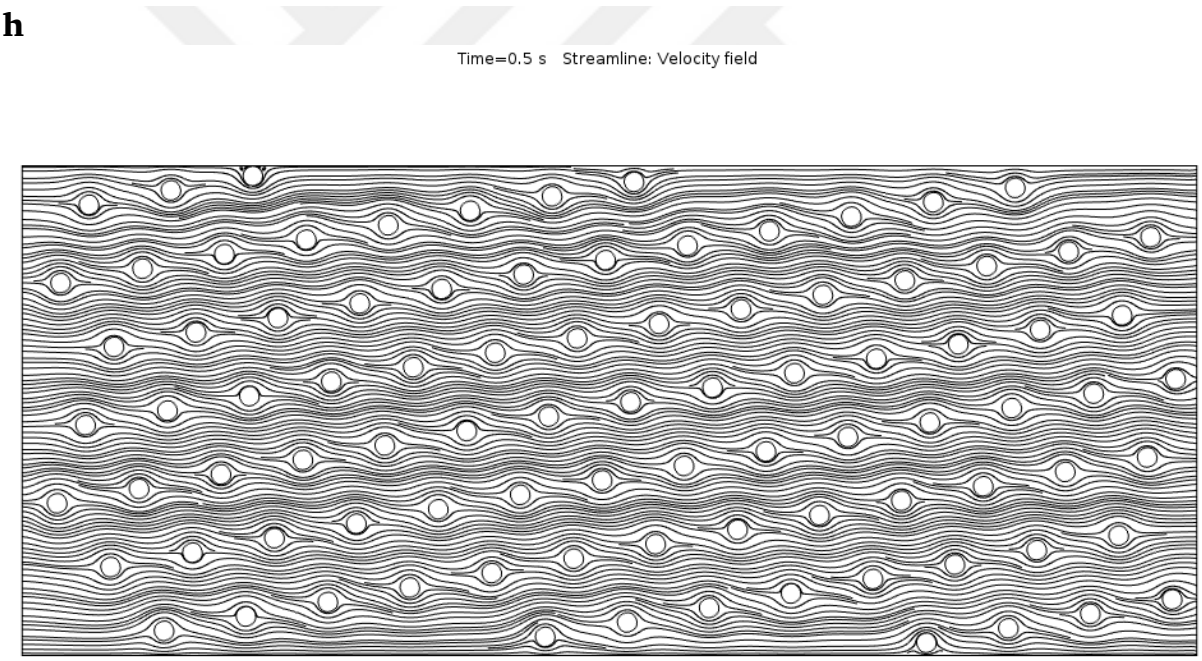
Time=0.32 s Particle trajectories



g

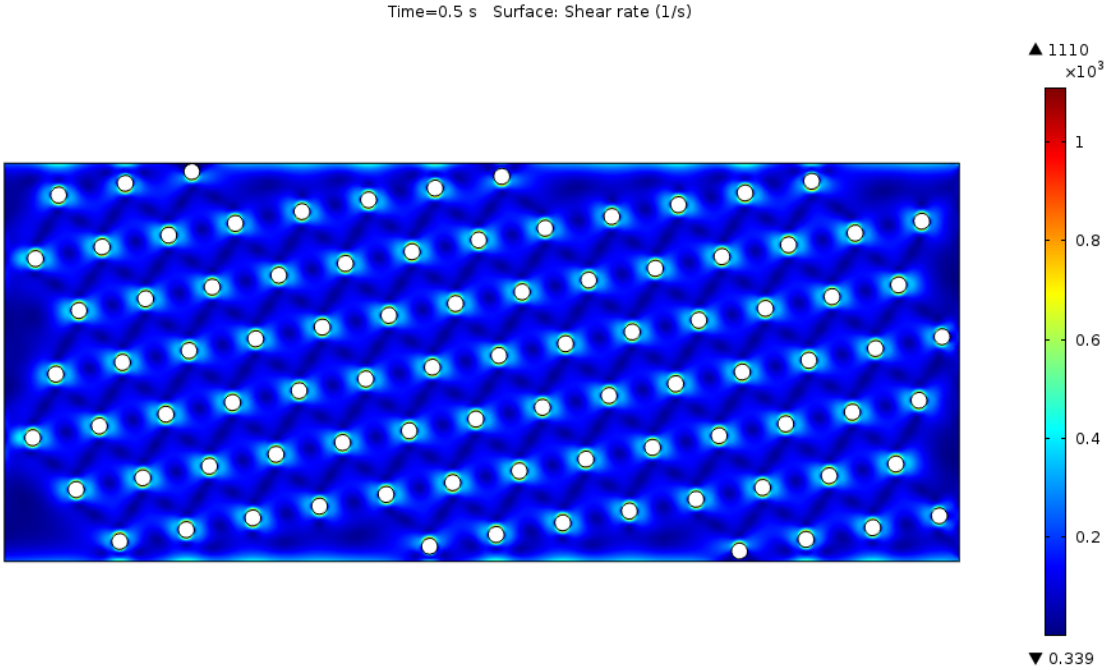

Time=0.5 s Surface: Velocity magnitude (m/s)
▲ 5.17×10^-3
×10^-3
5
4.5
4
3.5
3
2.5
2
1.5
1
0.5
0
▼ 0

h

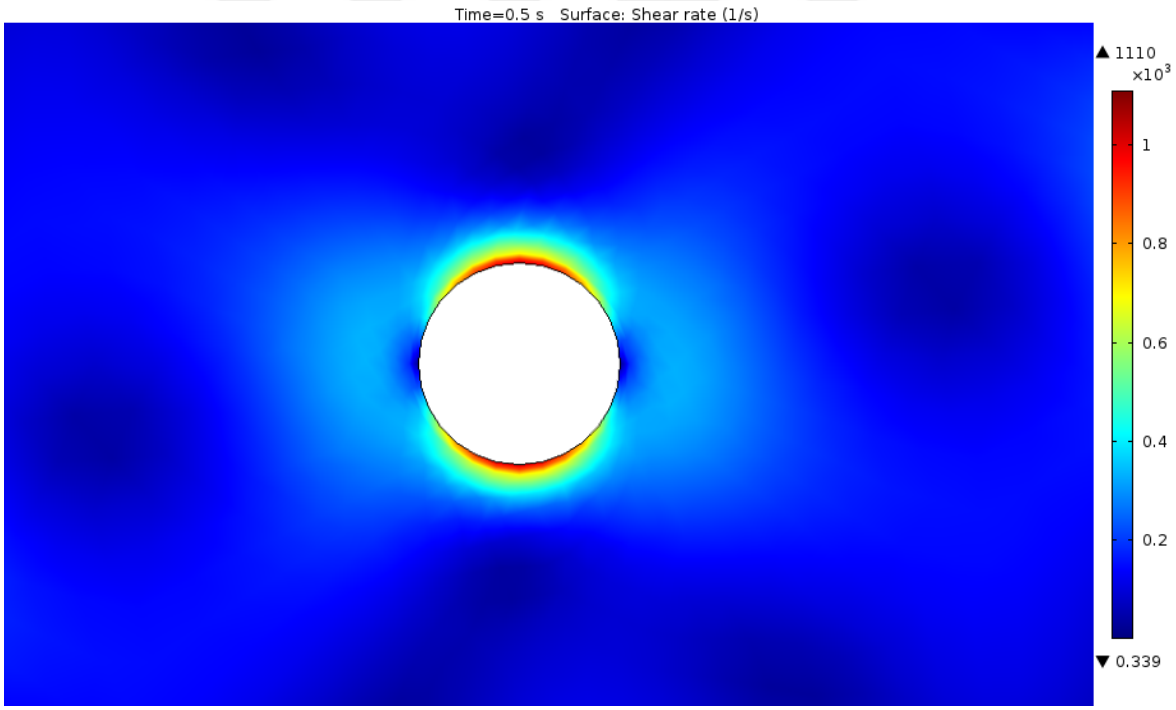

Time=0.5 s Streamline: Velocity field

2. Results Obtained at Velocity 3333.33 µm/s

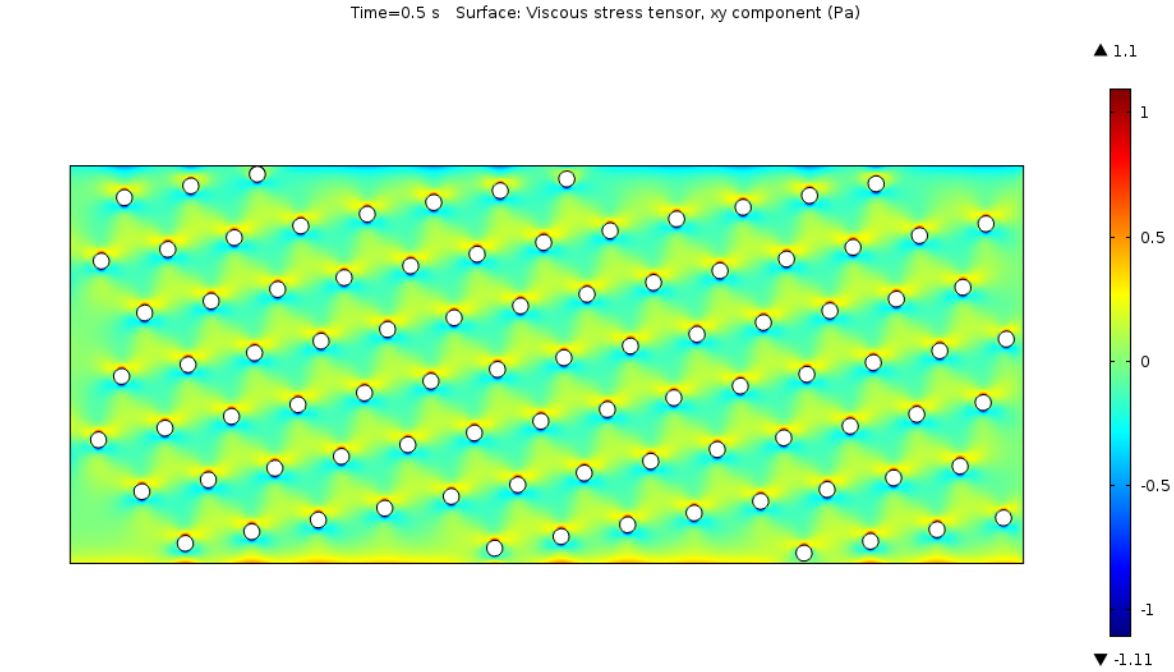
a



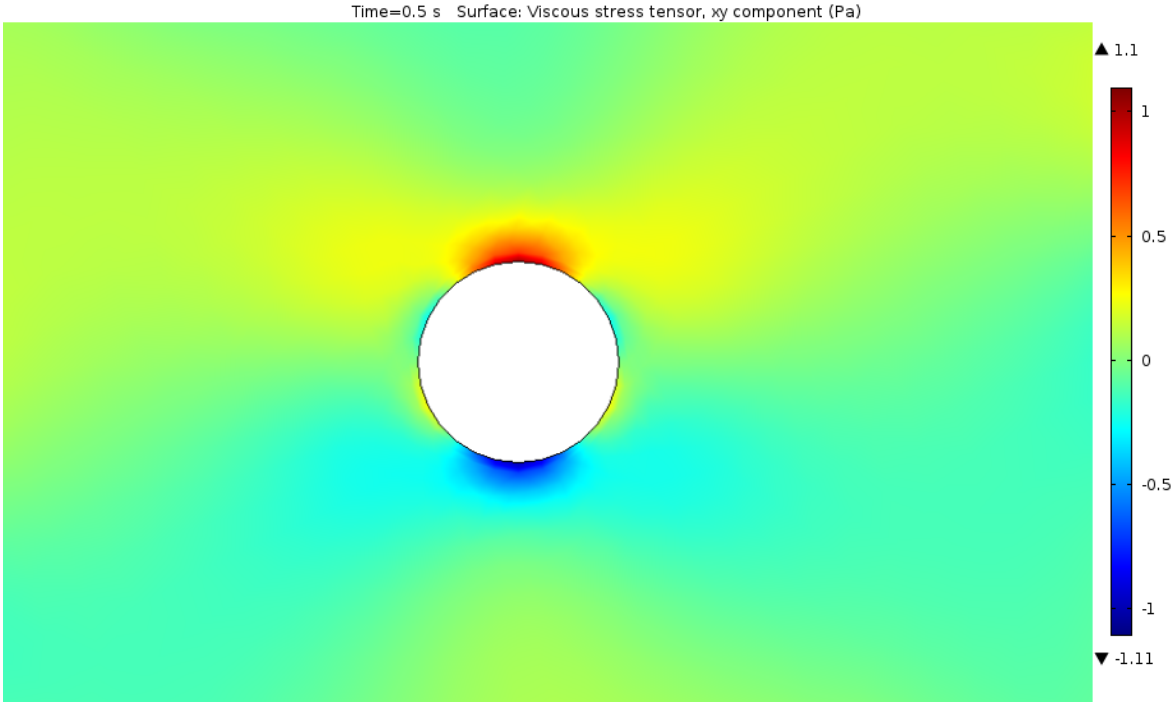
b



c

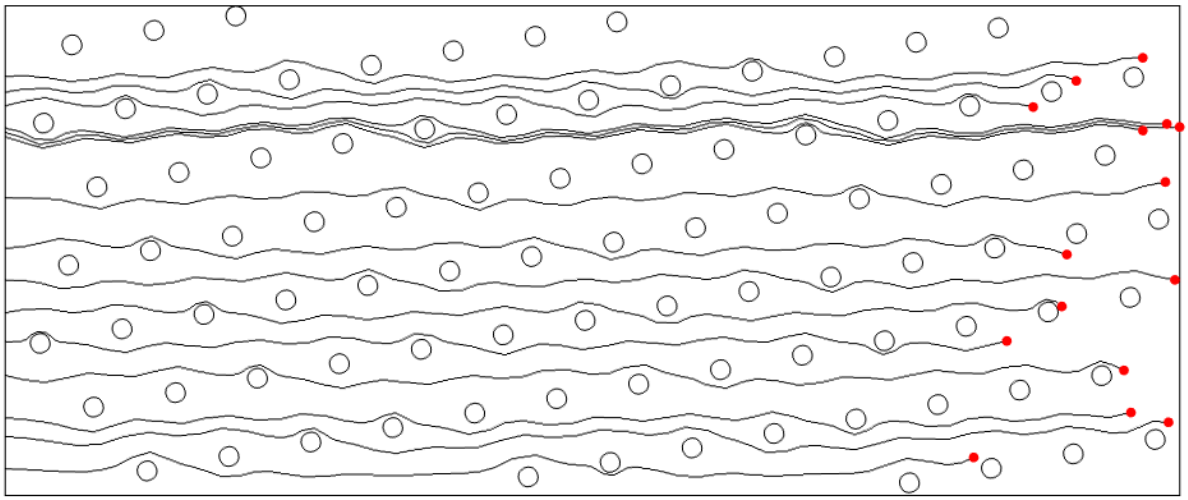

Time=0.5 s Surface: Viscous stress tensor, xy component (Pa)
▲ 1.1
1
0.5
0
-0.5
-1
▼ -1.11

d


Time=0.5 s Surface: Viscous stress tensor, xy component (Pa)
▲ 1.1
1
0.5
0
-0.5
-1
▼ -1.11

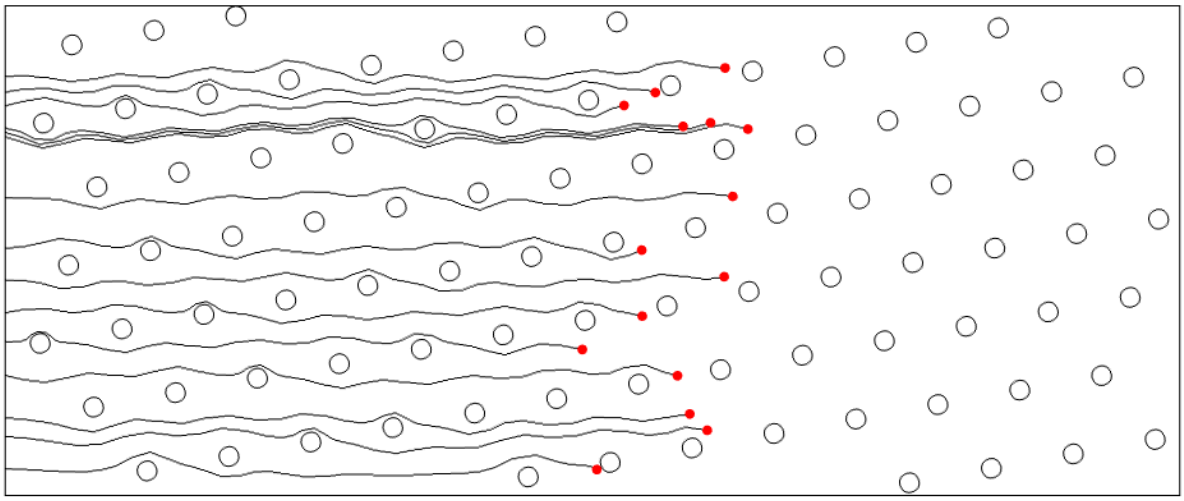
e

Time=0.3 s Particle trajectories

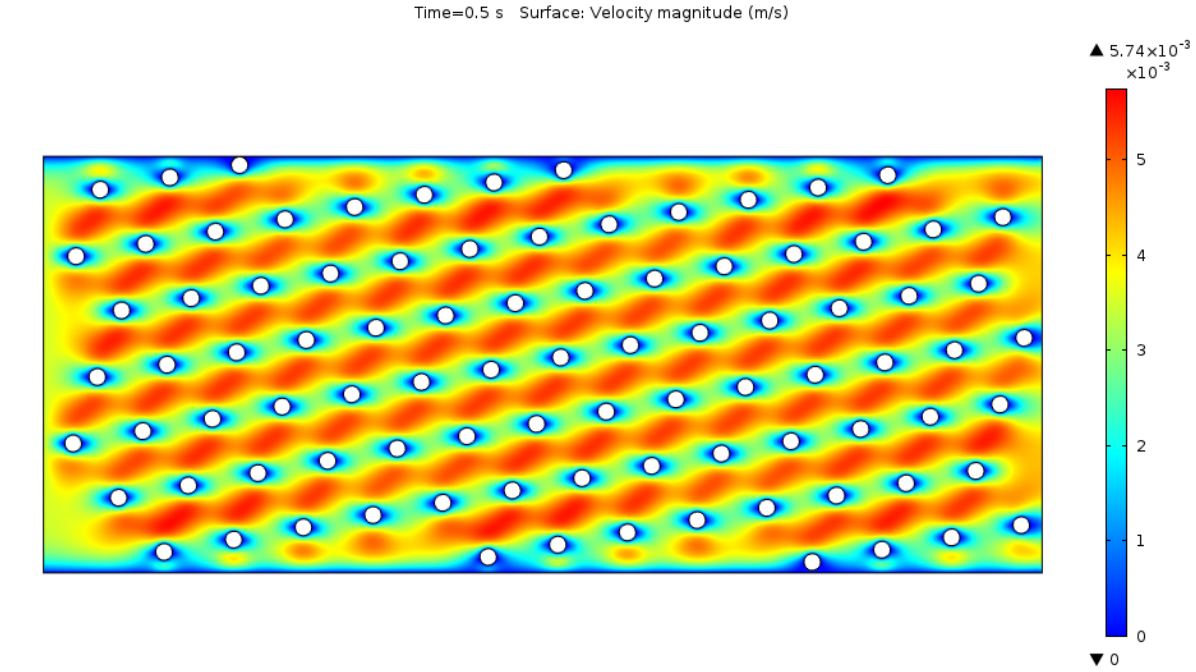


f

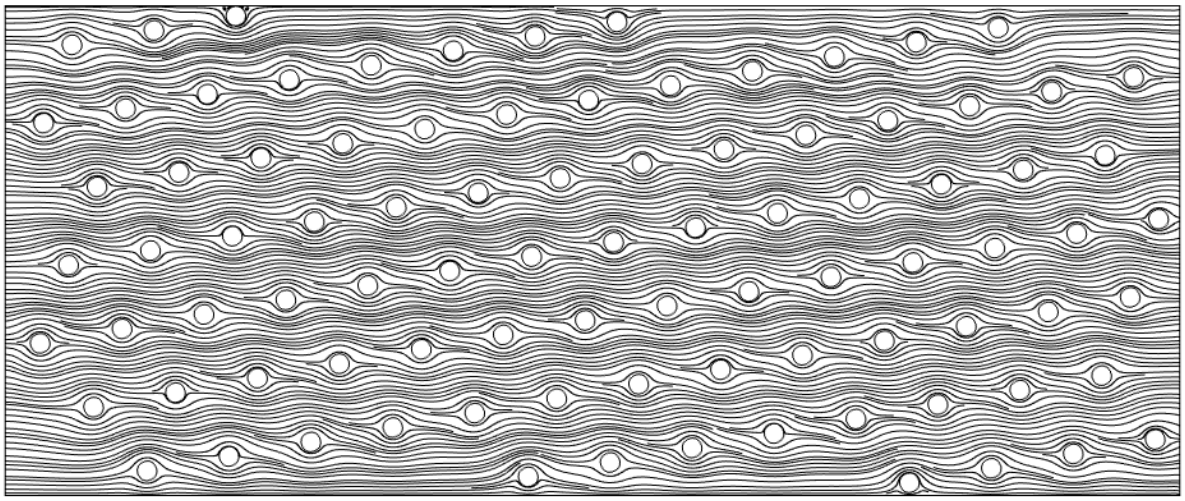
Time=0.18 s Particle trajectories



g

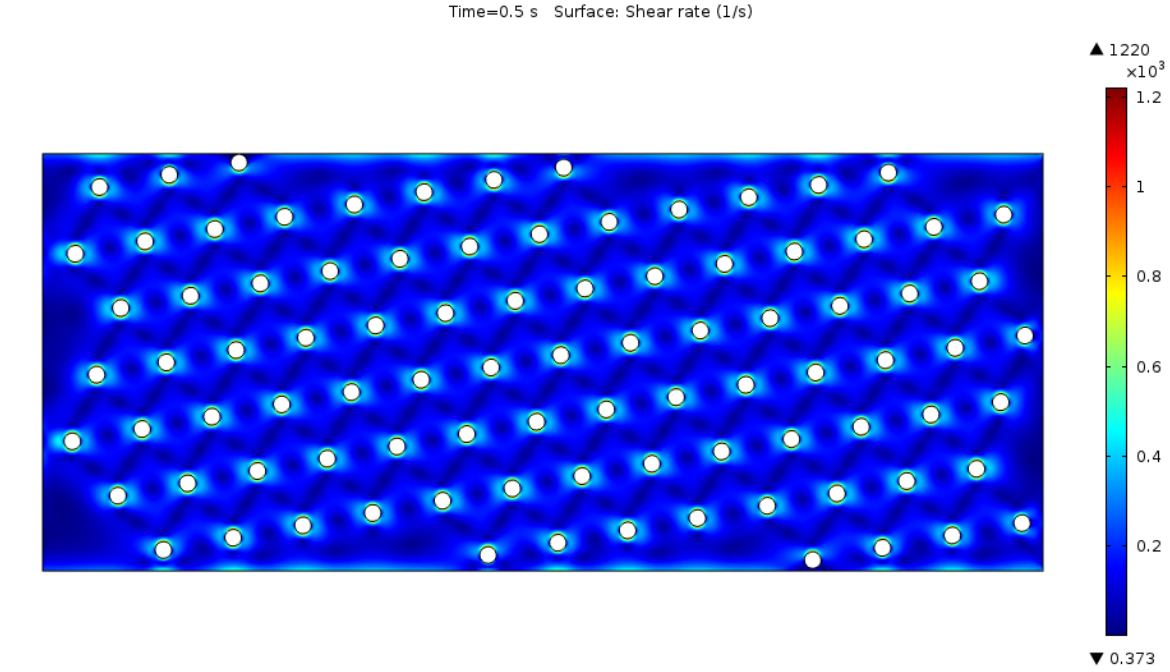

Time=0.5 s Surface: Velocity magnitude (m/s)
▲ 5.74×10^-3
×10^-3
5
4
3
2
1
0
▼ 0

h

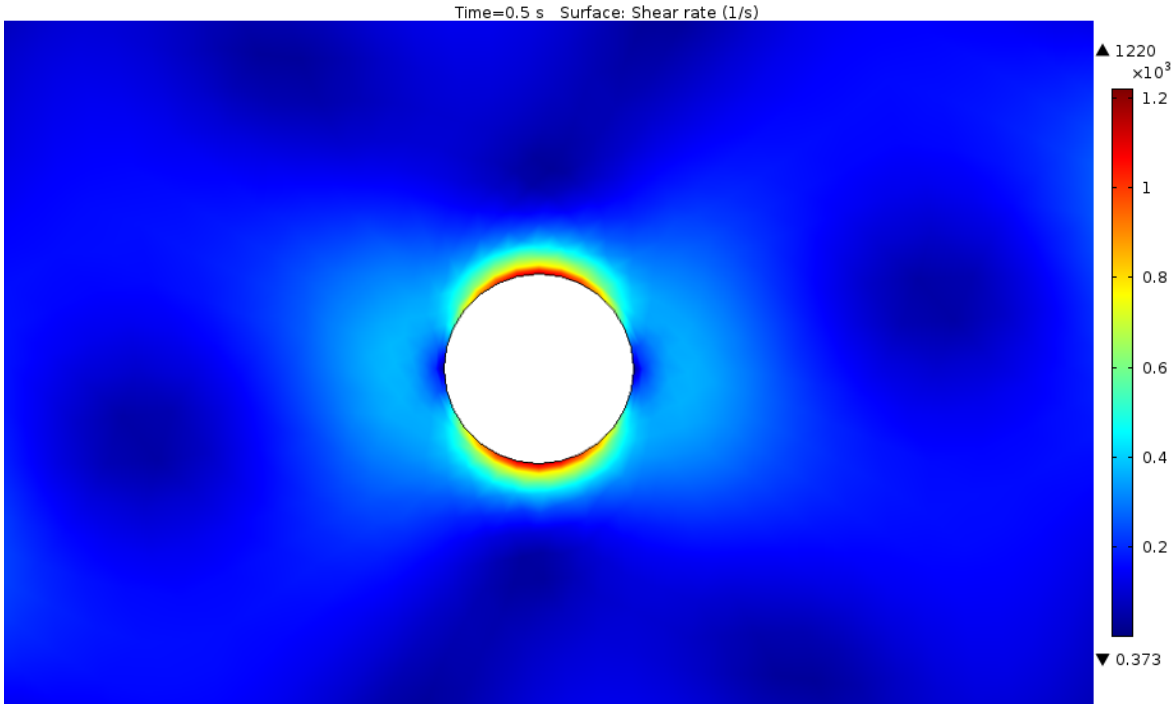

Time=0.5 s Streamline: Velocity field

3. Results Obtained at Velocity 3666.66 µm/s

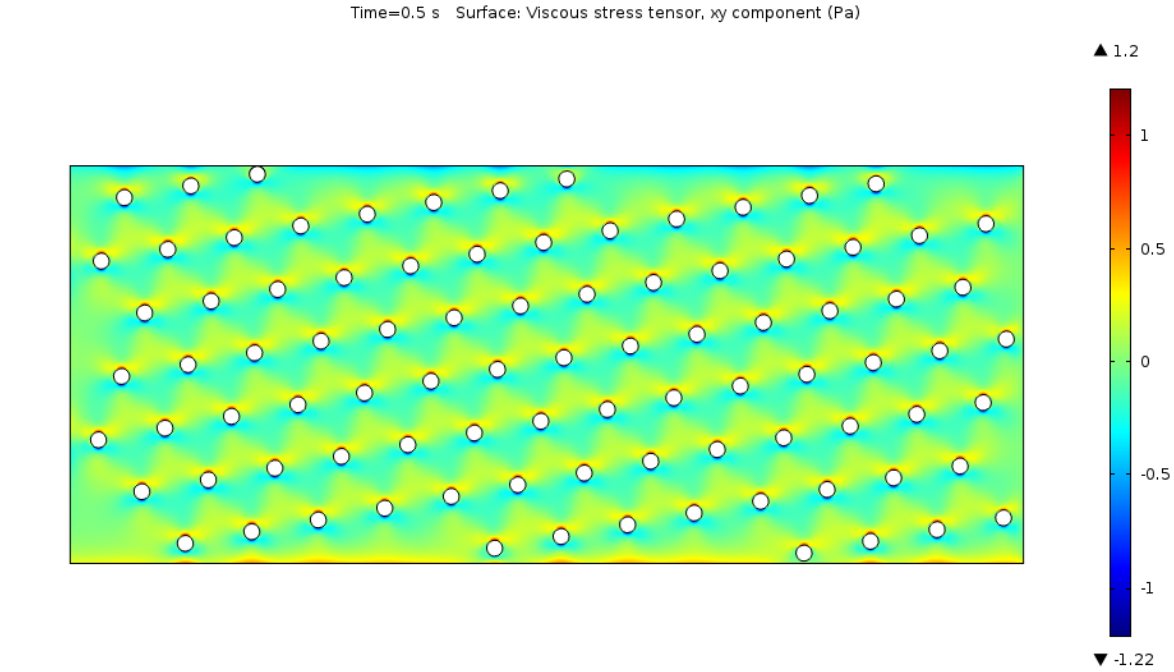
a



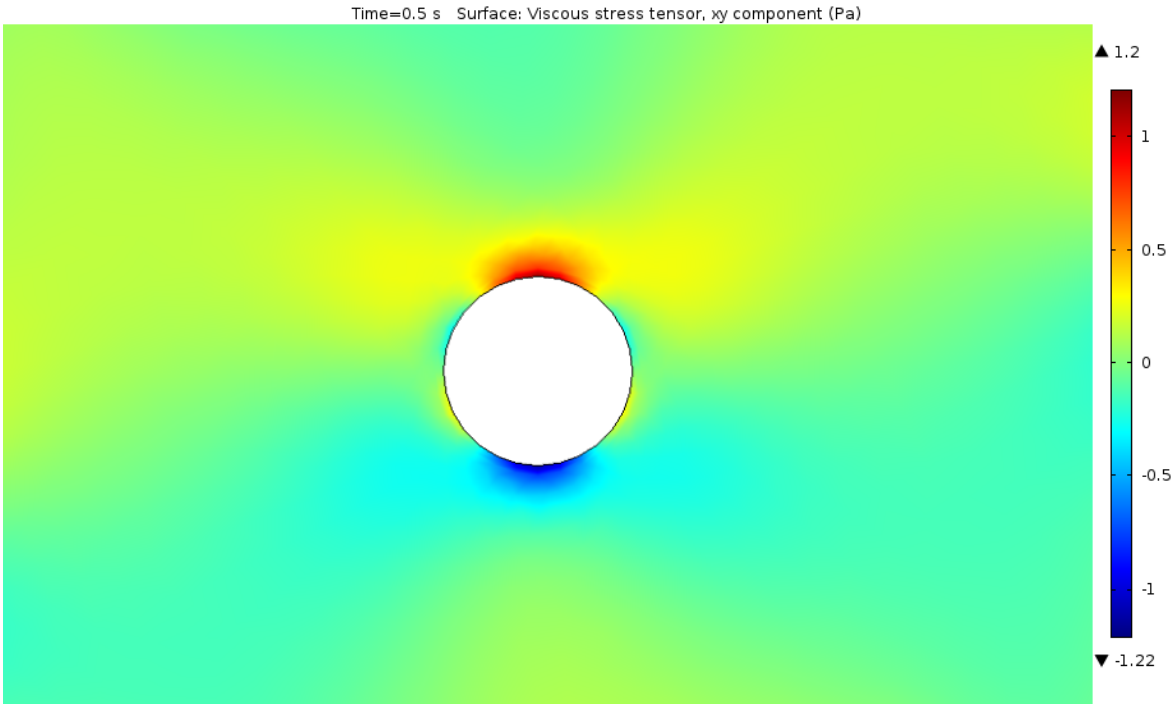
b



c

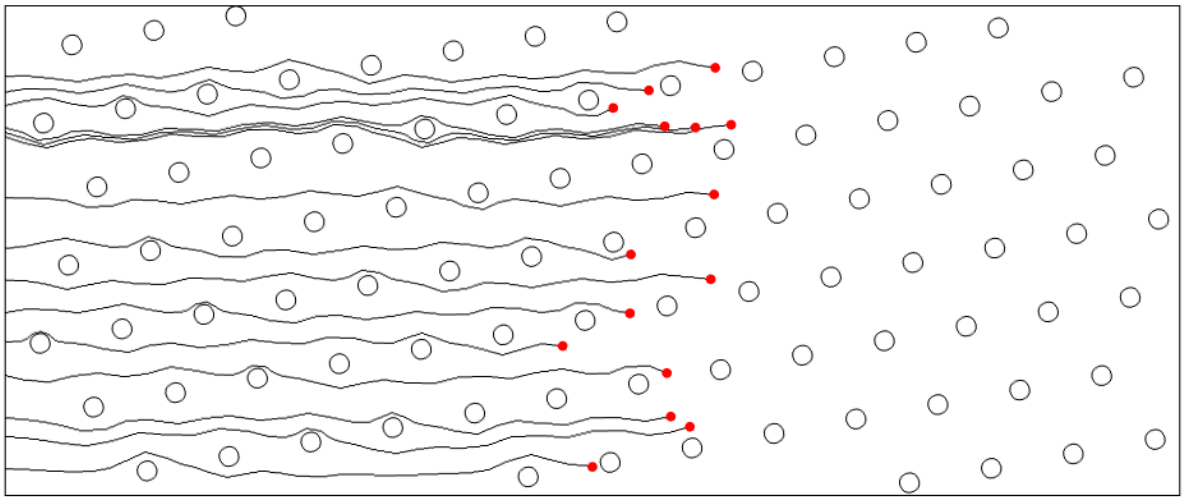

Time=0.5 s Surface: Viscous stress tensor, xy component (Pa)
▲ 1.2
1
0.5
0
-0.5
-1
▼ -1.22

d


Time=0.5 s Surface: Viscous stress tensor, xy component (Pa)
▲ 1.2
1
0.5
0
-0.5
-1
▼ -1.22

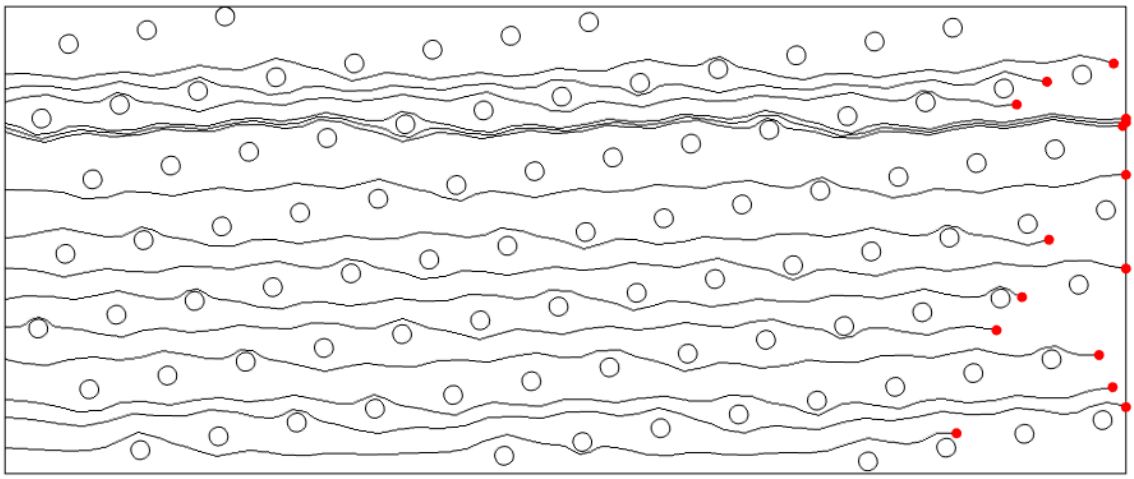
e

Time=0.16 s Particle trajectories

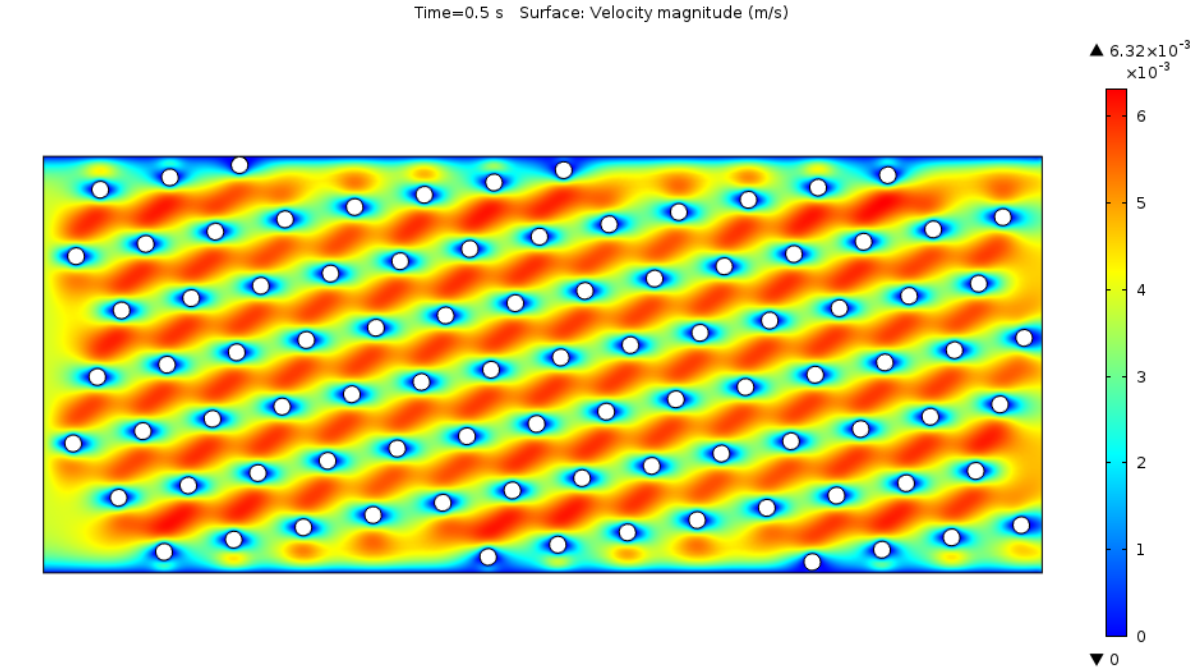


f

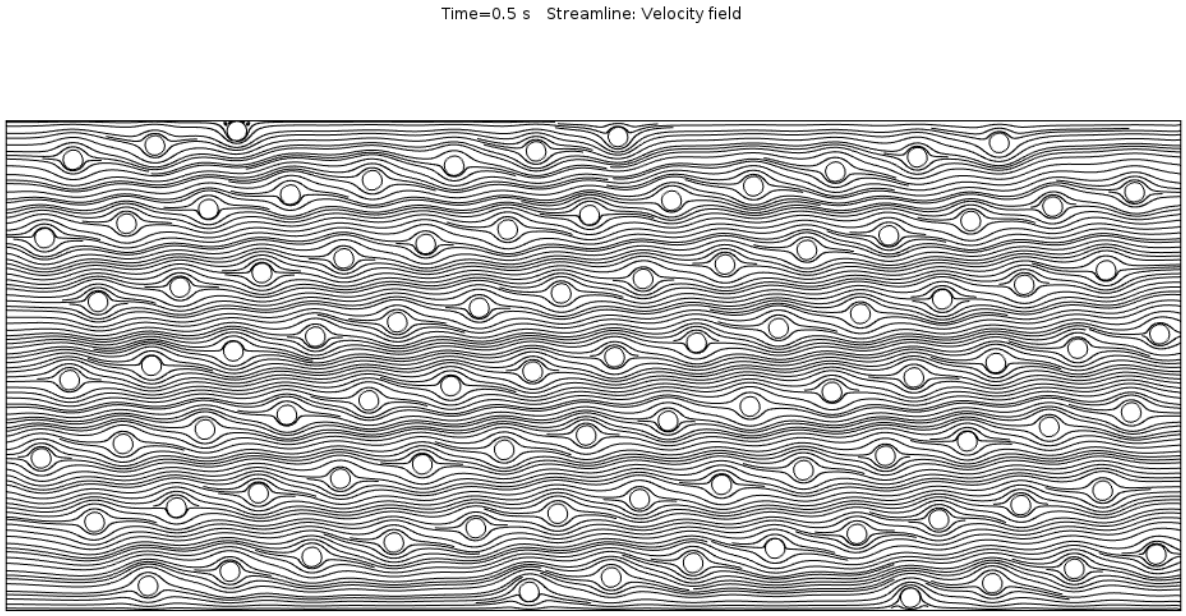
Time=0.28 s Particle trajectories



g

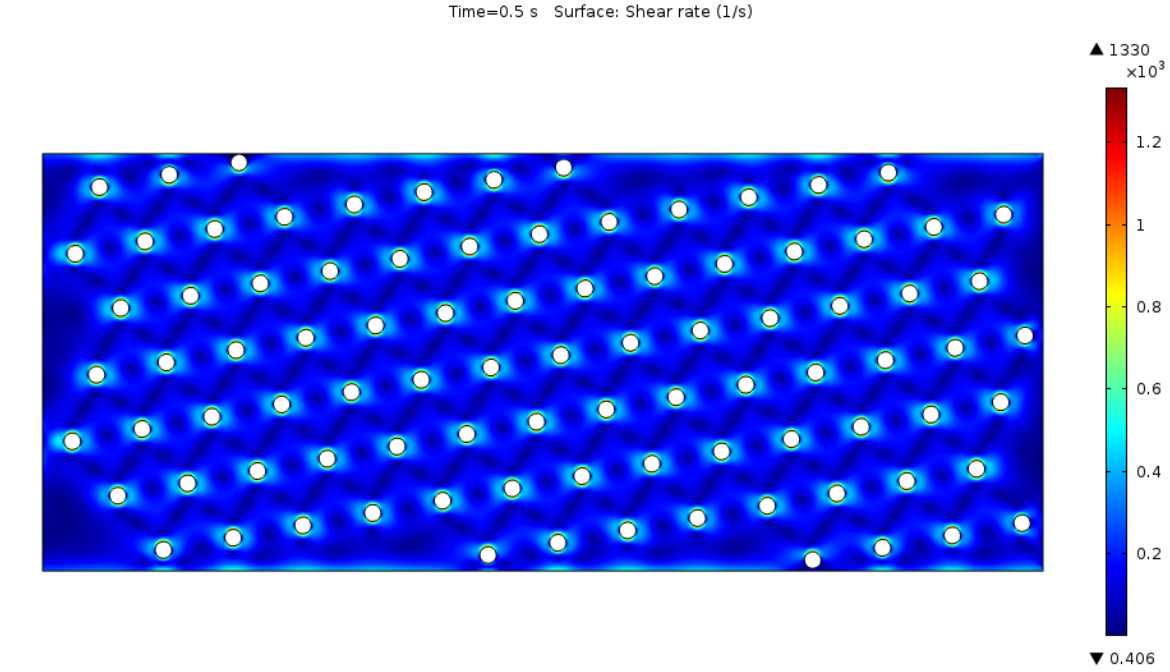

Time=0.5 s Surface: Velocity magnitude (m/s)
▲ 6.32×10^-3
×10^-3
6
5
4
3
2
1
0
▼ 0

h

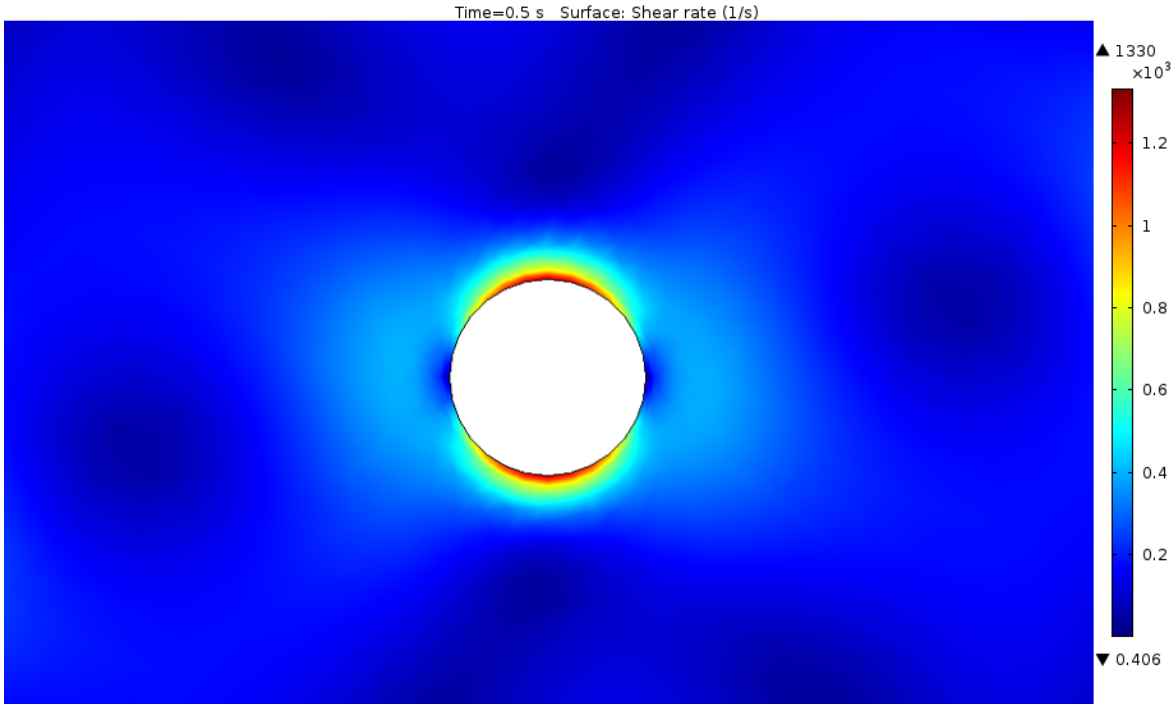

Time=0.5 s Streamline: Velocity field

4. Results Obtained at Velocity 4000 µm/s

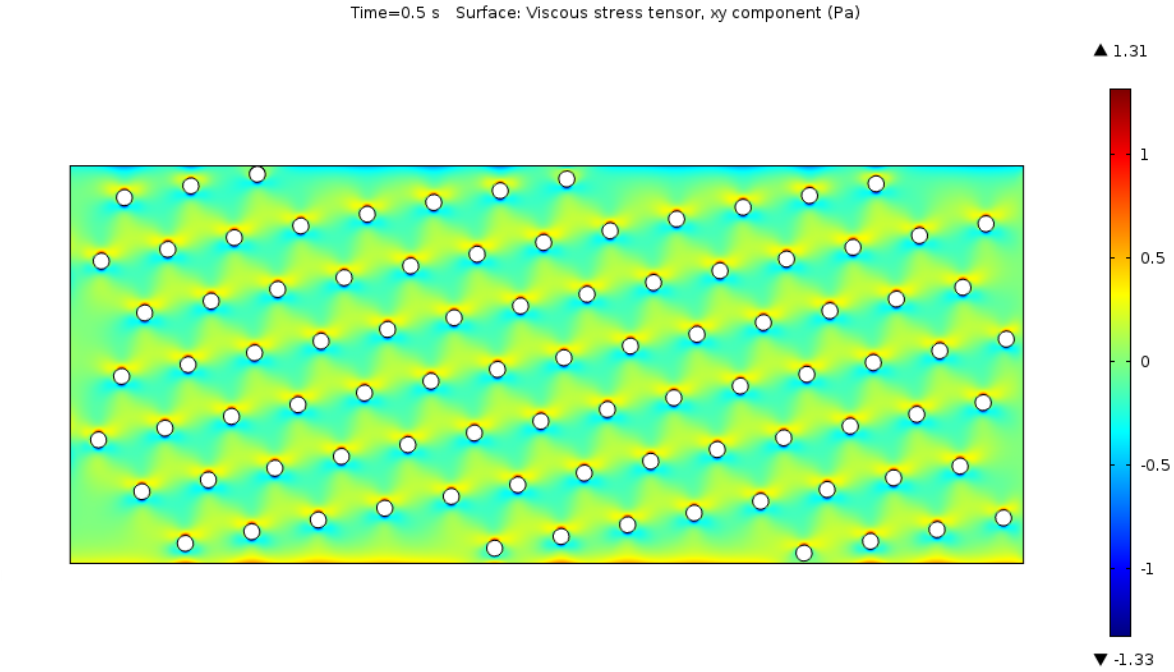
a



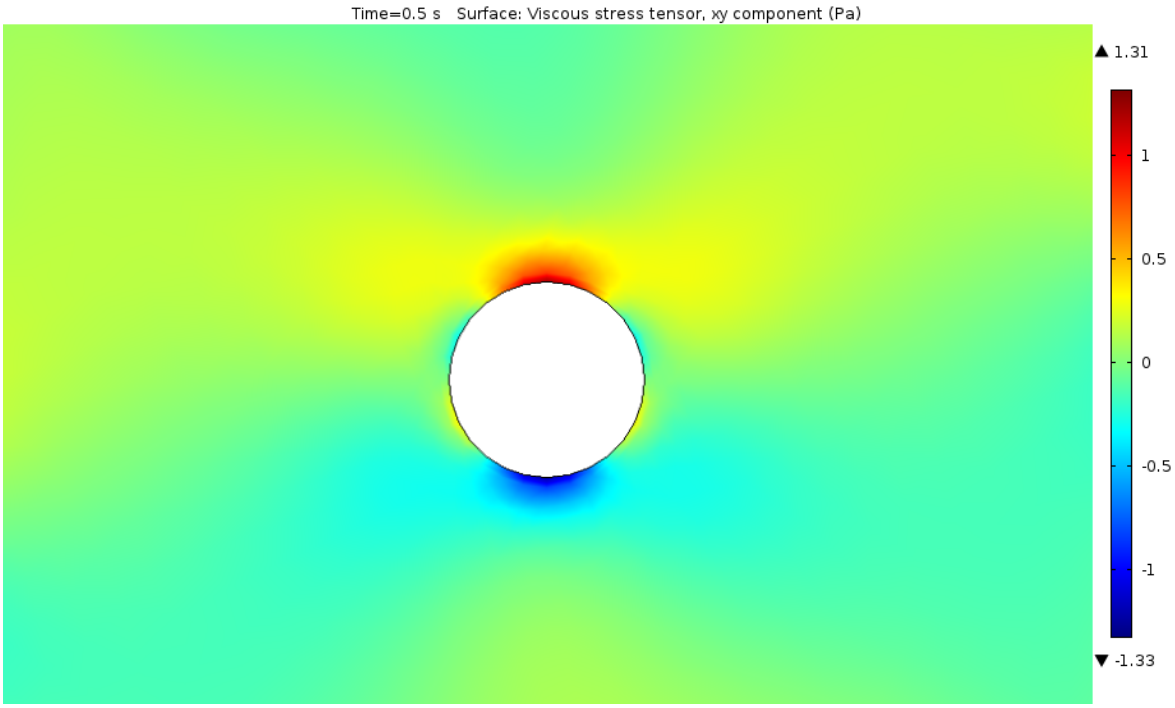
b



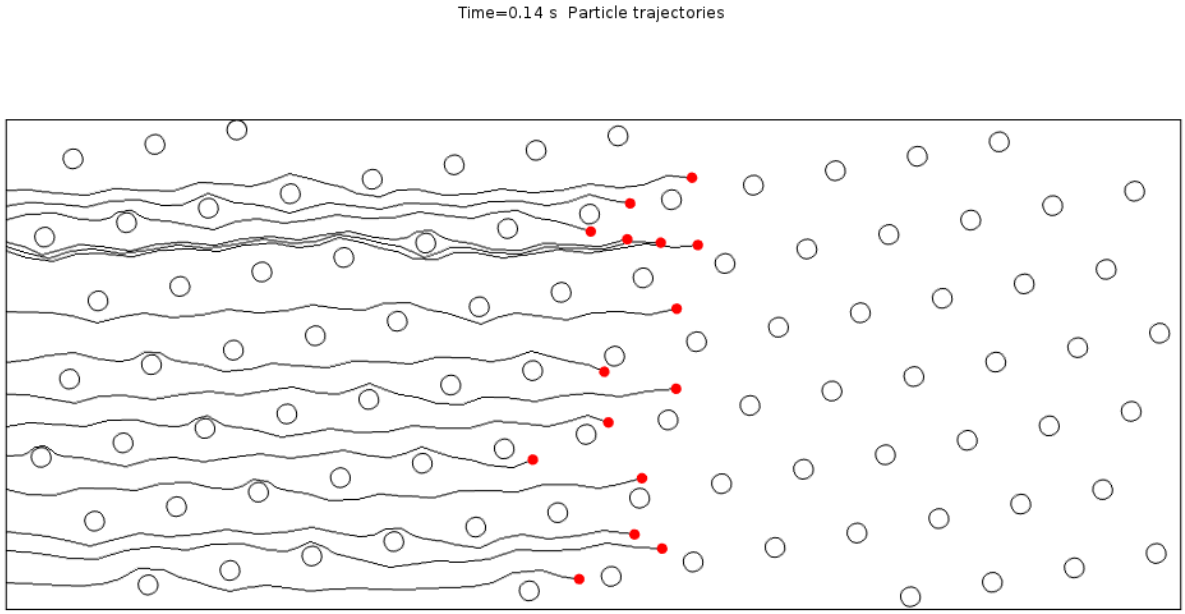
c


Time=0.5 s Surface: Viscous stress tensor, xy component (Pa)
▲ 1.31
1
0.5
0
-0.5
-1
▼ -1.33

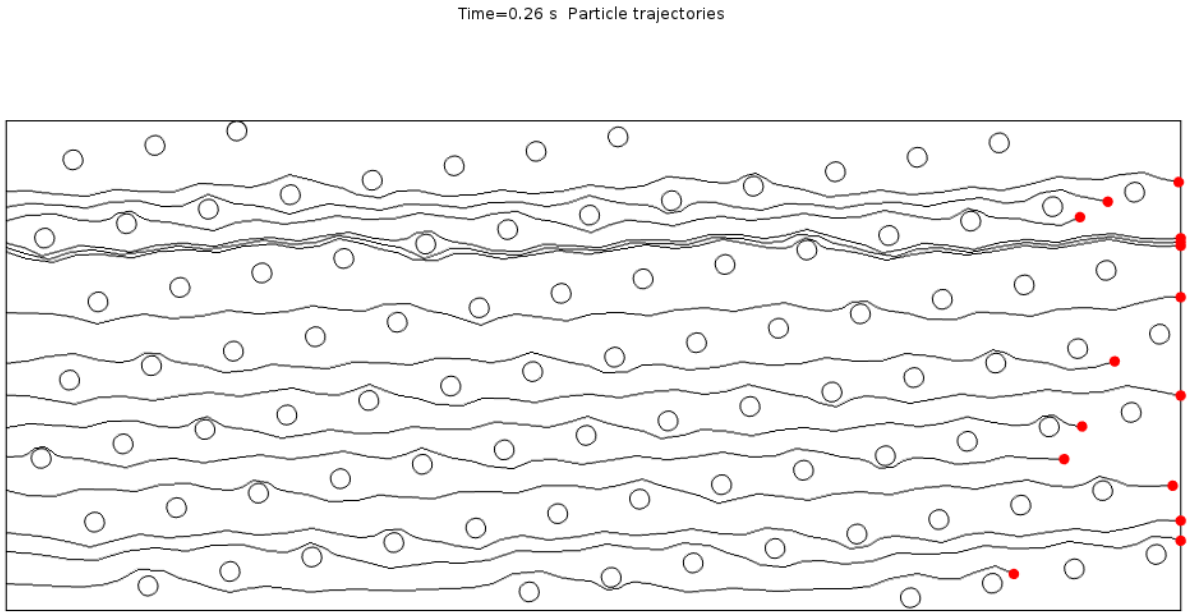
d


Time=0.5 s Surface: Viscous stress tensor, xy component (Pa)
▲ 1.31
1
0.5
0
-0.5
-1
▼ -1.33

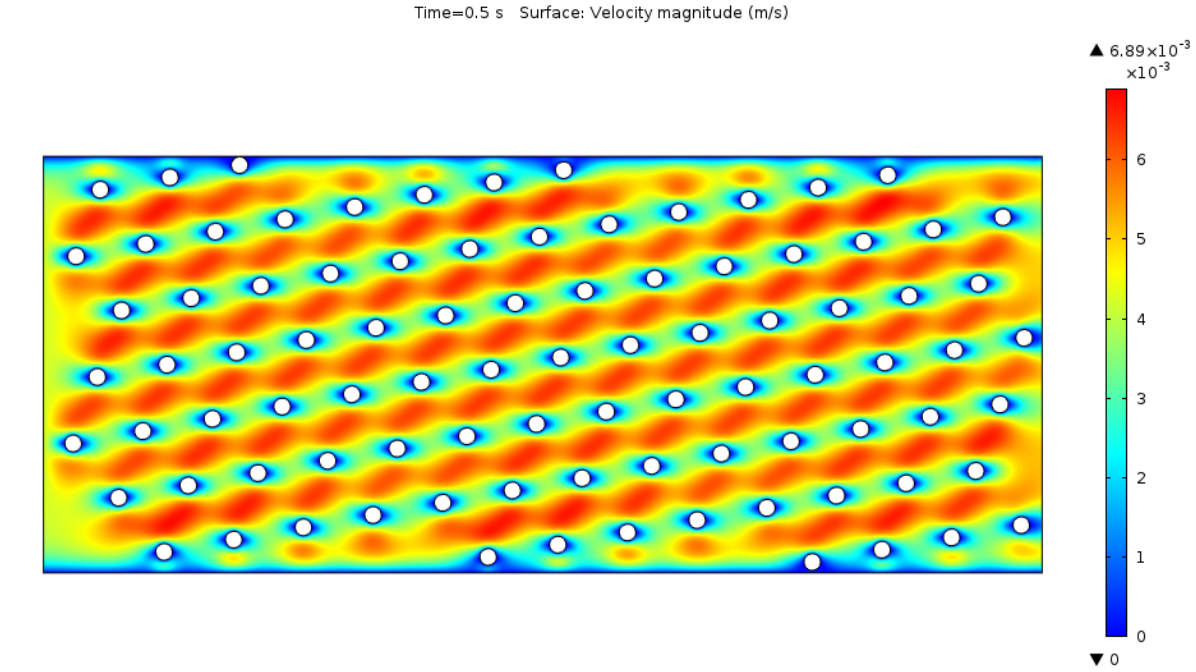
e


Time=0.14 s Particle trajectories

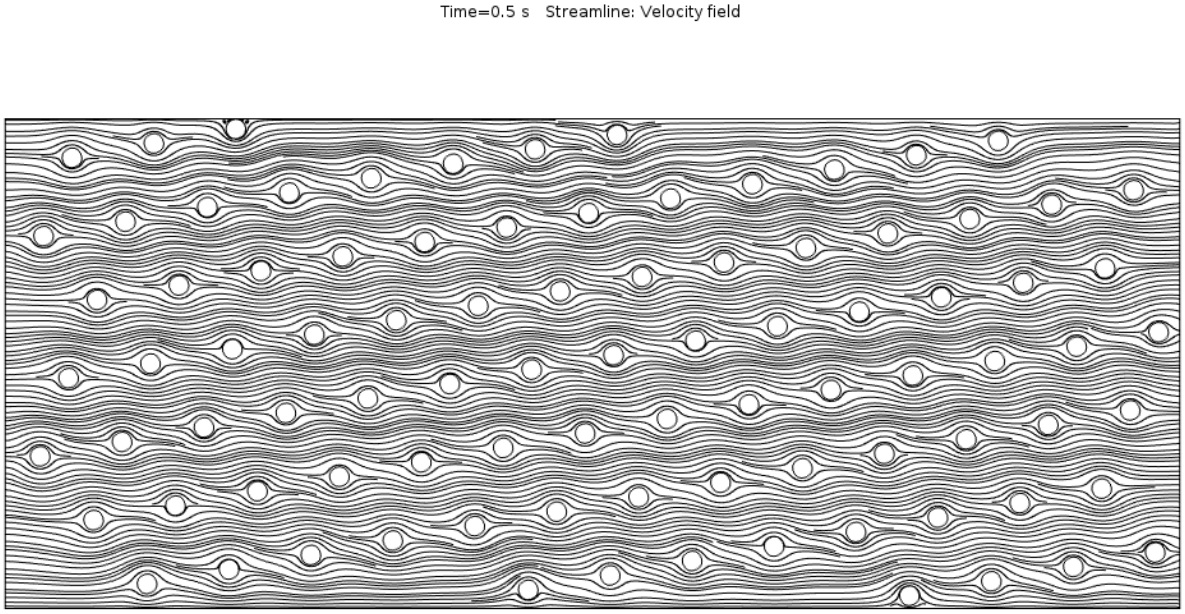
f


Time=0.26 s Particle trajectories

g

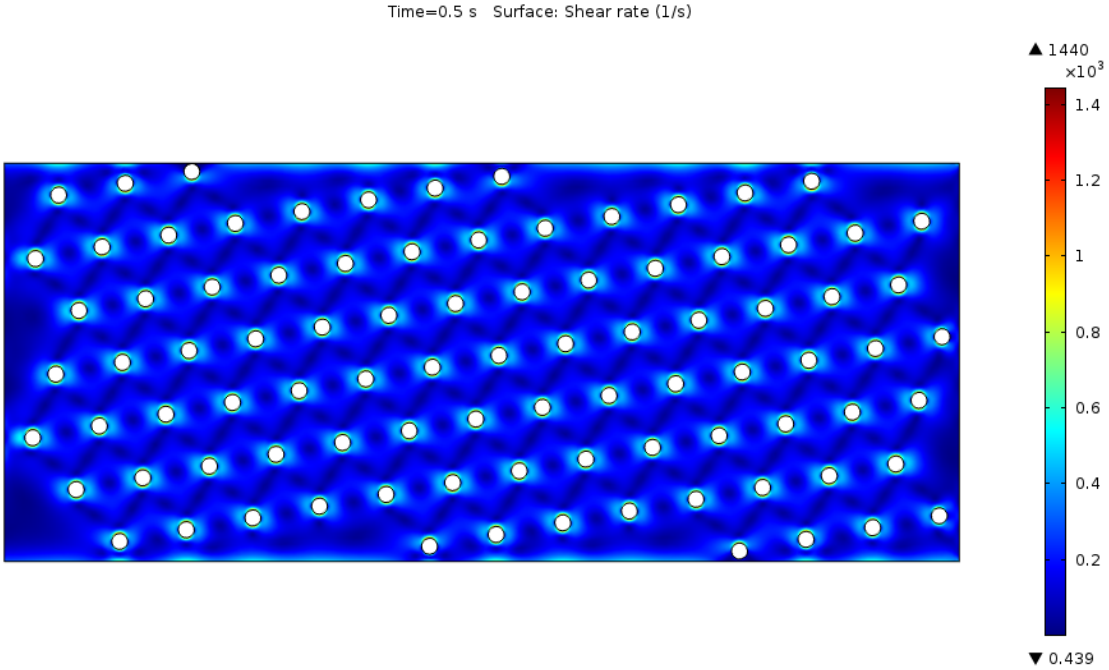

Time=0.5 s Surface: Velocity magnitude (m/s)
▲ 6.89×10^-3
×10^-3
6
5
4
3
2
1
0
▼ 0

h

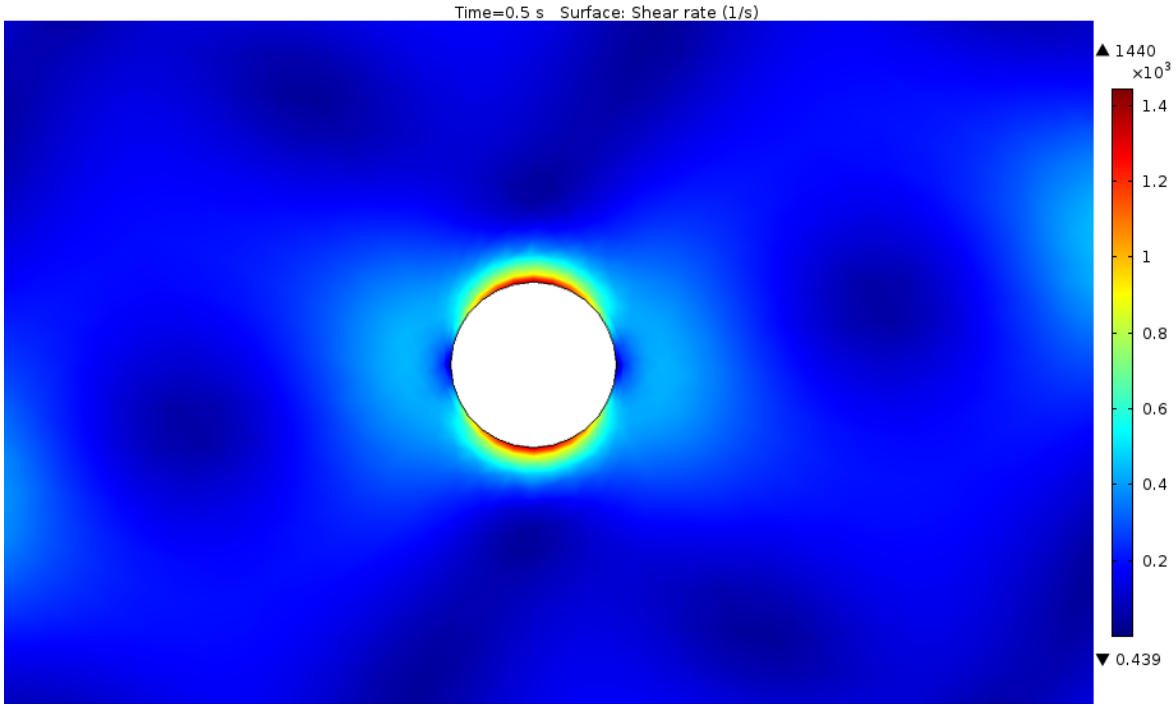

Time=0.5 s Streamline: Velocity field

5. Results Obtained at Velocity 4333.33 µm/s

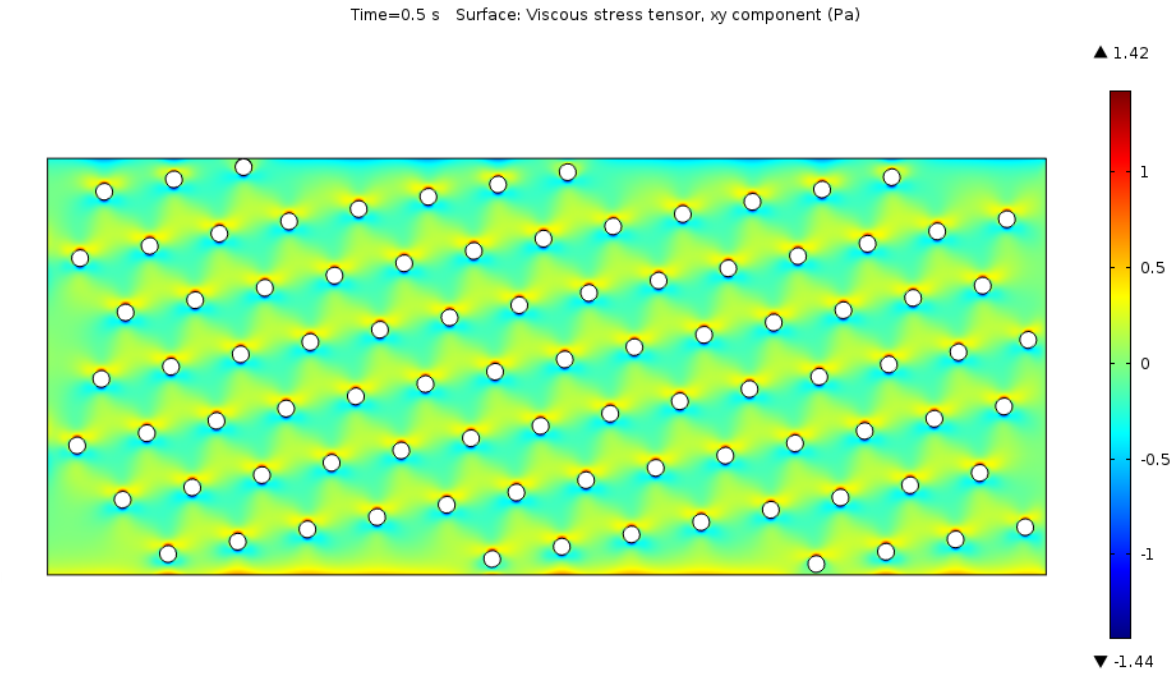
a



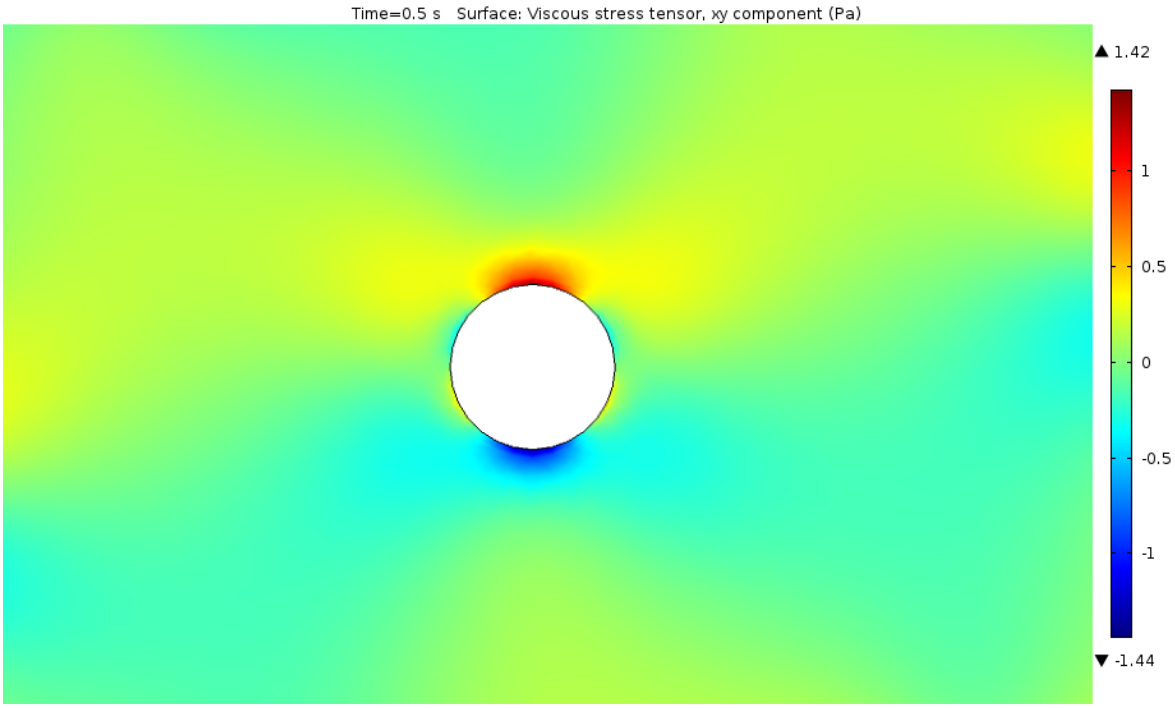
b



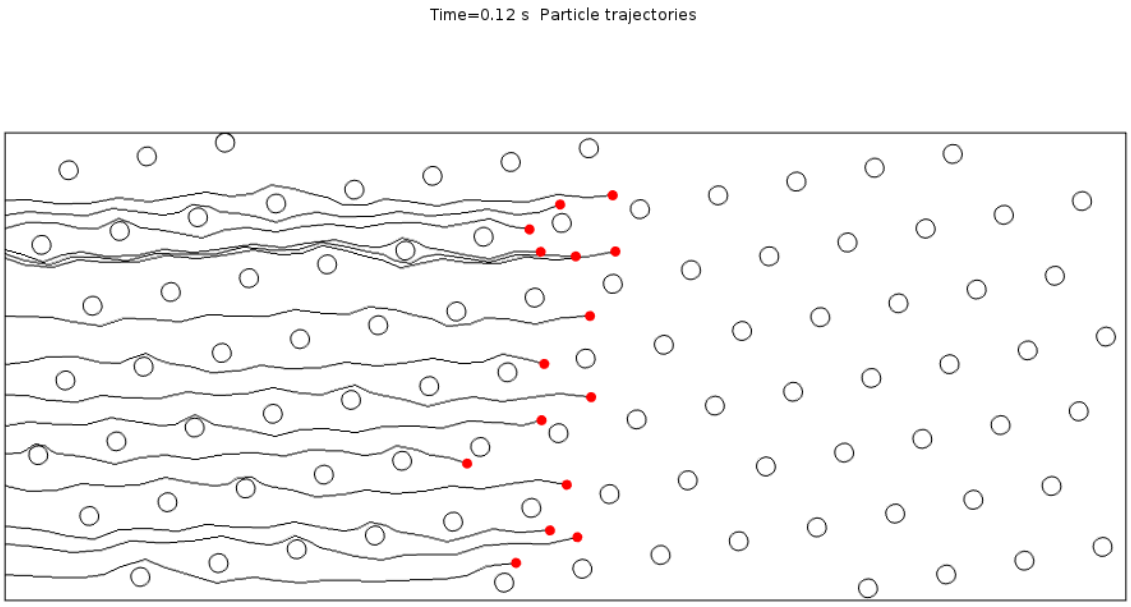
c


Time=0.5 s Surface: Viscous stress tensor, xy component (Pa)
▲ 1.42
1
0.5
0
-0.5
-1
▼ -1.44

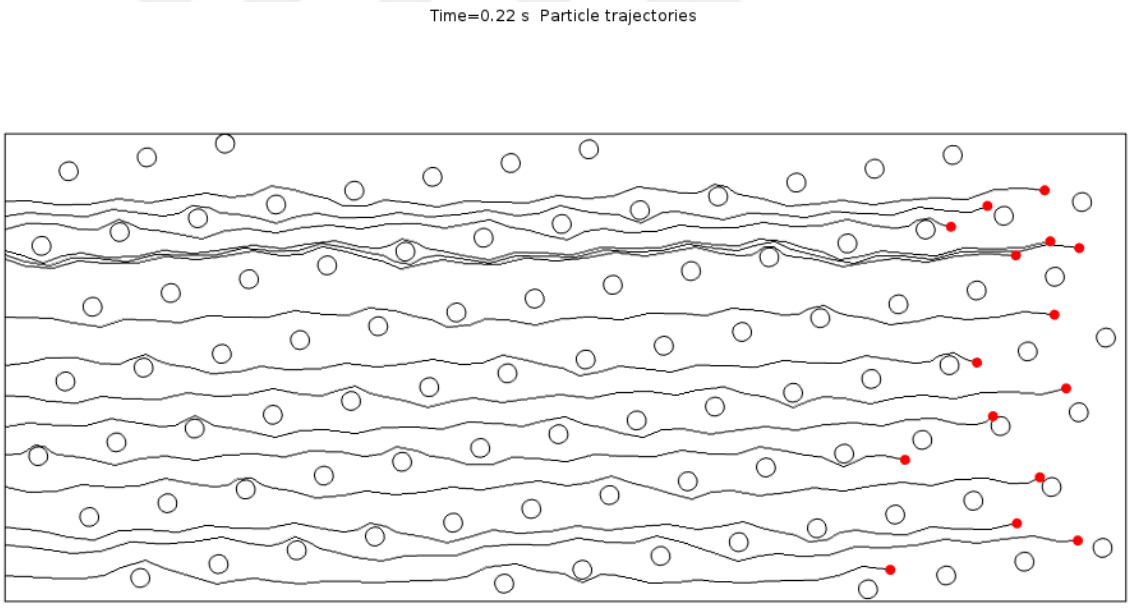
d


Time=0.5 s Surface: Viscous stress tensor, xy component (Pa)
▲ 1.42
1
0.5
0
-0.5
-1
▼ -1.44

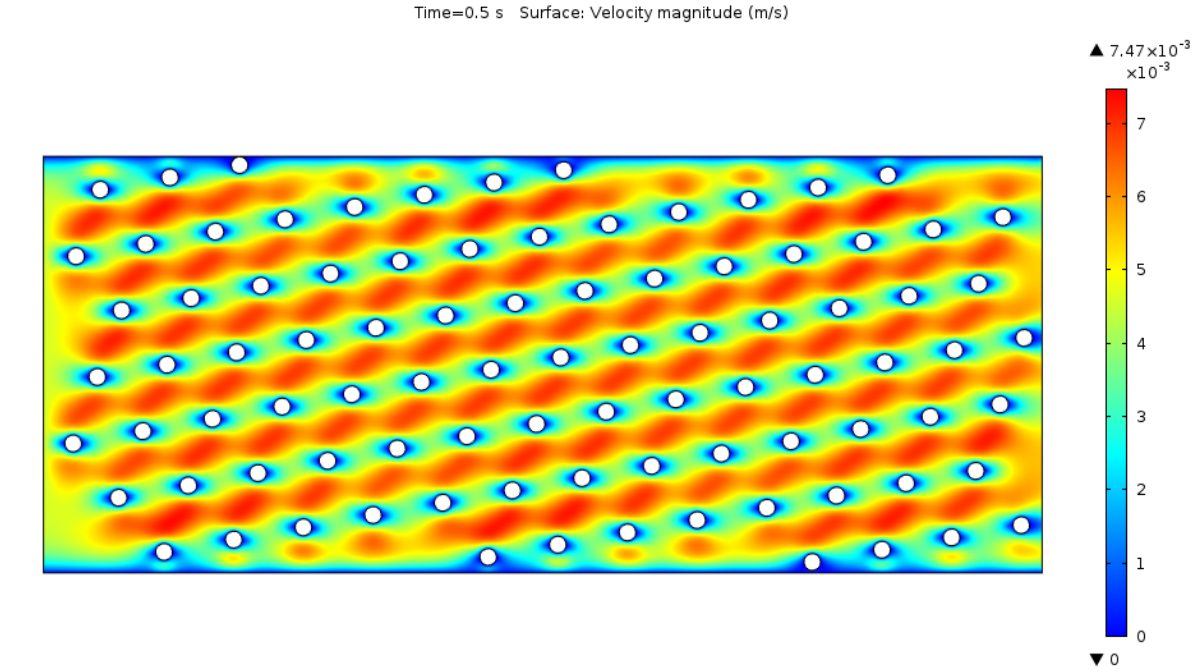
e


Time=0.12 s Particle trajectories

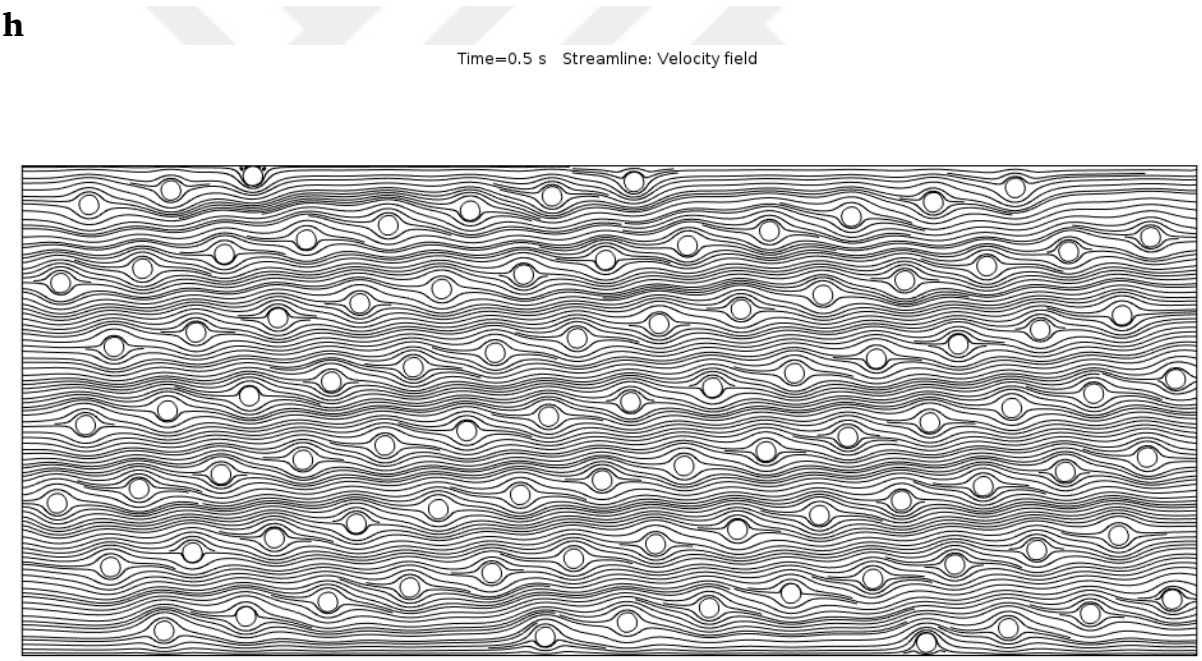
f


Time=0.22 s Particle trajectories

g

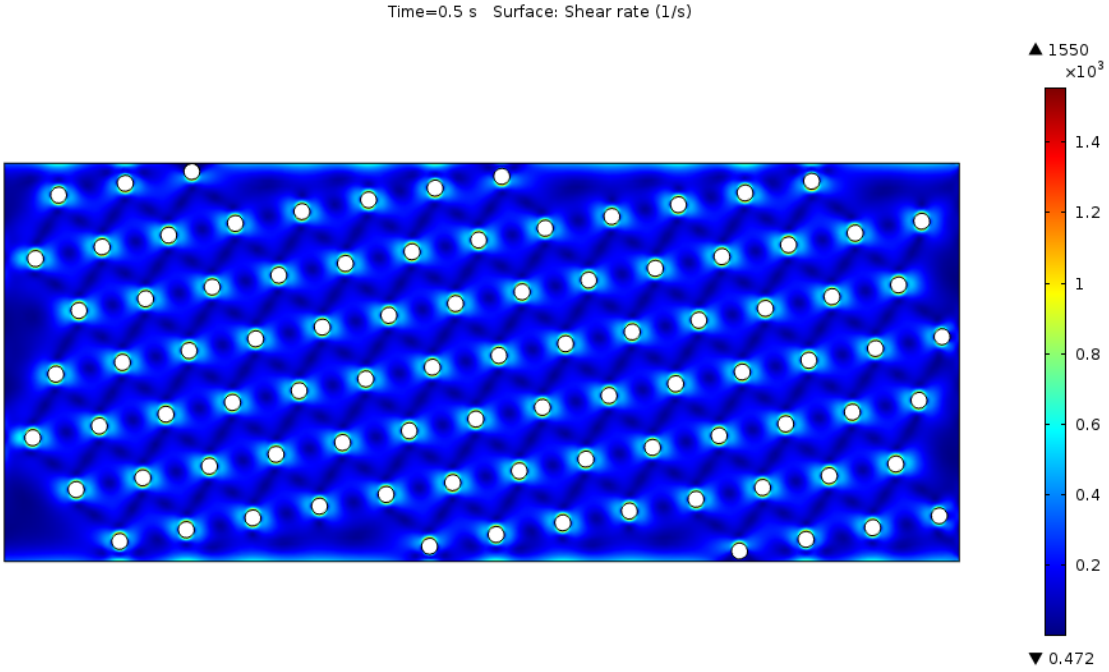

Time=0.5 s Surface: Velocity magnitude (m/s)
▲ 7.47×10^-3
×10^-3
7
6
5
4
3
2
1
0
▼ 0

h

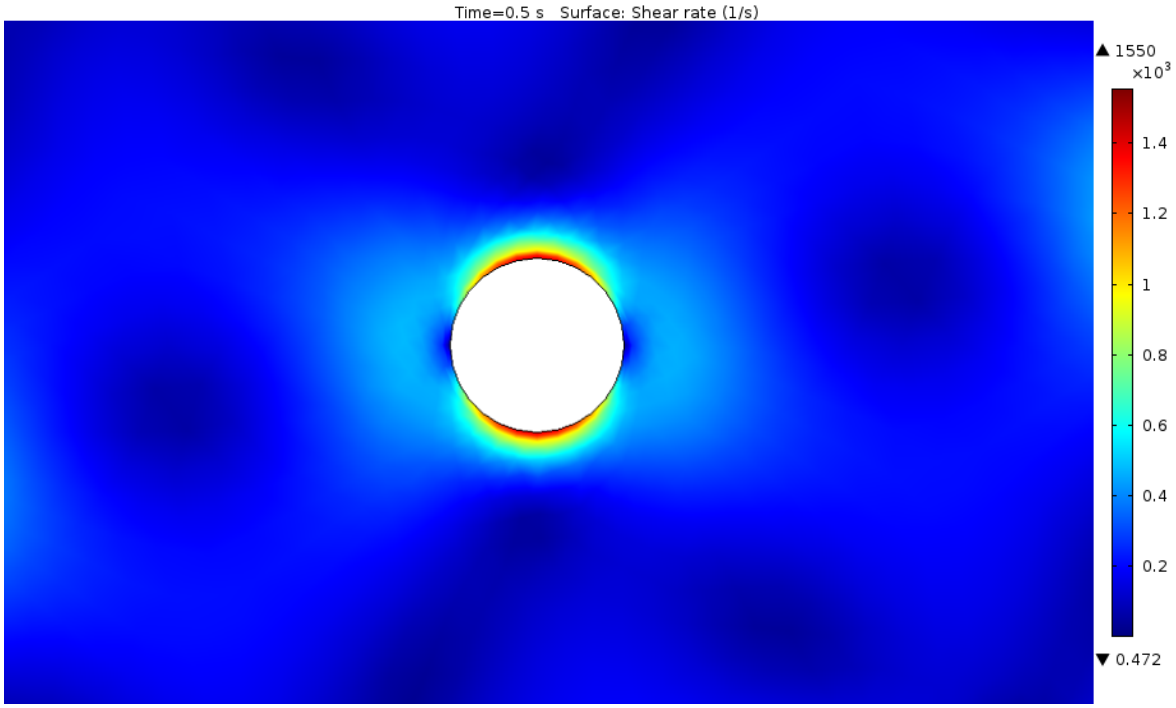

Time=0.5 s Streamline: Velocity field

6. Results Obtained at Velocity 4666.66 µm/s

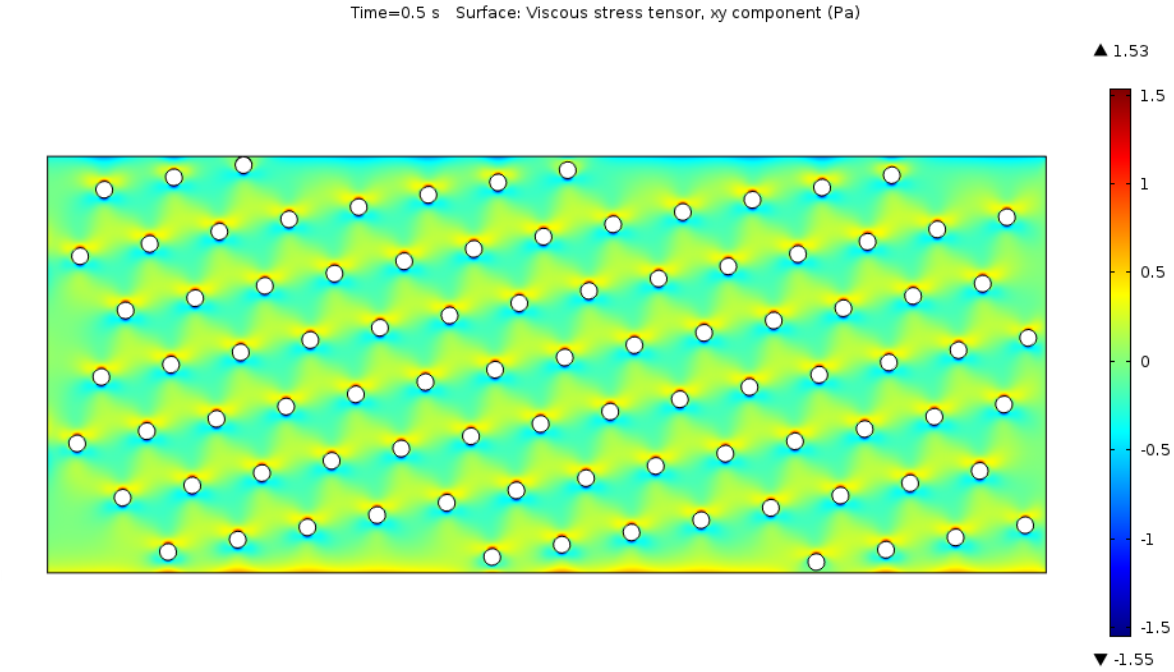
a



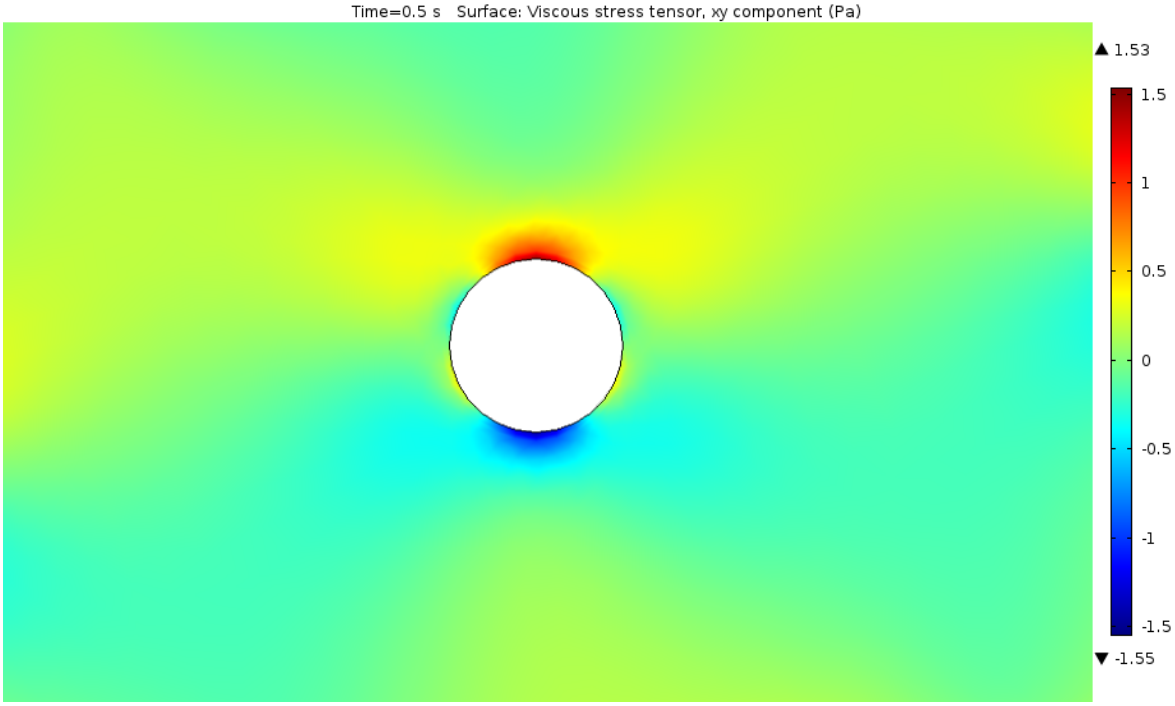
b



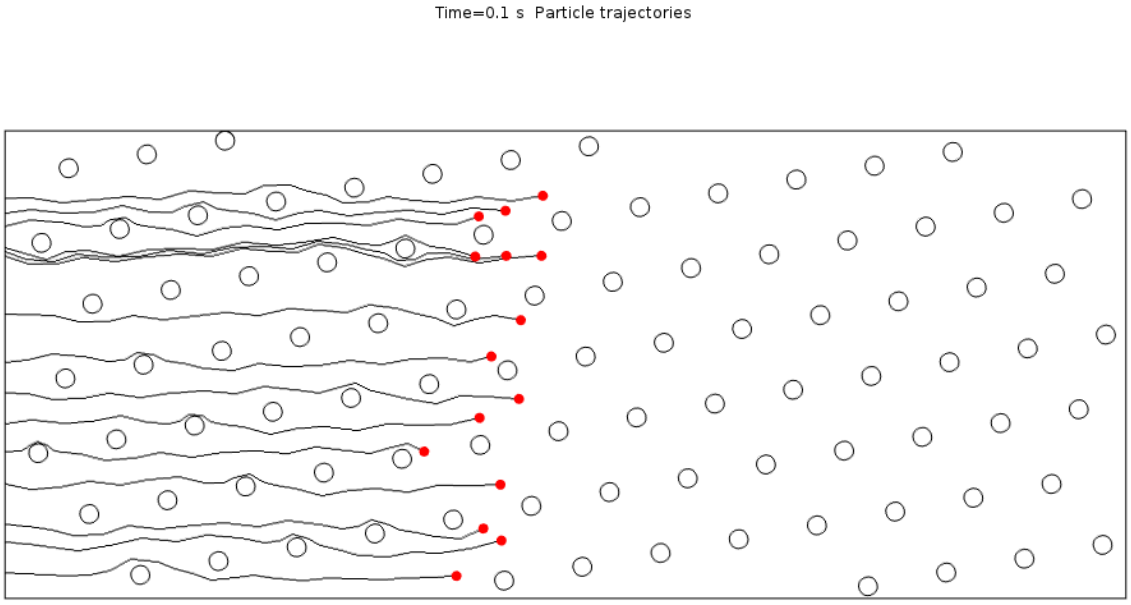
c


Time=0.5 s Surface: Viscous stress tensor, xy component (Pa)
▲ 1.53
1.5
1
0.5
0
-0.5
-1
-1.5
▼ -1.55

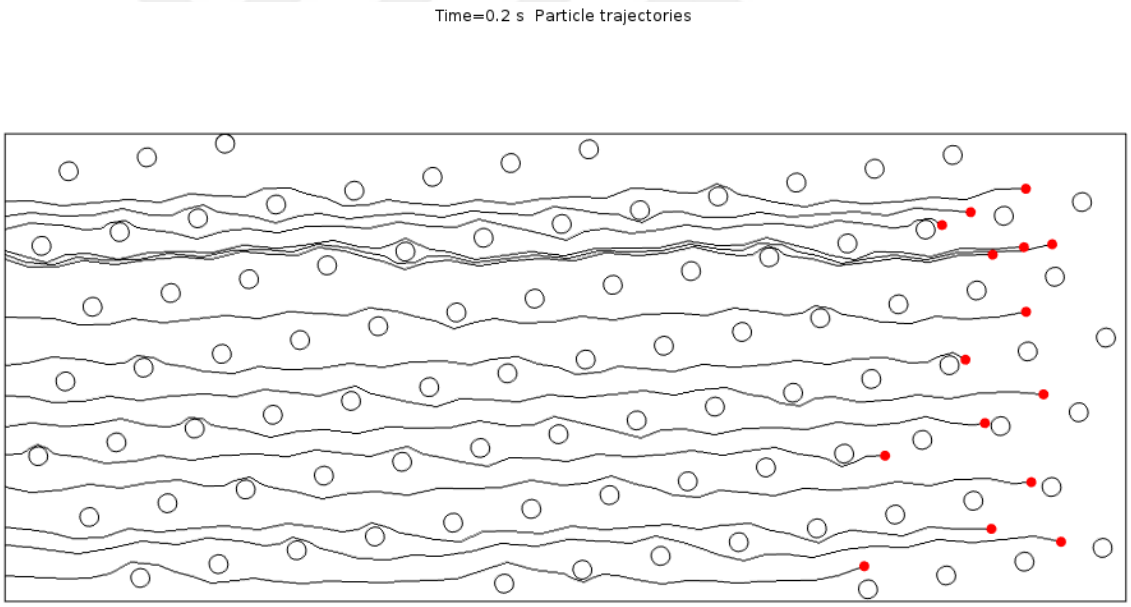
d


Time=0.5 s Surface: Viscous stress tensor, xy component (Pa)
▲ 1.53
1.5
1
0.5
0
-0.5
-1
-1.5
▼ -1.55

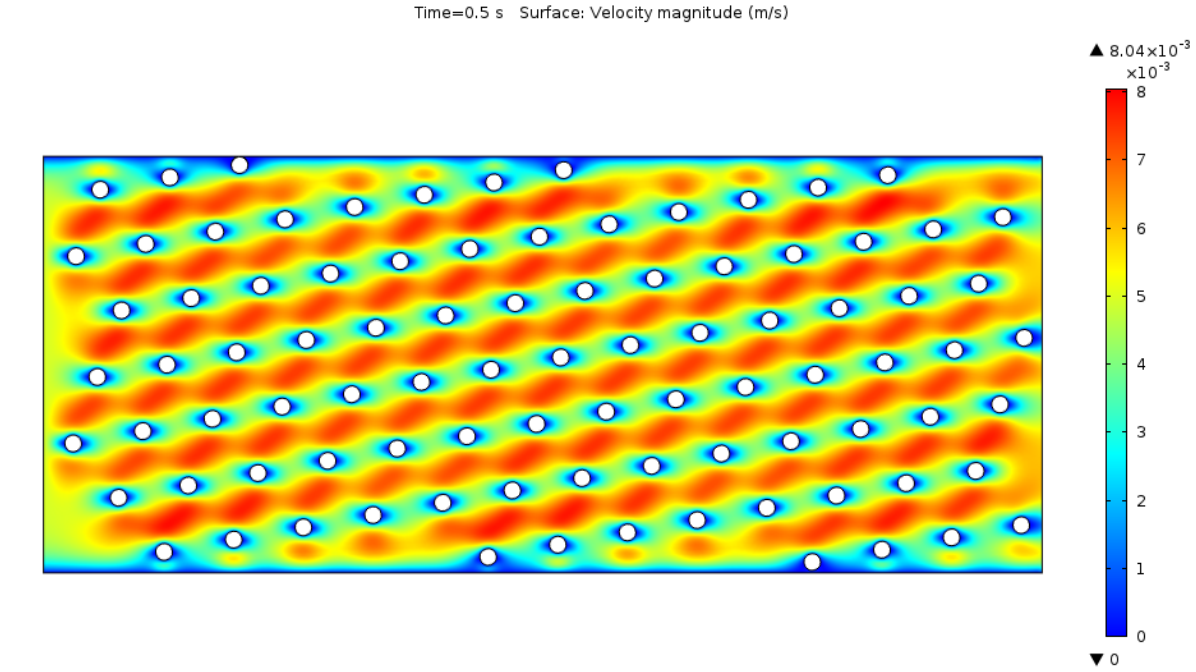
e


Time=0.1 s Particle trajectories

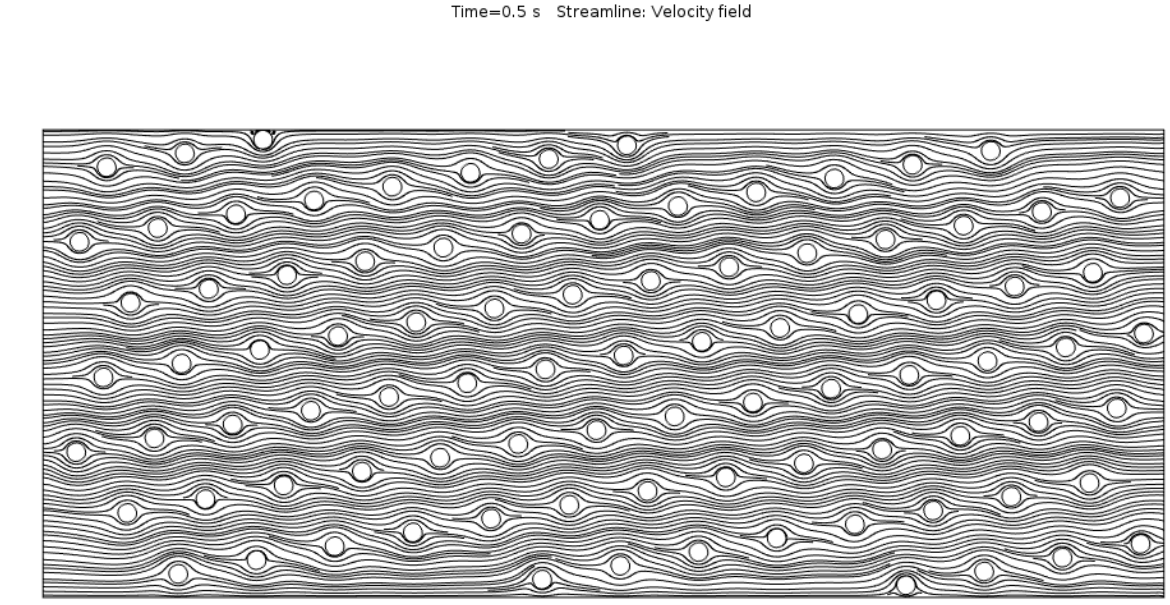
f


Time=0.2 s Particle trajectories

g

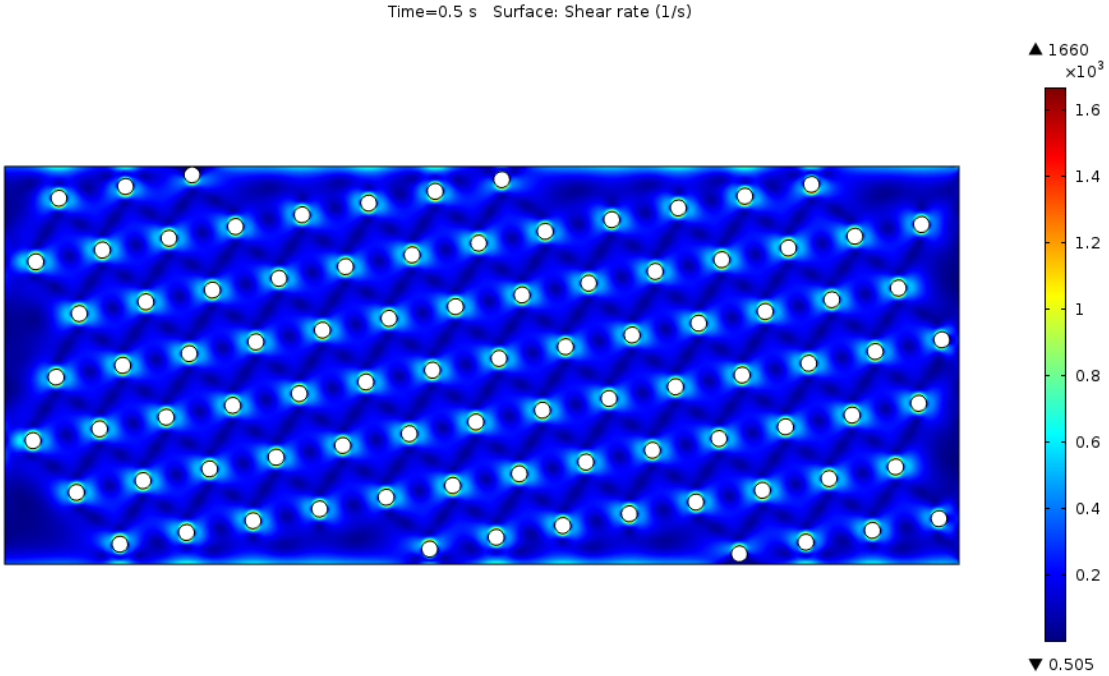

Time=0.5 s Surface: Velocity magnitude (m/s)
▲ 8.04×10^-3
×10^-3
8
7
6
5
4
3
2
1
0
▼ 0

h

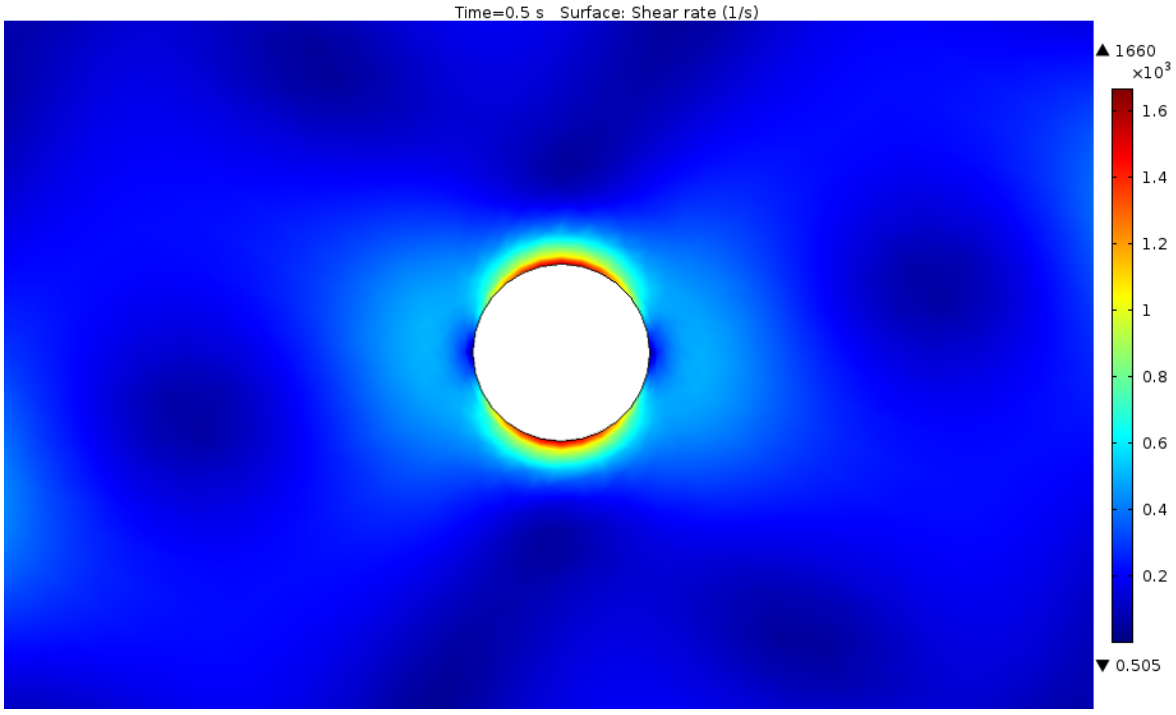

Time=0.5 s Streamline: Velocity field

7. Results Obtained at Velocity 5000 µm/s

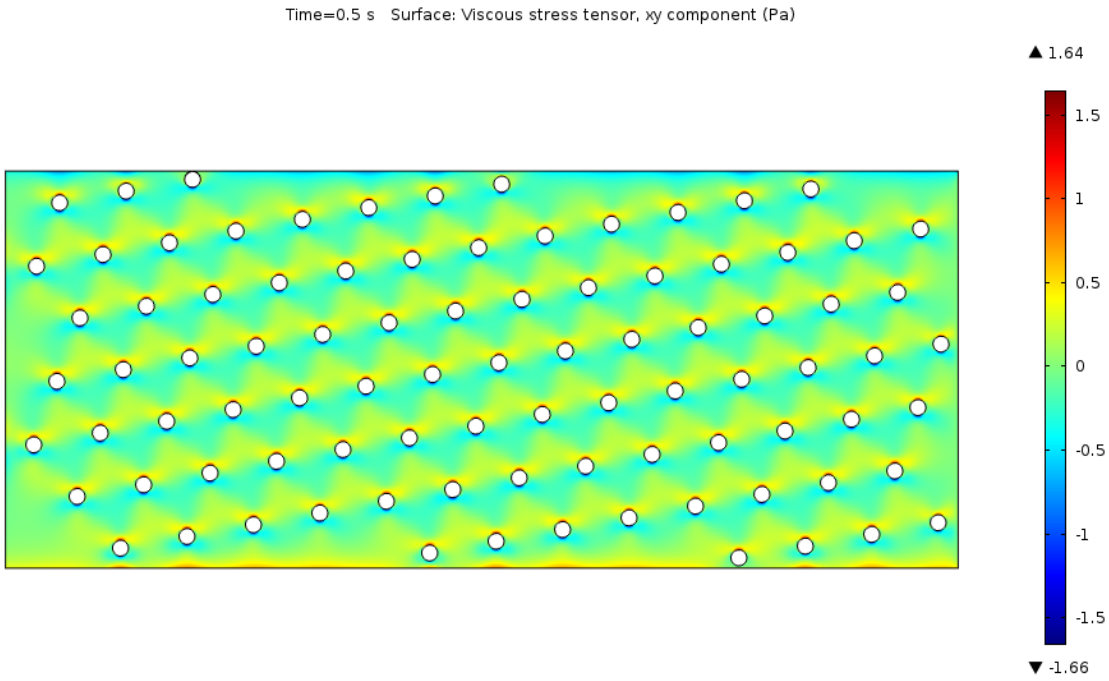
a



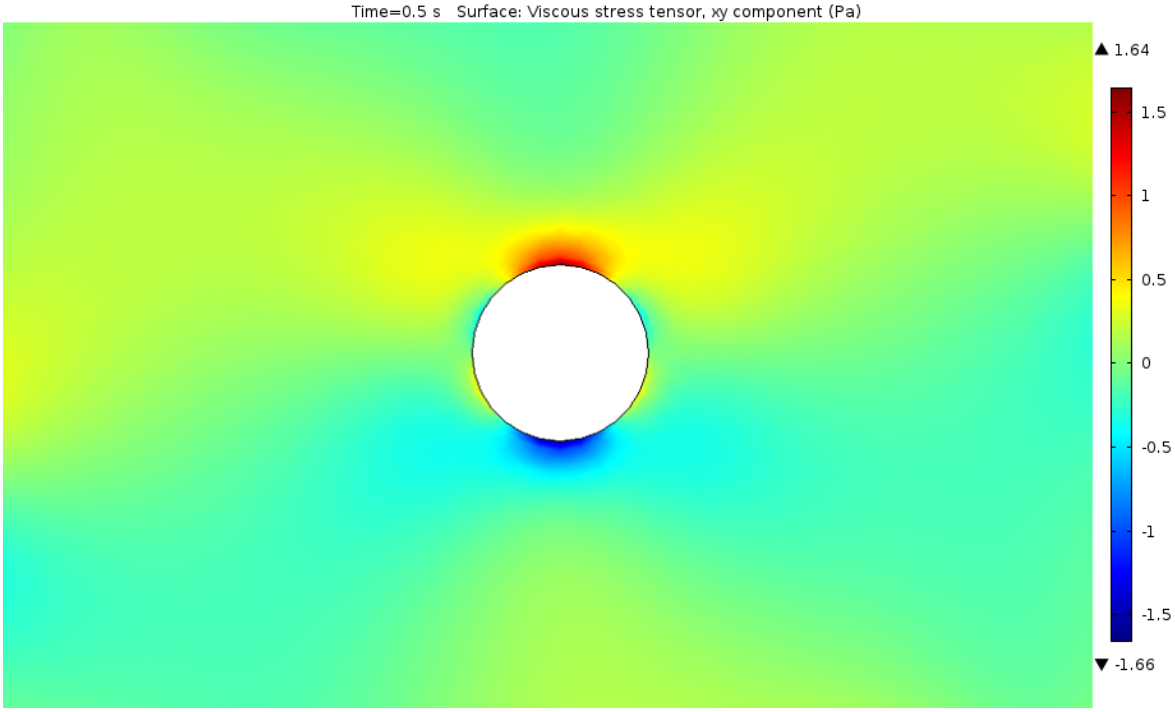
b



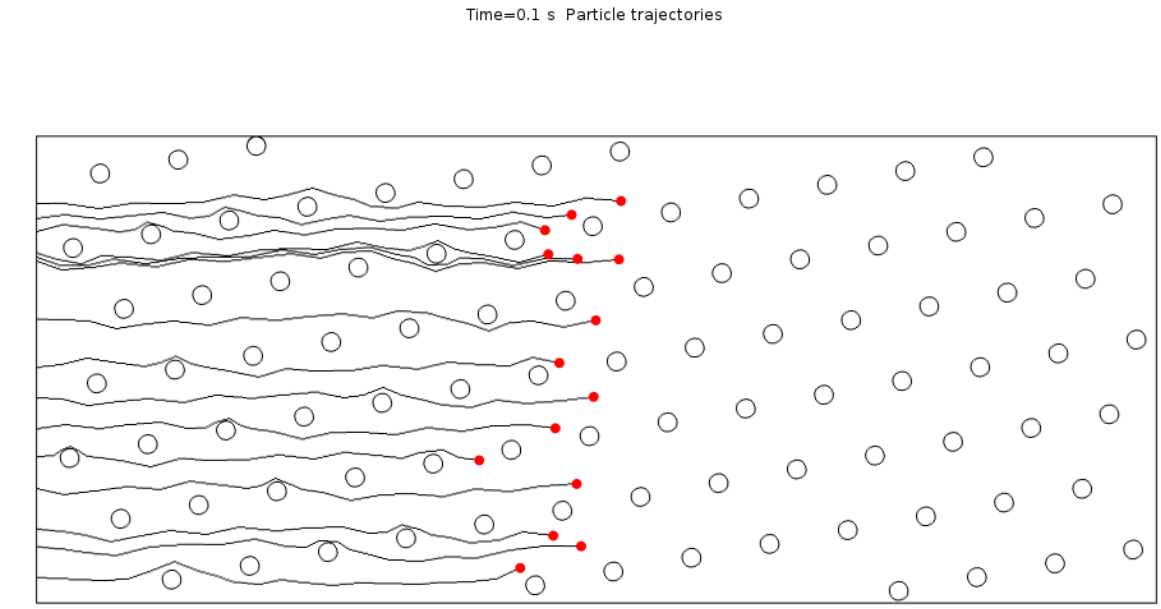
c


Time=0.5 s Surface: Viscous stress tensor, xy component (Pa)
▲ 1.64
1.5
1
0.5
0
-0.5
-1
-1.5
▼ -1.66

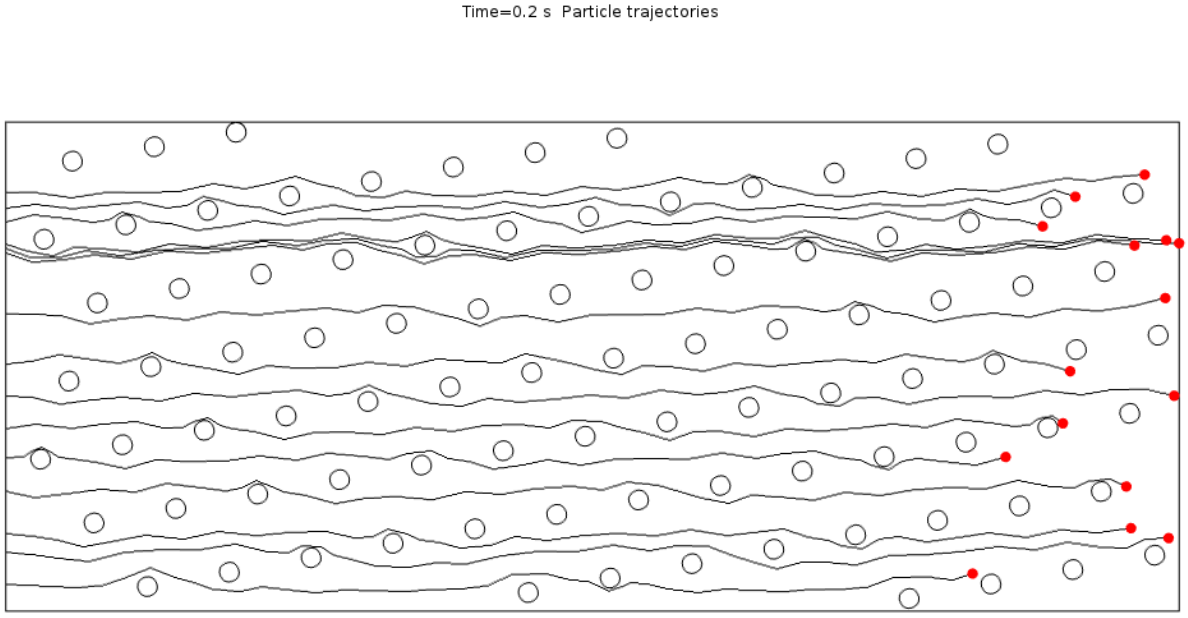
d


Time=0.5 s Surface: Viscous stress tensor, xy component (Pa)
▲ 1.64
1.5
1
0.5
0
-0.5
-1
-1.5
▼ -1.66

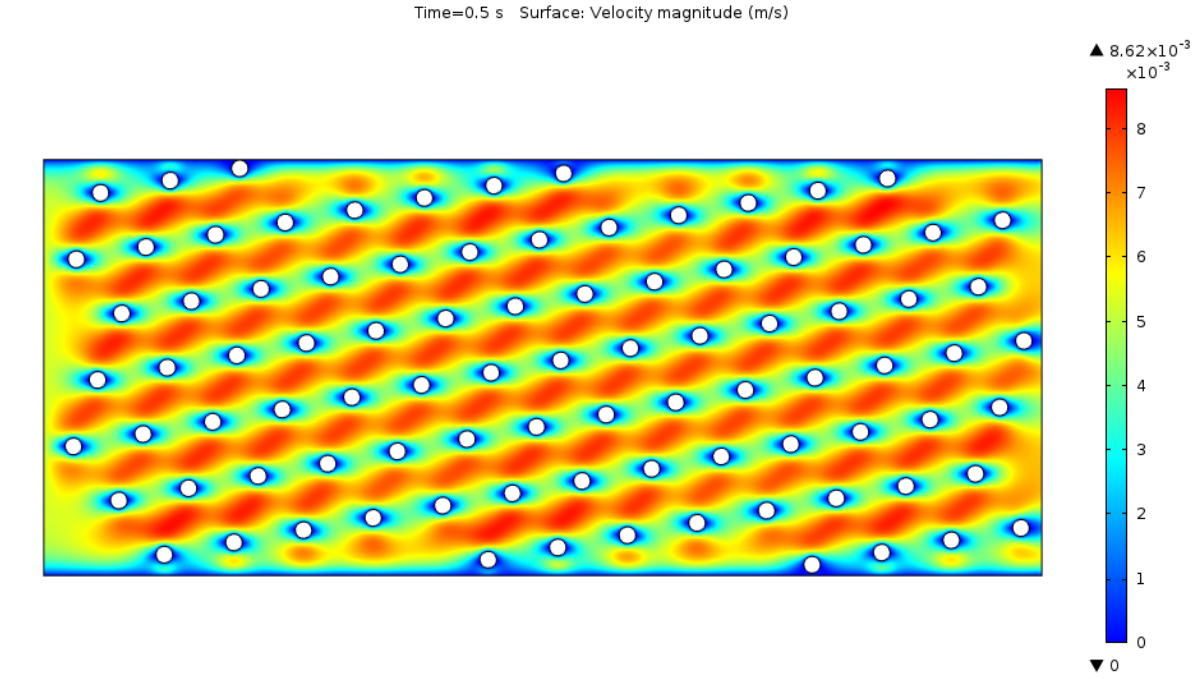
e


Time=0.1 s Particle trajectories

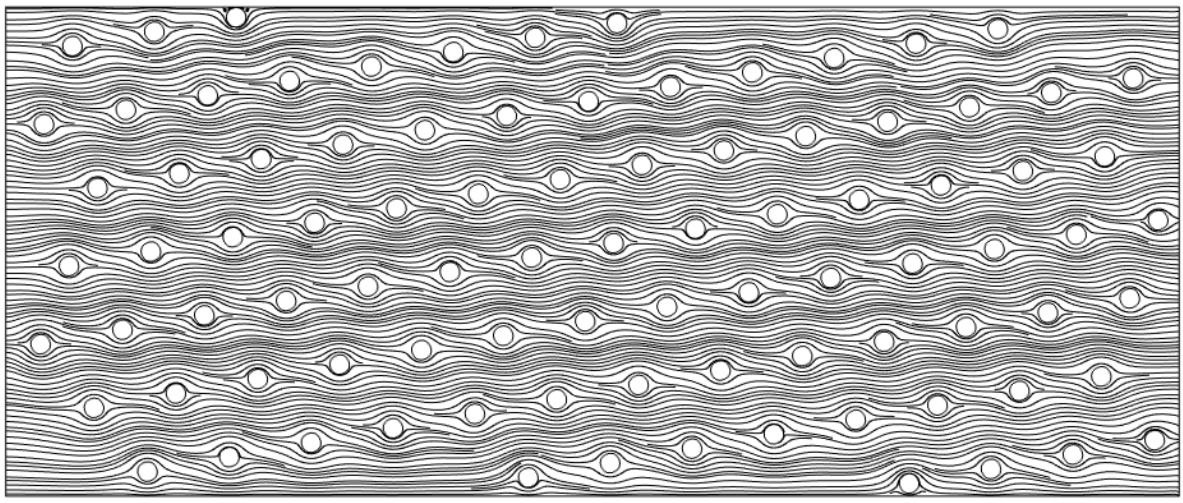
f


Time=0.2 s Particle trajectories

g

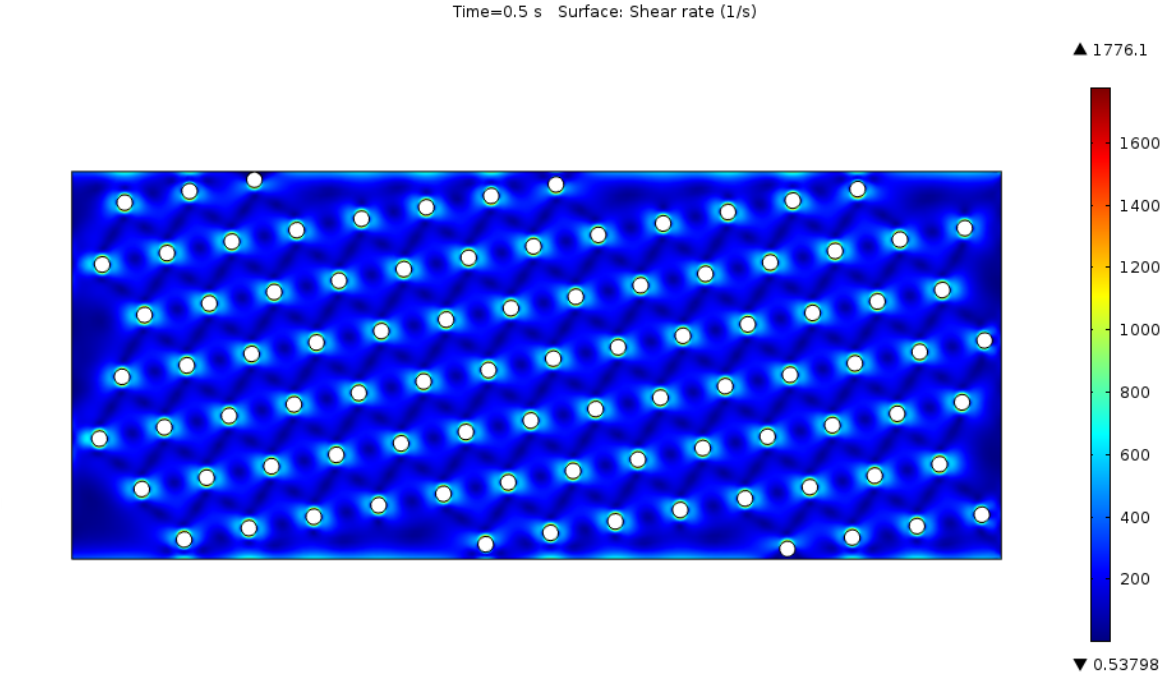

Time=0.5 s Surface: Velocity magnitude (m/s)
▲ 8.62×10^-3
×10^-3
8
7
6
5
4
3
2
1
0
▼ 0

h

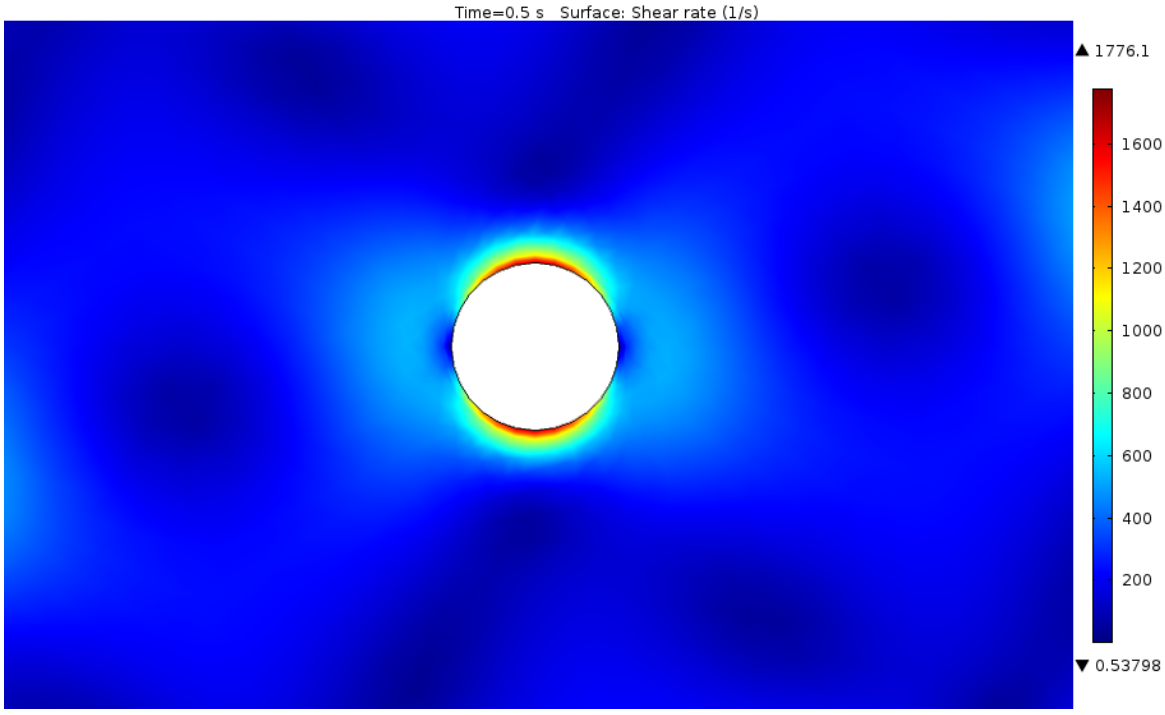

Time=0.5 s Streamline: Velocity field

8. Results Obtained at Velocity 5333.33 µm/s

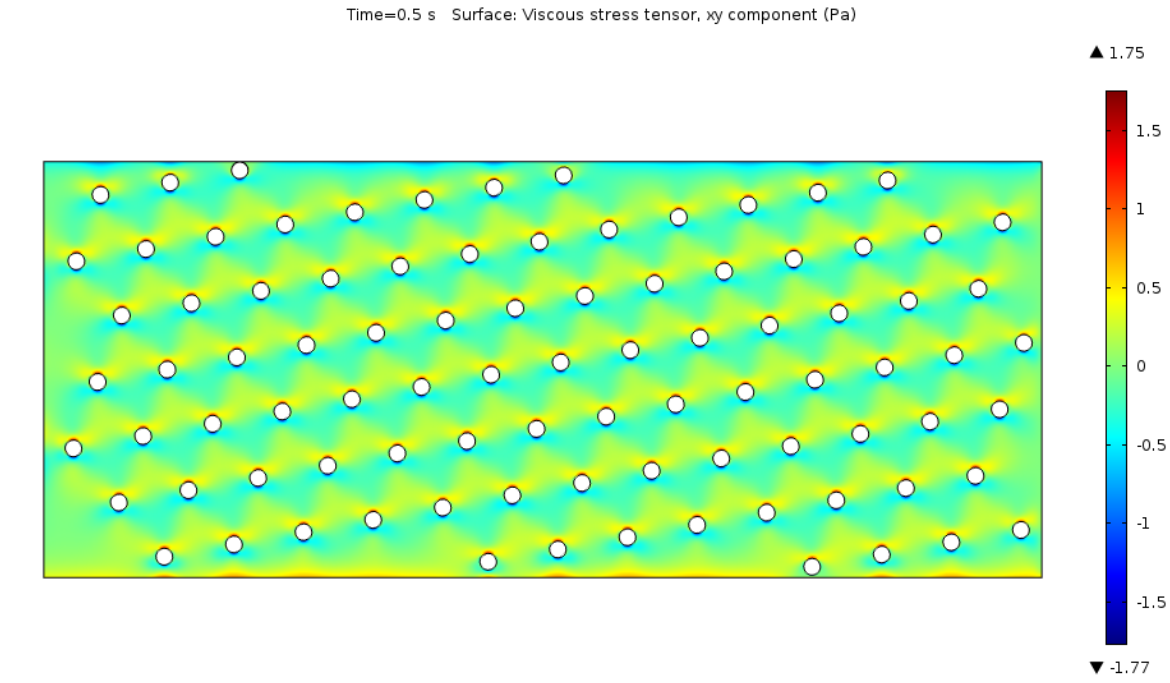
a



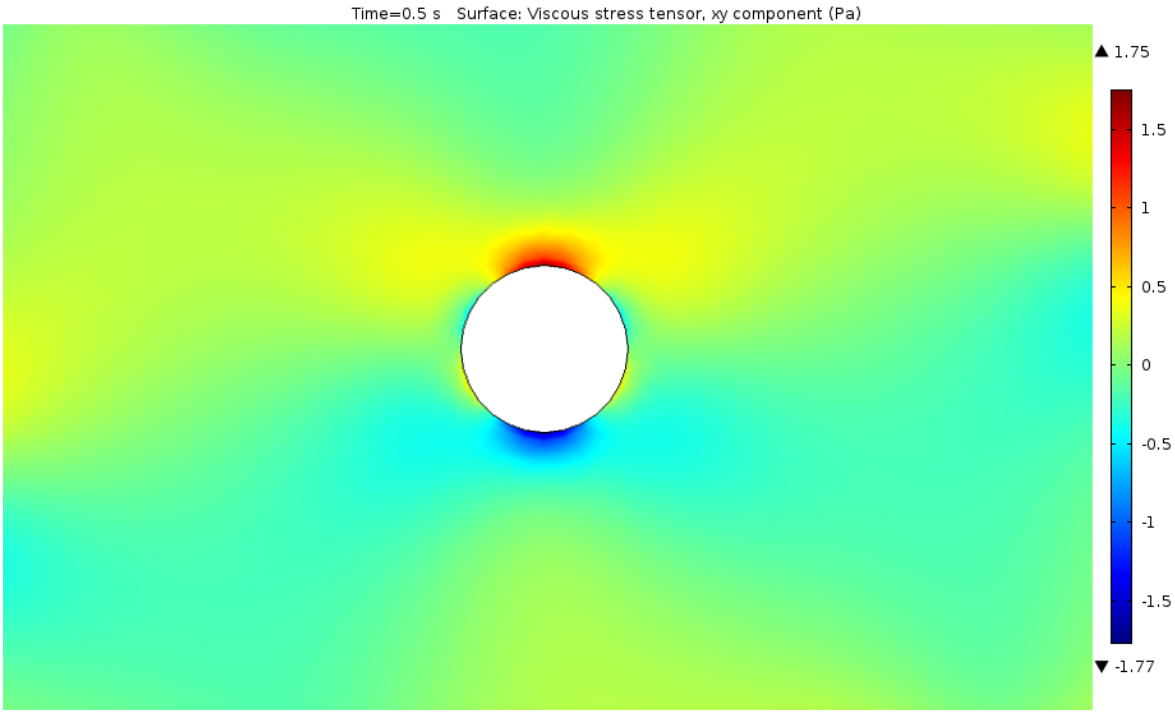
b



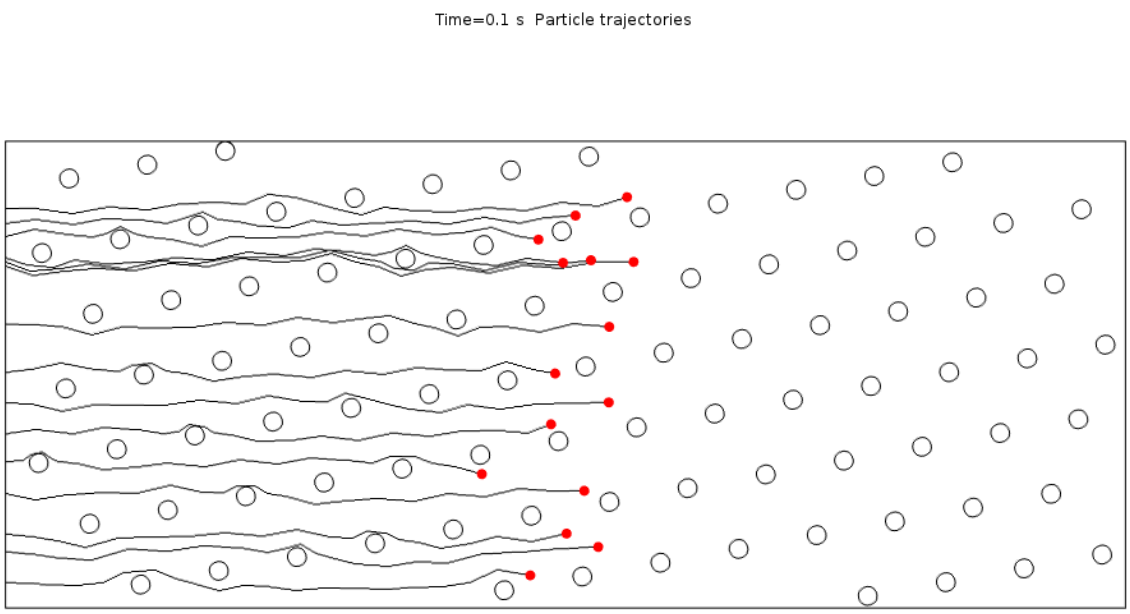
c


Time=0.5 s Surface: Viscous stress tensor, xy component (Pa)
▲ 1.75
1.5
1
0.5
0
-0.5
-1
-1.5
▼ -1.77

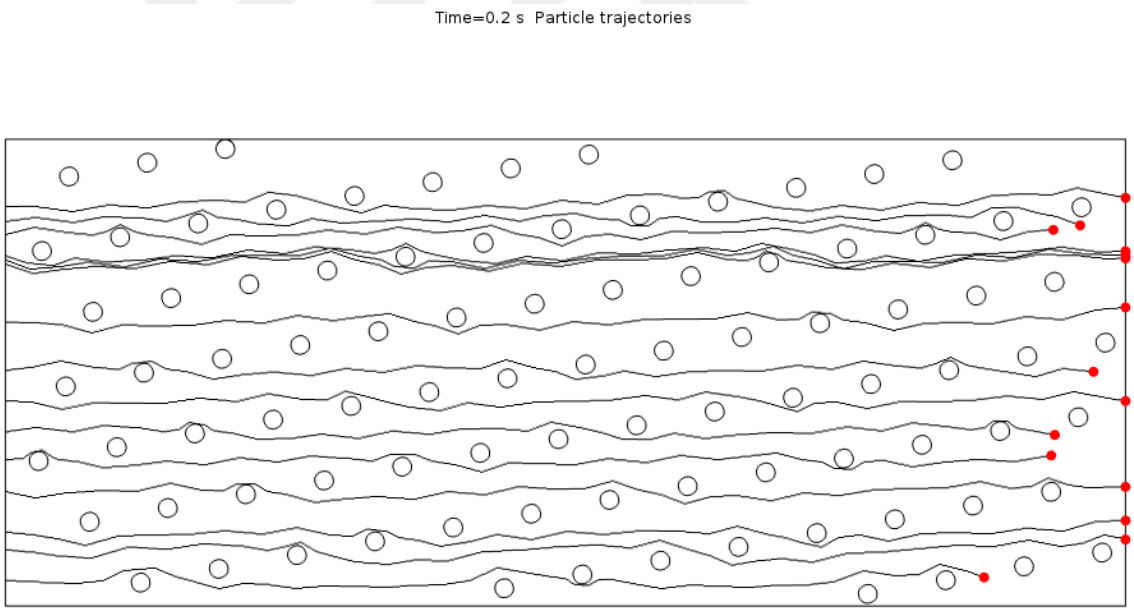
d


Time=0.5 s Surface: Viscous stress tensor, xy component (Pa)
▲ 1.75
1.5
1
0.5
0
-0.5
-1
-1.5
▼ -1.77

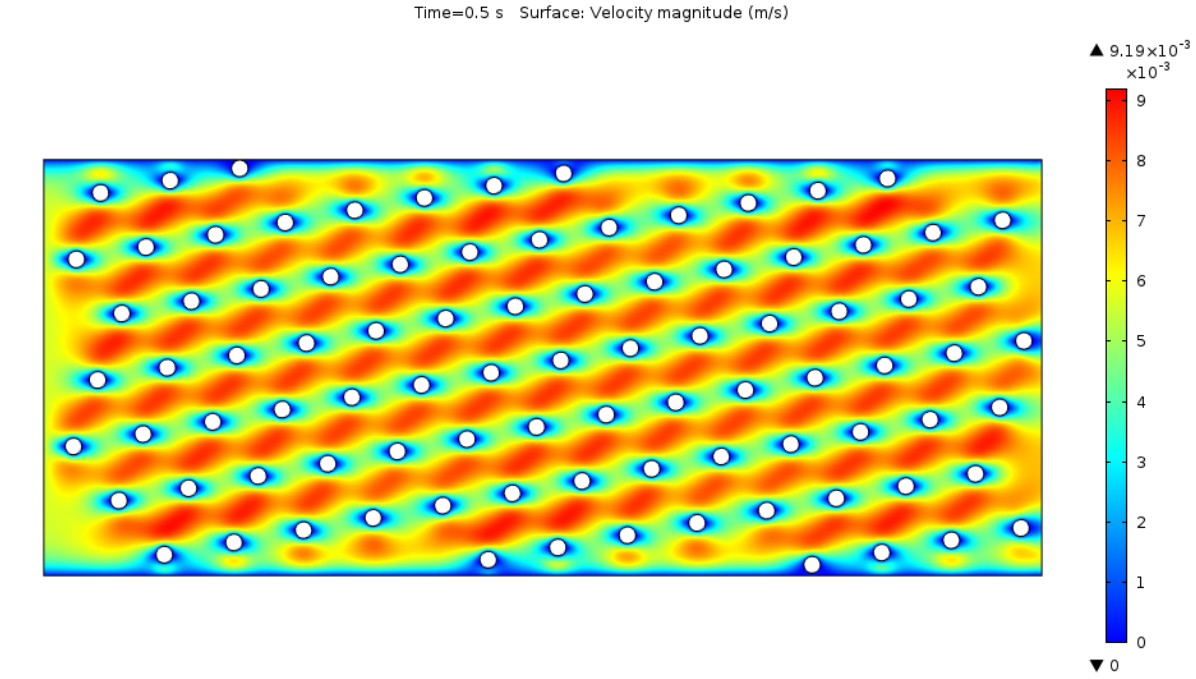
e


Time=0.1 s Particle trajectories

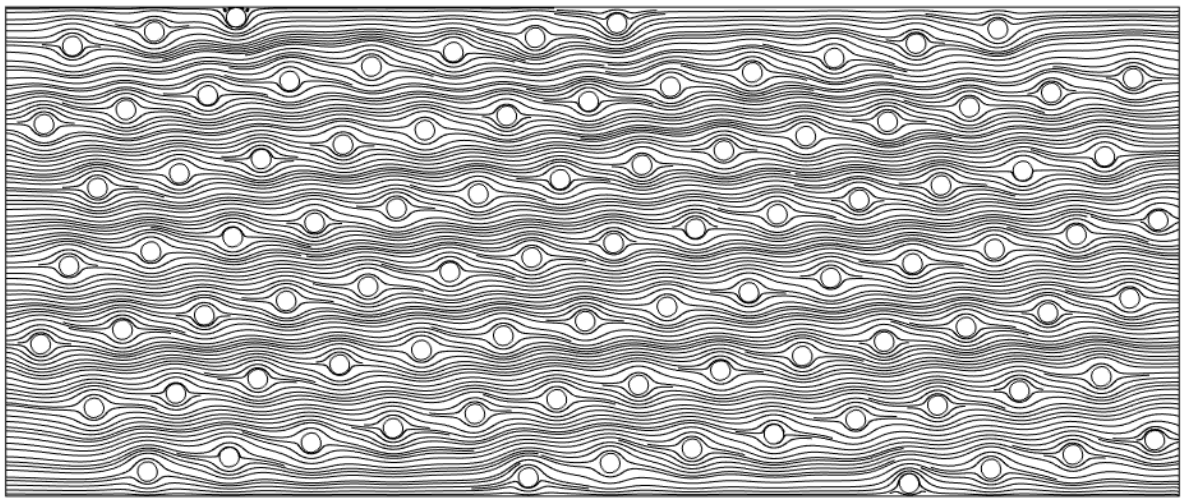
f


Time=0.2 s Particle trajectories

g

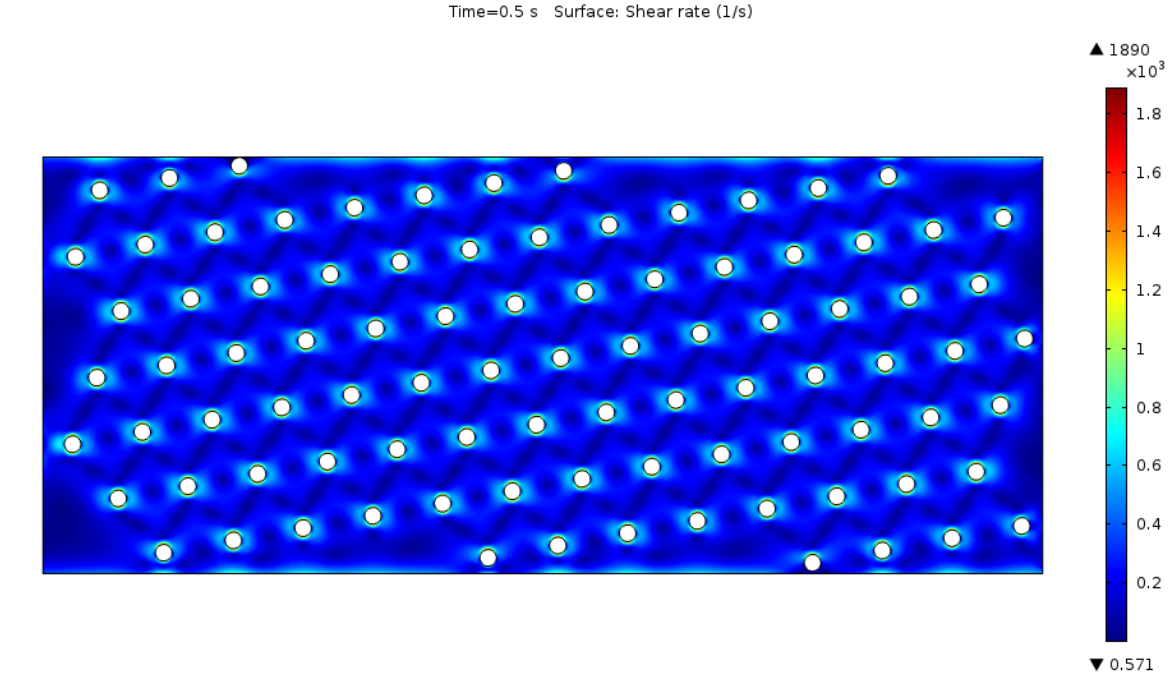

Time=0.5 s Surface: Velocity magnitude (m/s)
▲ 9.19×10^-3
×10^-3
9
8
7
6
5
4
3
2
1
0
▼ 0

h

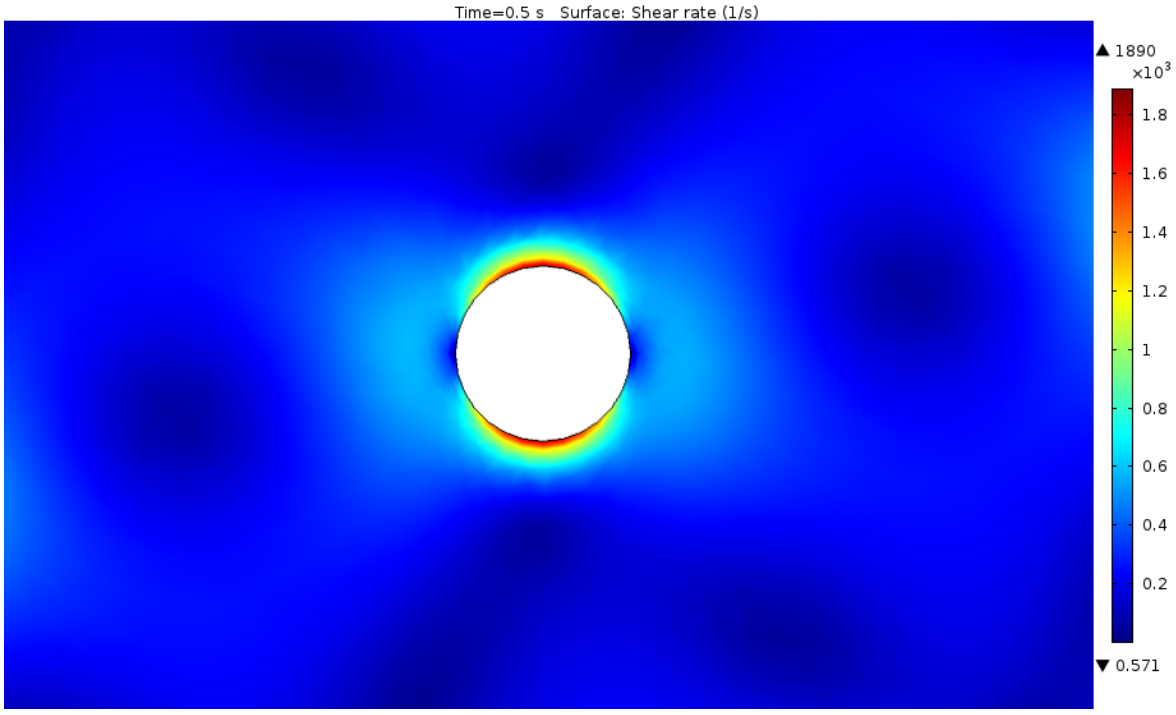

Time=0.5 s Streamline: Velocity field

9. Results Obtained at Velocity 5666.66 µm/s

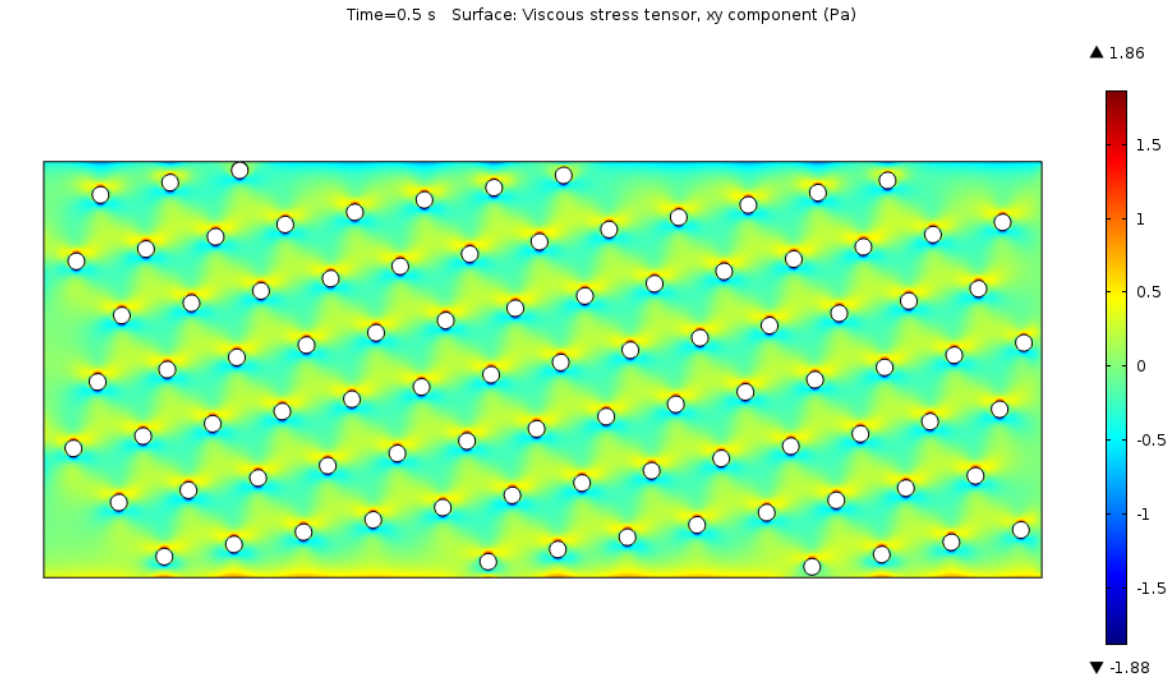
a



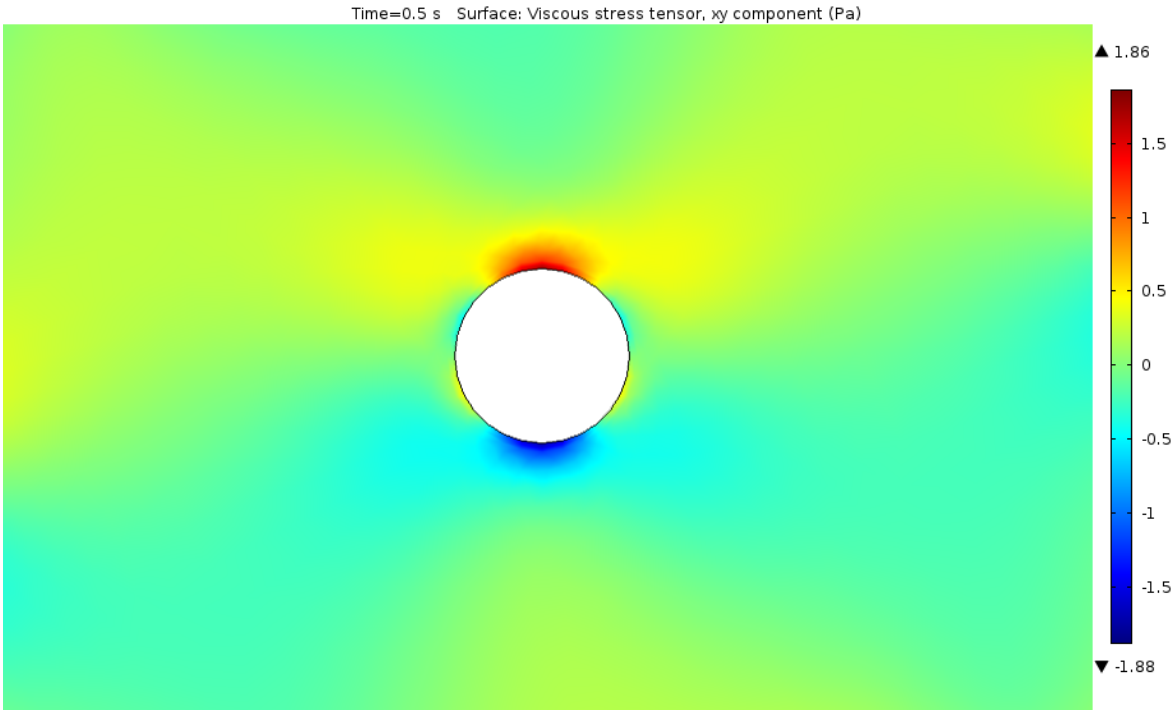
b



c

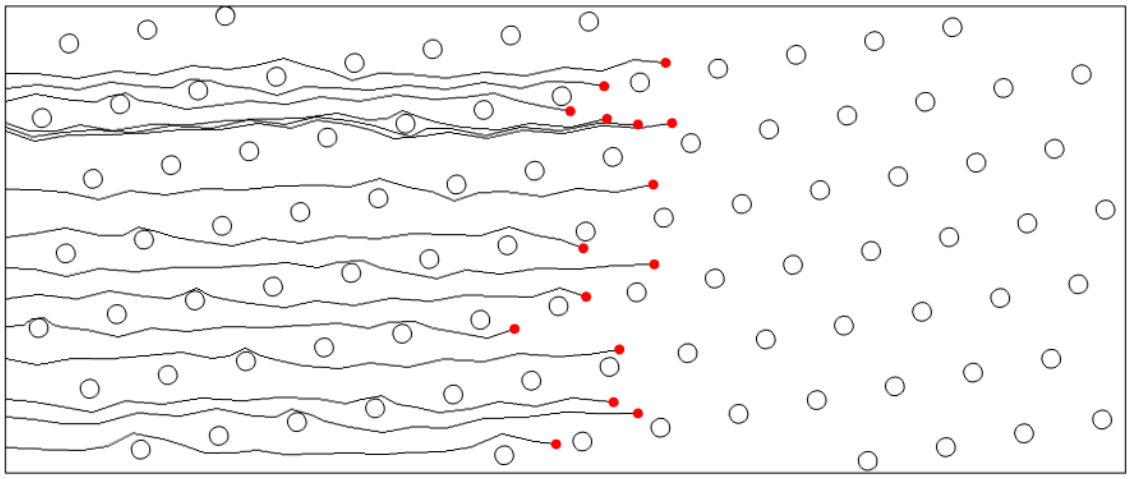

Time=0.5 s Surface: Viscous stress tensor, xy component (Pa)
▲ 1.86
1.5
1
0.5
0
-0.5
-1
-1.5
▼ -1.88

d


Time=0.5 s Surface: Viscous stress tensor, xy component (Pa)
▲ 1.86
1.5
1
0.5
0
-0.5
-1
-1.5
▼ -1.88

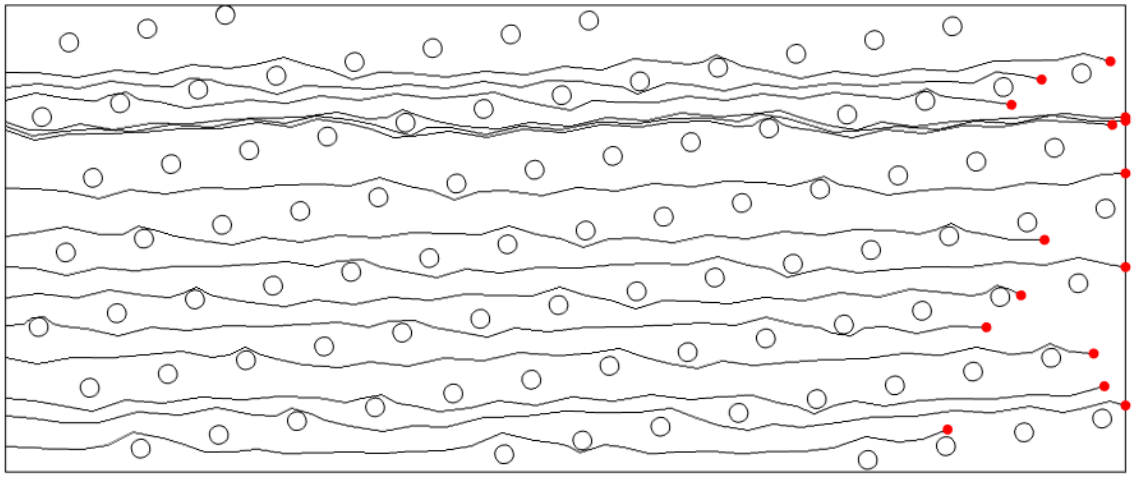
e

Time=0.1 s Particle trajectories

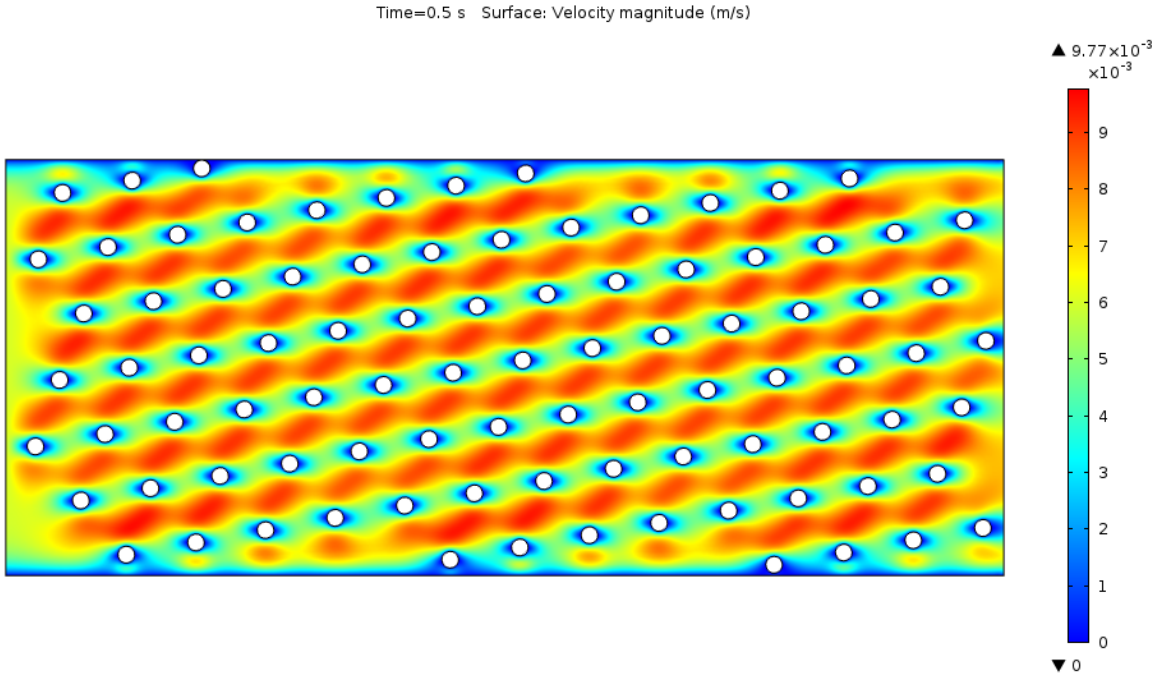


f

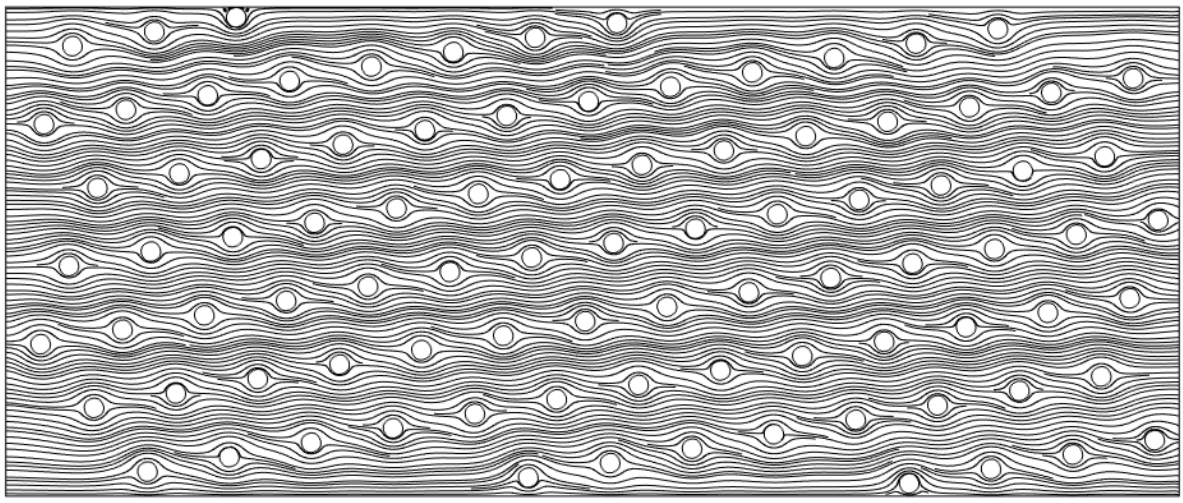
Time=0.18 s Particle trajectories



g

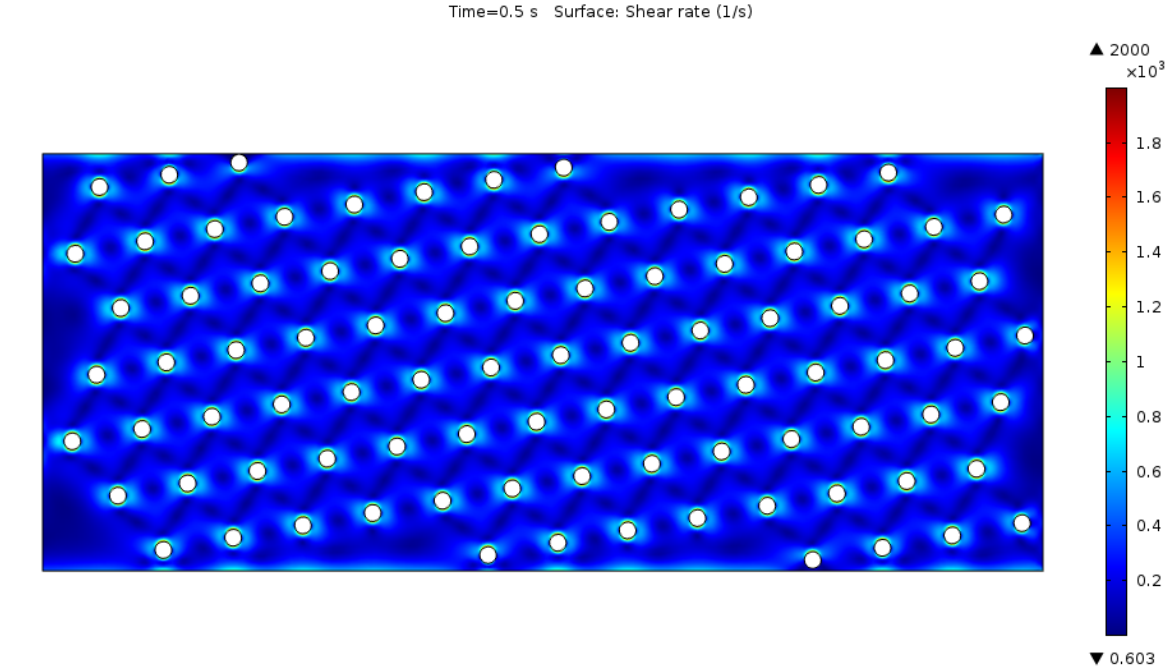

Time=0.5 s Surface: Velocity magnitude (m/s)
▲ 9.77×10^-3
×10^-3
9
8
7
6
5
4
3
2
1
0
▼ 0

h

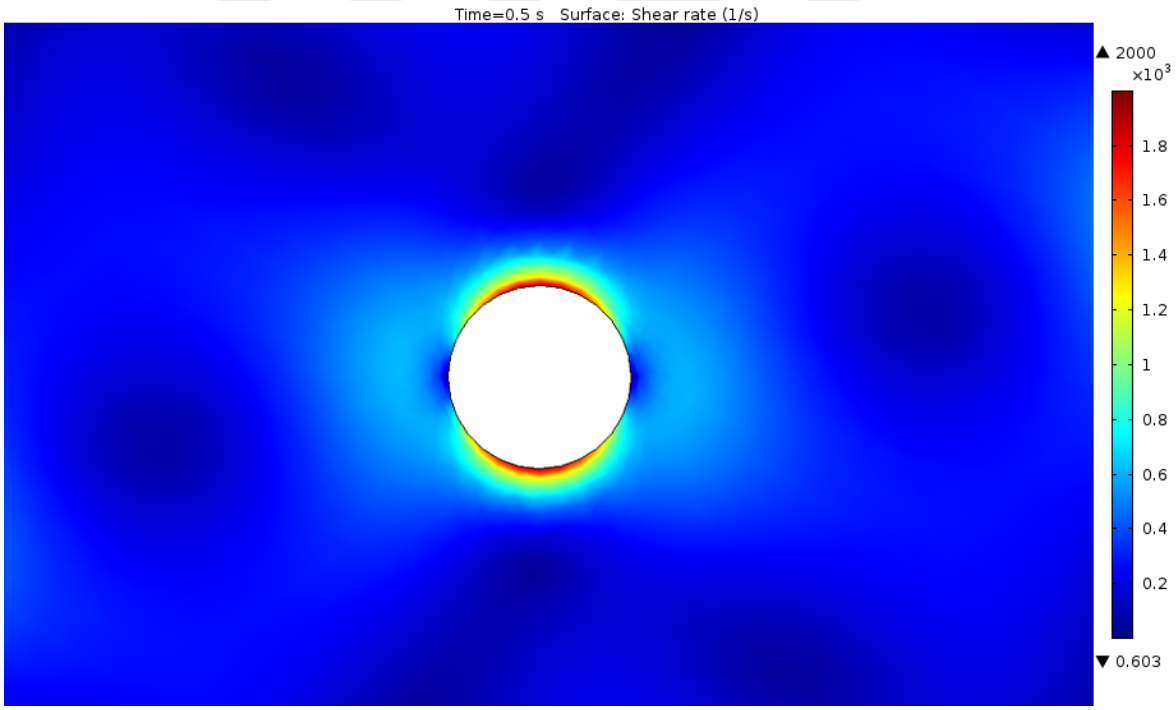

Time=0.5 s Streamline: Velocity field

10. Results Obtained at Velocity 6000 µm/s

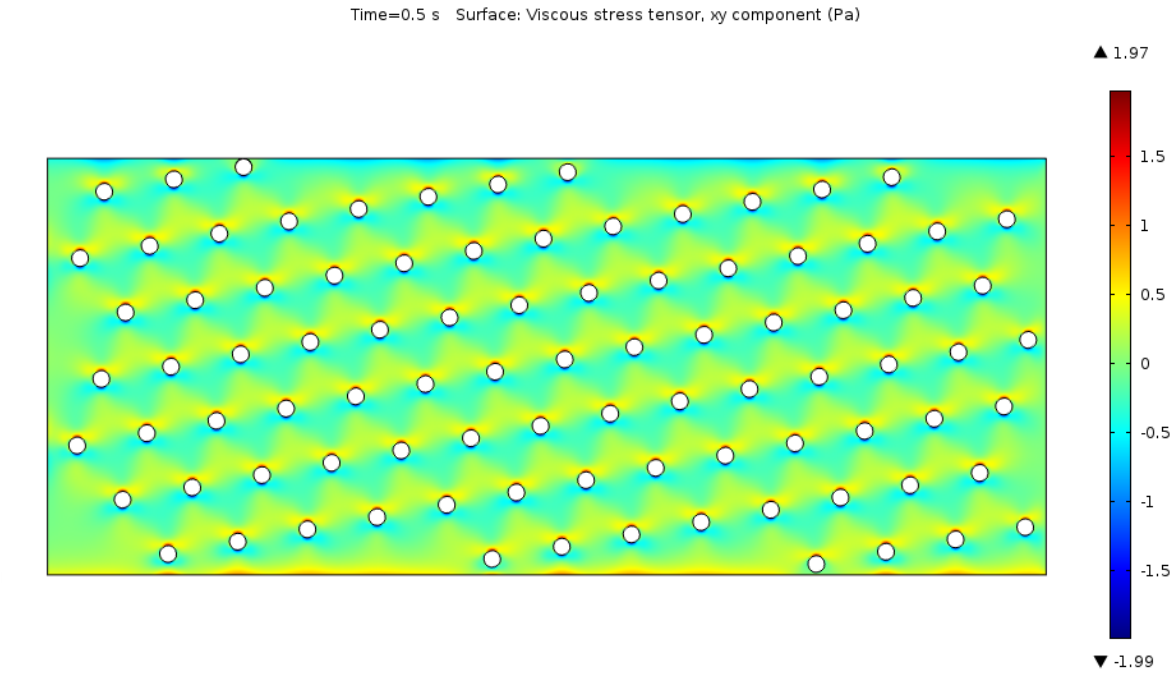
a



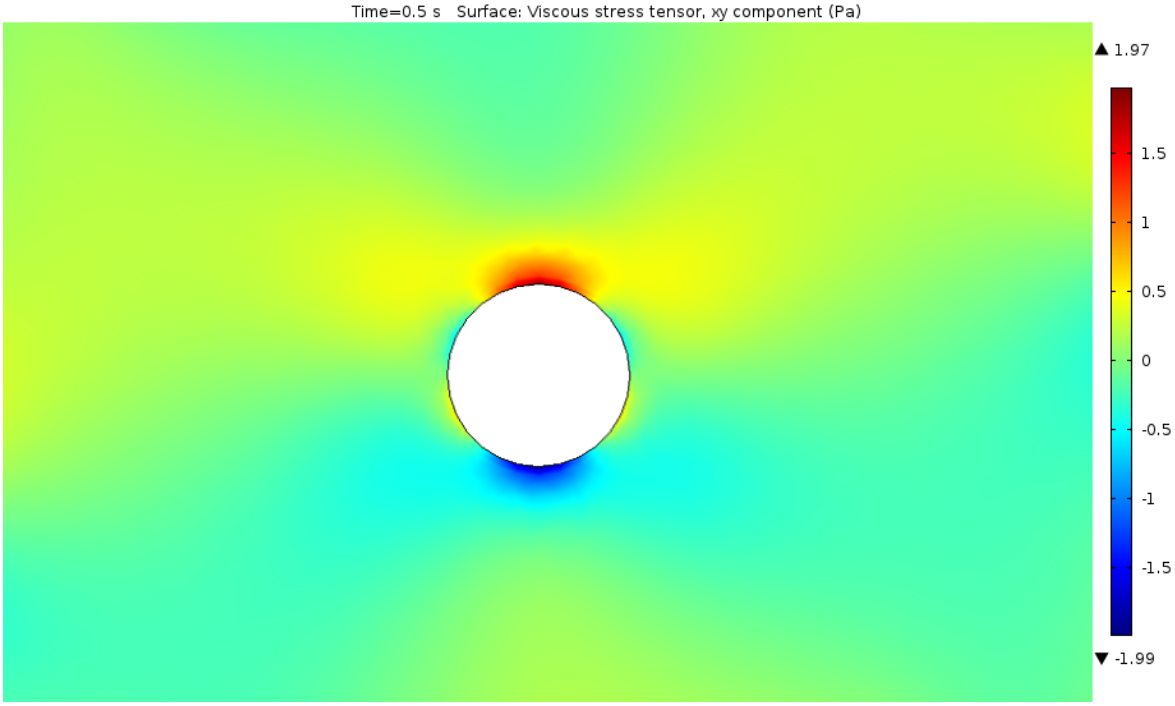
b



c

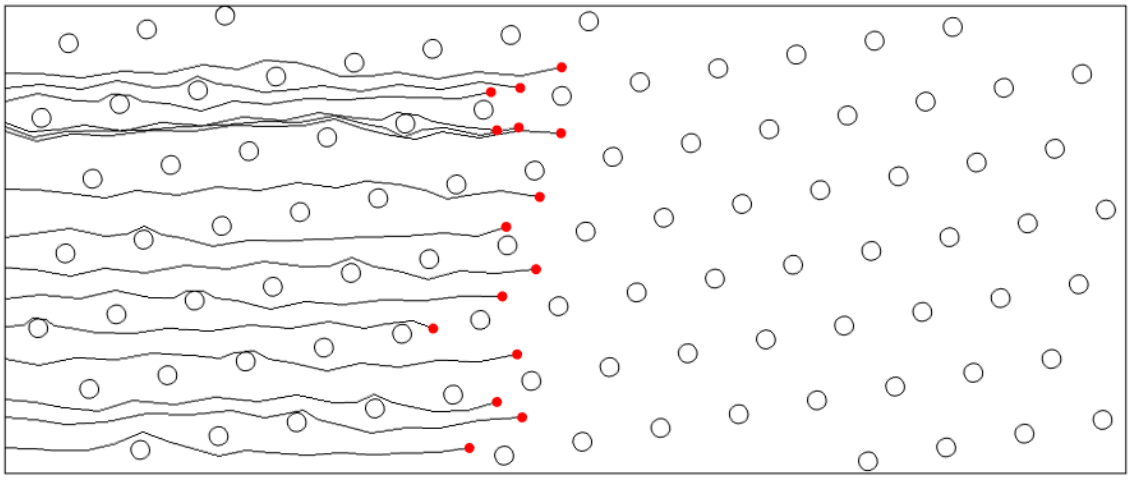

Time=0.5 s Surface: Viscous stress tensor, xy component (Pa)
▲ 1.97
1.5
1
0.5
0
-0.5
-1
-1.5
▼ -1.99

d


Time=0.5 s Surface: Viscous stress tensor, xy component (Pa)
▲ 1.97
1.5
1
0.5
0
-0.5
-1
-1.5
▼ -1.99

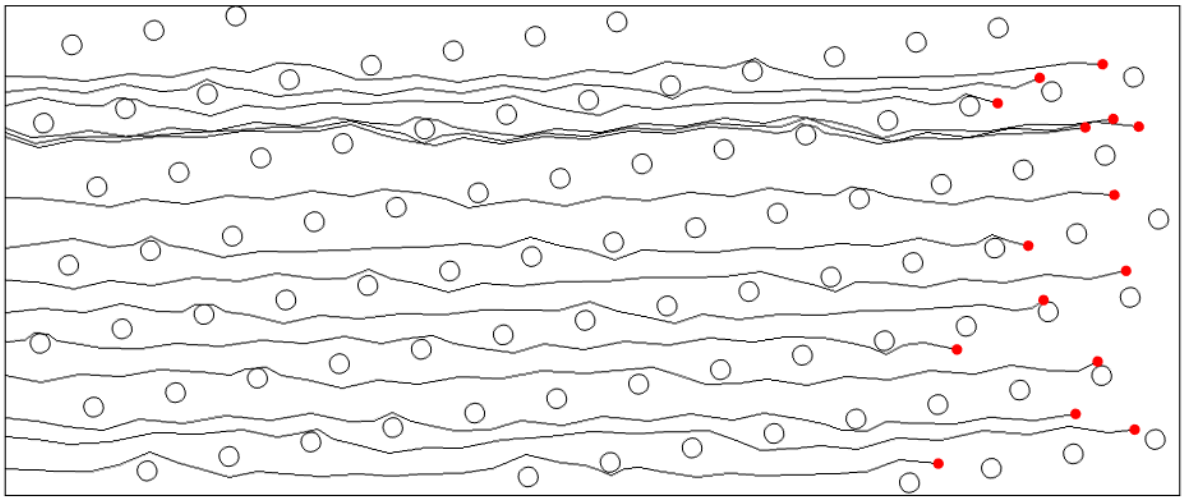
e

Time=0.08 s Particle trajectories

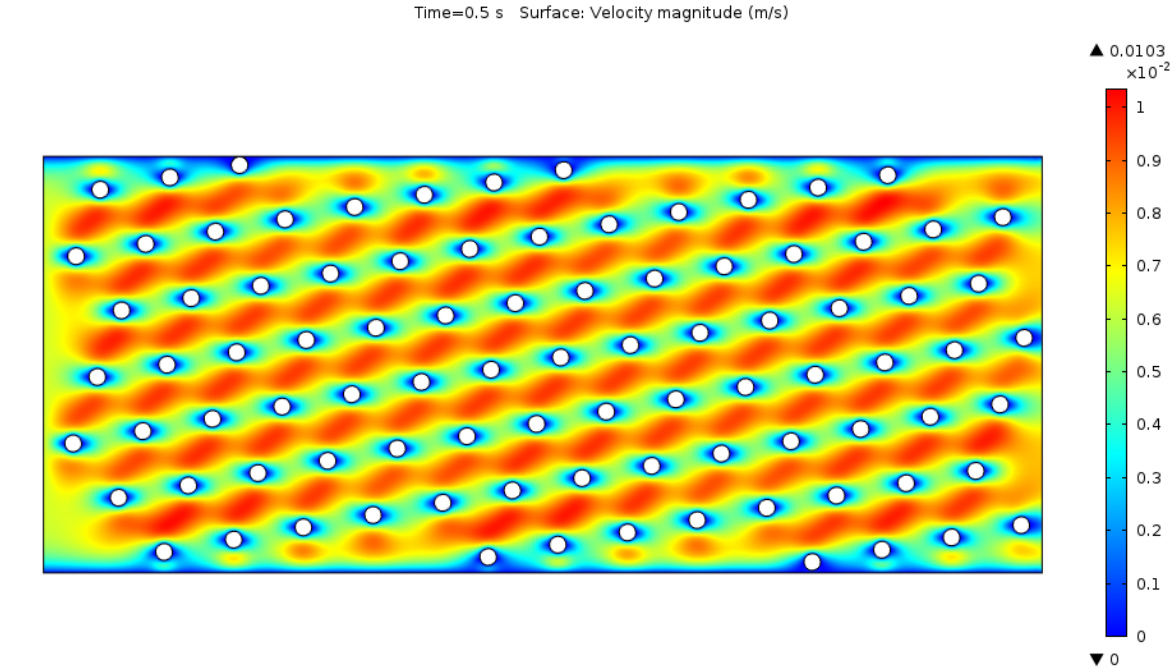


f

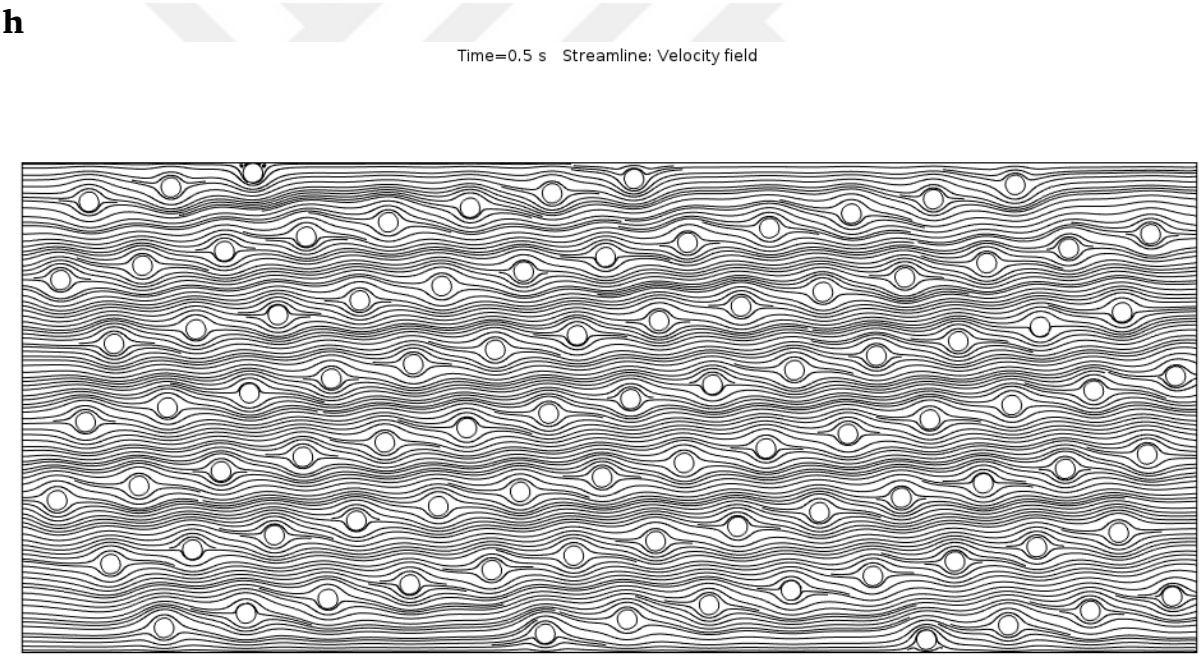
Time=0.16 s Particle trajectories



g


Time=0.5 s Surface: Velocity magnitude (m/s)
▲ 0.0103
×10^-2
1
0.9
0.8
0.7
0.6
0.5
0.4
0.3
0.2
0.1
0
▼ 0

h


Time=0.5 s Streamline: Velocity field

PUBLICATIONS FROM THE THESIS

Papers

1. G. Baydar-Atak, M. A. Insel, M. E. Oruc, H. Sadikoglu, "Optimization of megakaryocyte trapping for platelet formation in microchannels," Chemical Industry and Chemical Engineering Quarterly, In press, doi:10.2298/CICEQ201224012B, 2021.

Conference Papers

1. G. Baydar-Atak, M. E. Oruc, H. Sadikoglu, "Flow dynamics in a microchannel for platelet formation from megakaryocyte," International Conference on Technology, Engineering and Science (IConTES), Antalya, Turkey, 2018.

2. G. Baydar-Atak, M. A. Insel, M. E. Oruc, H. Sadikoglu, "Theoretical investigation of significant parameters affecting the platelet formation in microchips," International Conference of Mathematics Science and Engineering Education (ICESME), Girne, KKTC, 2019.

3. G. Baydar-Atak, M. E. Oruc, H. Sadikoglu, "A general overview: Production of platelets in a microchannel," 5th International Conference on Advances in Mechanical Engineering, İstanbul, Turkey, 2019.

4. G. Baydar-Atak, S. Omeroglu, H. Sadikoglu, M. E. Oruc, "Fabrication of microchip with sub-10 microns for platelet formation from megakaryocyte," 2nd International Eurasian Conference on Science, Engineering and Technology, Gaziantep, Turkey, 2020.

Projects

1. G. Baydar-Atak, (Researcher), M. E. Oruc, (Researcher), B. Yılmaz, (Researcher) H. Sadikoglu (Principal investigator), "Megakaryositlerden trombosit oluşumunun mikroakışkan kanallarda incelenmesi," (2018-2021), YTU BAPK - FCD-2018-3150.